

博士學位論文

Phantom Studies on Breast Cancer Detection  
Using Electrical Impedance Tomography

濟州大學校 大學院



金 奉 奭

2005年 12月

# Phantom Studies on Breast Cancer Detection Using Electrical Impedance Tomography

指導教授 金 慶 淵

金 奉 奭

이 論文을 工學 博士學位 論文으로 提出함

2005年 12月

金奉奭의 工學 博士學位 論文을 認准함



제주대학교 중앙도서관  
JEJU NATIONAL UNIVERSITY LIBRARY

審査委員長 \_\_\_\_\_ 印

委 員 \_\_\_\_\_ 印

委 員 \_\_\_\_\_ 印

委 員 \_\_\_\_\_ 印

委 員 \_\_\_\_\_ 印

濟州大學校 大學院

2005年 12月

# Phantom Studies on Breast Cancer Detection Using Electrical Impedance Tomography

Bong Seok Kim

(Supervised by professor Kyung Youn Kim)

A thesis submitted in partial fulfillment of the requirement for  
the degree of Doctor of Philosophy

2005. 12

Department of Electrical and Electronic Engineering  
GRADUATE SCHOOL  
CHEJU NATIONAL UNIVERSITY

# CONTENTS

Summary (in Korean) . . . . .	iii
I. Introduction . . . . .	1
1.1 Electrical Impedance Tomography . . . . .	1
1.2 Breast Cancer Detection . . . . .	2
1.3 Related Work for Breast Cancer Detection with Electrical Im- pedance Tomography . . . . .	5
1.4 Overview of the Thesis . . . . .	9
II. The Forward Problem Using an Analytical Method in EIT . . . . .	11
2.1 Physical Model in EIT . . . . .	11
2.2 2-D Circular Geometry . . . . .	12
2.2.1 Gap model . . . . .	13
2.2.2 Ave-gap model . . . . .	17
2.2.3 Complete electrode model . . . . .	18
2.2.4 Comparison of the characteristic resistance . . . . .	22
2.3 3-D Mammography Geometry . . . . .	24
2.3.1 Gap model . . . . .	26
2.3.2 Ave-gap model . . . . .	35
2.4 Canonical Patterns . . . . .	36
III. The Inverse Problem in EIT . . . . .	39
3.1 Jacobian Matrix in EIT . . . . .	39
3.1.1 Gap model and ave-gap model . . . . .	41
3.1.2 Complete electrode model . . . . .	42
3.2 Linearization . . . . .	42
3.3 Fast Inversion using a Spectral Representation . . . . .	46
3.4 NOSER Algorithm . . . . .	49
3.4.1 Formulation of the NOSER algorithm . . . . .	49
3.4.2 Determinations of $F(\zeta_0)$ and Hessian matrix $H(\zeta_0)$ . . .	50

3.5	Linearized Kalman Filter . . . . .	52
3.5.1	Formulation of the time-varying model . . . . .	52
3.5.2	Inverse solver based on the linearized Kalman filter . . . . .	54
3.6	Synthesized Voltages and Best Impedivity Approximation . . . . .	56
3.6.1	Finding synthesized complex voltages . . . . .	56
3.6.2	Finding the best constant impedivity approximation . . . . .	58
IV.	Experimental Studies . . . . .	60
4.1	Experimental Setup . . . . .	60
4.2	2-D Circular Geometry . . . . .	61
4.2.1	Static imaging reconstruction . . . . .	62
4.2.1.1	FEM simulation data . . . . .	62
4.2.1.2	Chest phantom experimental data . . . . .	65
4.2.1.3	Comparison between the linearization method and the fast inversion algorithm . . . . .	66
4.2.1.4	Discussion . . . . .	68
4.2.2	Dynamic imaging reconstruction . . . . .	68
4.2.2.1	FEM simulation data . . . . .	69
4.2.2.2	Chest phantom experimental data . . . . .	72
4.2.2.3	Discussion . . . . .	73
4.3	3-D Mammography Geometry . . . . .	74
4.3.1	3-D test phantom and voxel configuration . . . . .	74
4.3.2	Image reconstruction . . . . .	75
4.3.2.1	Distinguishability . . . . .	77
4.3.2.2	Fast inversion algorithm reconstruction . . . . .	79
4.3.2.3	NOSER algorithm reconstruction . . . . .	85
4.3.2.4	Linearized Kalman filter (LKF) reconstruction . . . . .	90
4.3.3	Discussion . . . . .	96
V.	Conclusions . . . . .	97
	Summary . . . . .	100
	References . . . . .	102
	Acknowledgment . . . . .	106

## 초 록

유방암(breast cancer)은 서양 여성들에게서 가장 흔히 발병하는 악성 암(malignant tumor)인데, 초기 검출만이 사망률을 줄일 수 있는 가장 효과적인 방법이다.

유방암 조직은 주변 조직(tissue)과 비교했을 때, 높은 전기적 도전율(conductivity)와 유전율(permittivity)을 보이므로, 본 논문에서는 전기 임피던스 단층촬영법(EIT) 기술을 유방암 검출에 적용하고자 한다.

EIT에서는, 서로 다른 전기적 특성 분포를 갖는 대상물체 표면에 특수하게 제작된 여러 개의 전극들을 균등하게 배치하고, 이를 통하여 전기적 신호(전류)를 주입하여 이에 따른 경계면에 유기되는 전압을 측정한다. 이 전류와 전압 데이터를 바탕으로 EIT 영상복원 알고리즘을 이용하여 물체 내부의 전기적 특성 분포를 추정하고 복원한다.

본 논문에서는, 2-D 원형 구조의 human chest 팬텀과 3-D mammography 구조의 breast 팬텀을 고려하여, 영상복원 알고리즘을 개발하여 적용시켰다. 2-D 원형 구조에서는 FEM 시뮬레이션 데이터와 팬텀 실험 데이터를 사용하여 제안한 알고리즘의 복원 성능을 평가하였다. 3-D mammography 구조에서는 유방암 검출을 위한 임상실험의 전단계인 phantom study로서, 여성의 breast의 외형(shape)과 유사하게 팬텀을 만들고 팬텀 내부에 식염수를 채워 실험하였다.

대부분의 다른 EIT 연구팀들은 FEM(유한요소법), BEM(경계요소법) 등의 수치적 방법(numerical method)을 이용하여 forward solver를 만들어 사용하지만, 본 논문에서는 해석적 방법(analytical method)을 이용하여 forward solver를 만들었다. 본 논문에서는 gap 모델을 학습하고, ave-gap 모델과 CE 모델의 forward solution을 구하는 방법을 제안하였다. 각 수학적 전극모델에 대한 특성 저항(characteristic resistance)을 계산하여 실험 데이터와의 비교결과를 통해, gap 모델과 ave-gap 모델보다 완전전극 모델이 실험 데이터와 거의 유사하게 나타남을 보였다.

3-D mammography geometry에서는 Rensselaer 그룹에서 4×4 electrode array (32-전극)을 갖는 rectangular box 형태의 팬텀에 사용되던 ave-gap 모델 알고리즘을 수정하여 새로운 테스트 팬텀, 즉, 6×6 electrode array (64-전극, 아래쪽 4개의 전극은 사용하지 않음)을 갖는 breast 팬텀에 적용시켰다. 전극의 x-y 평면에 대한 공간 해상도(spatial resolution)를 학습하기 위해, 5 mm solder 표적과 10 mm copper 표적을 전극 바로 밑에서 5 mm 떨어진 곳에 위치시키고 다른 한 개의 10 mm copper 표적은 4개의 전극이 서로 인접해 있는 gap에서 5 mm 떨어진 곳에 위치시켜 테스트 하였다. 그리고 10 mm copper 표적을 전극 바로 밑에서 7.5 mm, 10 mm, 12.5 mm, 15 mm 떨어진 곳에 위치시키면서 z-축(depth)에 따른 공간 해상도를 학습하였다. 그리고 difference 복원영상들을 통해서 각각 해당 표적의 위치 정보를 잘 추정하고 있고 있음을 확인하였다.

ACT4 시스템은 complex 전압을 주입하고 complex 전류를 측정하기 때문에, 주입전류와 측정전압으로 이루어지는 기존 EIT 문제와 등가적으로 해결하면서 ACT4의 complex 데이터를 영상복원 알고리즘에 적용시키기 위해 synthesized voltage 구하는 방법을 제안하였다.

기존에 사용되던 linearization 방법과 NOSER 알고리즘은 real 알고리즘이며, 본 논문에서는 이들을 complex data를 위한 complex 알고리즘으로 제안하였다. 그리고 spectral representation을 이용한 fast inversion 알고리즘과 선형 칼만 필터도 complex 알고리즘으로 전개하여, phantom study에서의 영상복원에 적용하였다. 그리고 linearization 방법과 fast inversion 알고리즘의 복원 영상의 성능비교 측면에서 두 알고리즘은 거의 같은 결과를 산출하지만, 대상물체 내부의 admittivity 분포를 추정하는 복원 시간 측면에서는 fast inversion 알고리즘이 linearization 방법보다 추정 시간이 단축됨을 보였다.

# I. Introduction

## 1.1 Electrical Impedance Tomography

Electrical impedance tomography (EIT) is an imaging modality that estimates and reconstructs the electrical properties in a body. In many cases the electrical properties (conductivity and permittivity, resistivity and capacitive reactivity) carry valuable information on the structural, and especially, functional properties of the targets. In EIT, small electrical currents are injected through electrodes placed on the surface of the body and the corresponding voltages are measured through these electrodes. These voltage and current data are used in reconstruction algorithms that reconstruct and display the internal electrical properties. The physical relationship between the internal admittivity (impedivity) distribution and the boundary voltages is governed by a partial differential equation with appropriate boundary conditions.

Although the spatial resolution of EIT is not comparable to other imaging techniques such as magnetic resonance imaging (MRI), computerized tomography (CT) or ultrasonic imaging, EIT has nonetheless some advantages such as being harmless and low cost, and having better temporal resolution, which make it possible to track relatively fast impedance changes in the body (Vauhkonen *et al.* 1998, Webster 1990). Therefore, if we combine the EIT technique with other modalities, such as X-ray mammography or ultrasonic imaging, it might provide new opportunities for improving breast cancer detection.

EIT is divided into two problems, the forward problem and the inverse problem. The forward problem in electrical impedance imaging is to compute the voltages on the boundary of the body given the internal admittivity (impe-



divivity) distribution and applied currents in a partial differential equation. The inverse problem is to determine the admittivity (impedivity) distribution given the injected current patterns and their corresponding voltage measurements.

The EIT reconstruction methods can be classified into two categories, stationary imaging and non-stationary imaging. In stationary imaging, the internal admittivity distribution of the body is time-invariant within the time required to acquire a full set of voltage measurement data. Stationary imaging can further be divided in two categories, static imaging and difference imaging. In static imaging, the reconstruction is based on a single data set of voltage measurements, and the absolute values of the conductivity and permittivity distributions are determined. In difference imaging, two data sets are measured, that is, one data set comes from a reference and the other data set comes from a second measurement. Based on the difference between these measurements the difference of the admittivity distributions can be estimated. In non-stationary or time-varying or dynamic imaging, the time-dependence of the impedivity distribution is taken into account, and it provides an estimate for the impedivity distribution after each current pattern is applied to the body (Kim *et al.* 2001, Vauhkonen 1997, Vauhkonen 2004).



## 1.2 Breast Cancer Detection

Breast cancer is the most commonly diagnosed malignant tumor among women in the western world (American Cancer Society 2005a, Boring 1994). Early detection of breast cancer is the most effective method for reducing breast cancer mortality rate. X-ray mammography is the standard technique presently used for breast cancer screening in clinical practice (American Cancer Society 2005a). However, it has significant diagnostic flaws. Breast screening is an uncomfortable and painful procedure for patients. It involves compression of breast to keep them still while the mammogram is taken. And its

screening procedure causes risk for patients being exposed to ionizing radiation. While mammography is sensitive for detecting breast abnormalities, it sometimes cannot differentiate between benign and malignant lesions and is less accurate in patients with dense glandular breasts (Edell and Eisen 1999), which means that breast screening has rather low specificity. For these reasons, to improve the diagnostic accuracy of breast imaging in distinguishing benign breast conditions from breast cancers, other imaging approaches have been studied. The following imaging modalities are cited from the American Cancer Society (2005b).

**Ultrasound (sonography):** This is an imaging method in which high-frequency sound waves are used to look inside a part of the body. Ultrasound has become a valuable tool to use along with mammograms because it is widely available, non-invasive, and less expensive than other options. However, the effectiveness of an ultrasound test depends on the operators level of skill and experience. Although ultrasound is less sensitive than MRI (that is, it detects fewer tumors), it has the advantage of being more available and less expensive.

**Magnetic resonance imaging (MRI):** MRI uses magnets and radio waves to produce very detailed, cross-sectional images of the body. MRI is most often used along with mammograms or breast ultrasound to detect breast cancer, particularly in women with very dense breasts. A few recent studies have shown that for younger women at very high risk of breast cancer, MRI screening finds more cancers than standard mammography alone. The MRI studies found many more abnormalities that were not cancers, which led to an increased number of unnecessary biopsy procedures. MRI is also more costly and time-consuming.

**Technetium sestamibi scan (scintimammography):** In this procedure, a small amount of a radioactive substance is injected into an arm vein. A special camera then records where radiation has accumulated in the

breasts. The general consensus is that this test is less sensitive than mammography, especially when the tumor is still small and most likely to be curable.

**Positron emission tomography (PET):** PET is another type of nuclear medicine study. Like the sestamibi test, a tiny amount of radioactive substance is injected into an arm vein. Unlike most other imaging tests that are based on changes tumors cause in the body's structure, PET scanning depends on changes in tissue metabolism. PET is being used to detect metastatic disease (cancer spread) and has been successful in that role. The PET scan is not currently used for primary breast cancer detection because it does not reliably detect tumors smaller than 1 cm, but research is being done to improve the accuracy of this test.

**Thermography (Thermal imaging):** Thermography is a way of measuring and mapping the heat on the surface of the breast with the use of a special heat-sensing camera. It is based on the idea that the temperature rises in areas with increased blood flow and metabolism, which could signify a tumor. Thermography has been around for several decades, and some scientists are still attempting to improve the technology for use in breast imaging. However, no study has ever shown that it is an effective screening tool for early detection of breast cancer.

**Digital mammograms:** This is similar to standard mammography in that x-rays are used to produce an image of the breast. The differences being the way the image is captured electronically, recorded, viewed on a computer monitor, and stored. Digital images can be transmitted over phone lines to another location for remote consultation with breast specialists. A digital mammogram is commonly used in stereotactic imaging to guide breast biopsy because it is rapid and reliable. Digital mammograms are not yet widely available in hospitals around the country.

**Computed tomography laser mammography (CTLM):** This is an experimental imaging test using laser technology to examine different planes of breast tissue and produce a 3D view of the breast. The technique does not use radiation and does not require breast compression. This test is only available in clinical studies and has not yet been approved for general use.

**Optical imaging:** This involves either passing light through the breast or reflecting light off of it and then somehow measuring the light that returns. The technique does not use radiation and does not require breast compression. Optical imaging might be useful at some point for detecting tumors or the blood vessels supplying them.

For more information, see the following references: American Cancer Society 2005b, Edell and Eisen 1999, Singhal and Thomson 2004.

### 1.3 Related Work for Breast Cancer Detection with Electrical Impedance Tomography

Various researches have been conducted on freshly-excised malignant breast tissues compared to surrounding normal tissues in an *in vitro* impedance cell. From these results and comparison with adjacent normal tissues, it was found that breast tumors have typically higher conductivity and permittivity (Fricke and Morse 1926, Jossinet 1998, Surowiec *et al.* 1988). This means that there are significant differences in electric properties between normal breast tissues and breast tumors. Therefore, electrical impedance of tissue could be used as an indicator for breast cancer detection (Zou and Guo 2003). Electrical impedance-based techniques as new imaging modalities for breast cancer detection have been developed.

EIT is one of these noninvasive impedance imaging techniques. EIT has been widely investigated by over 20 research groups for its clinical appli-

cations, for example, gastric function, pulmonary ventilation, perfusion, and hyperthermia (Boone *et al.* 1997). Breast cancer detection has also been studied by few research groups. A review of EIT techniques for breast cancer detection is presented in Zou and Guo (2003).

**Israeli group (T-Scan):** T-Scan 2000 (TranScan Medical Inc.) was a commercially available impedance imaging device for breast cancer detection. T-Scan was approved by the U.S. Food and Drug Administration (FDA) in 1999 to be used as an adjunct tool to mammography in helping detect breast cancer (FDA 1999).

T-Scan generates a low-level electric signal that is transmitted into the body. The resulting electric field is then measured by sensors in a non-invasive probe placed on the breast. The scanning probe uses 256 sensors in high-resolution mode and 64 sensors in normal-resolution mode. Measurements are made over several frequencies using proprietary algorithms to create and display a real-time electrical image of the breast along with immediate results. The resulting impedance images of the breast tissue can be used to help determine if the region of interest is a normal tissue or a cancerous tumor (Imaginis 2000, Mirabel Medical 2002).

**Moscow group (Centillion):** The Centillion system has been developed by the Moscow group and commercialized by TCI (Technology Commercialization International Inc.). Small currents (0.5mA, 50kHz) are applied into the breast tissue through a handheld device (compact array of 256 electrodes) and the resulting voltage measurements are taken within 20 seconds. These data are reconstructed by a modified back projection method into direct-to-digital tomographic conductivity images of the breast. Seven tomographic image slices are created within 40 seconds at depths of 0.4 cm to 4.6 cm to detect and isolate tumors (TCI 2003).

Cherepenin *et al.* (2001) reported the results of its preliminary clinical trial on 21 women. Eighty-six percent of examinations were found to

fully or partially agree with diagnoses made by X-ray mammography and biopsy.

**Toronto group (Z-Tech):** The Z-Tech breast cancer detection system has been built by the Toronto group. To begin the breast cancer screening test a participant lies on her back on an examining table. Over 300 combinations of electrodes, one combination at a time, are selected for impedance measurements throughout each breast. The entire procedure requires only 3 minutes to complete.

The HEDA (homologous electrical difference analysis) method uses side-by-side comparison of the impedance of many mirror image (homologous) breast regions. HEDA results are calculated and reported immediately as straightforward numerical values. There is no intrinsic delay in reading an image (Z-Tech 2004).

**Dartmouth group (EIS):** The Dartmouth group built and tested a 32-electrode, multi-frequency 2D EIS (electrical impedance spectroscopy) system. This system produces absolute electrical conductivity and permittivity values using a dual mesh scheme and Newton's method (Dartmouth College 2001).

Osterman *et al.* (2000) have modified and deployed a 3-D EITS (spectroscopic electrical impedance tomography) system to investigate the feasibility of delivering EITS breast examinations on a routine basis. Imaging examinations have consisted of the acquisition of multi-channel (10 kHz to 1 MHz) measurements at ten frequencies on both breasts. Participants lie prone on an examination table with the breast to be imaged pendant in the electrode array that is located below the table. Thirteen participants were tested. The examination took about 10 minutes per breast including electrode-positioning time. Structural features in the results of the EITS images correlated with limited clinical information available on participants. However, localized near-surface

electrode artifacts were evident in the reconstructed images.

**Rensselaer group (ACT3 and ACT4):** The Rensselaer group has also studied breast cancer detection using the ACT3 (adaptive current tomography) system which is a real-time impedance imaging instrument (Cook *et al.* 1994, Edic *et al.* 1995).

Mueller *et al.* (1999) studied the use of a single  $4 \times 4$  rectangular electrode array to collect the voltage measurements and reconstruct 3-D conductivity images using a linearization algorithm. Phantom studies were conducted using a rectangular tank filled with a saline solution. Electrode-sized agar targets ( $5 \times 7 \times 5.5$  mm) were suspended in a phantom at several positions. The conductivity ( $300$  mS/m) of the saline solution was chosen to approximate that of healthy breast tissue, and the conductivity ( $900$  mS/m) of the agar was chosen to approximate that of a breast tumor. They applied normalized eigenfunction current patterns on 16 electrodes that maximize the voltage signal (Gisser *et al.* 1990, Isaacson 1986). Their experimental results showed that even though the inhomogeneity's position was well characterized in the plane of the electrode, the depth resolution was still poor in the reconstruction. Choi *et al.* (2004) presented a simplified model of the mammography geometry which was modeled as a rectangular box with  $4 \times 4$  electrode arrays on the top and bottom planes. A forward model was derived for the homogeneous conductivity distribution and validated by experiment using a phantom tank. Their results showed that the predicted voltages were in a good agreement with the measured voltages.

Kao *et al.* (2005) reproduced Mueller *et al.*'s study and designed a new test phantom with a single  $5 \times 5$  planar electrode array. They used the combination of the Tikhonov and NOSER-type regularizations in the reconstruction algorithm. Their experimental results showed that the combination of two regularizations allows static images of a 2 cm

cube target placed 2 *cm* distant from the electrode array and difference images of a 1 *cm* cube target placed 4 *cm* away from the array.

The improved instrument ACT4 is presently in its final stage of construction. The ACT4 system can support up to 64 electrodes with an excitation frequency that is selectable from a discrete set in the range from 300 Hz to 1 MHz for breast cancer detection (Ross 2003, Liu *et al.* 2005). The Rensselaer group is preparing an initial clinical trial for breast cancer detection at Massachusetts General Hospital (MGH) in late 2005.

#### 1.4 Overview of the Thesis

In this thesis, the 2-D circular and 3-D mammography geometries are considered, and reconstruction algorithms are applied to both geometries. In the 2-D circular geometry, we evaluate the reconstruction performances of the proposed algorithms using FEM simulation data and experimental data. In the 3-D mammography geometry, we consider phantom studies for the breast cancer detection. This work was accomplished with the experimental data of ACT3 and ACT4 systems and was carried out with the help of the Rensselaer group (Impedance Imaging Lab). The aims of the thesis are:

- to find the analytical forward solution of the mathematical model, especially, the complete electrode model using Fourier series form.
- to introduce the fast inversion using a spectral representation in the 2-D and 3-D reconstructions.
- to find the synthesized complex voltages that are combined with the complex data (applied complex voltages and measured complex currents) obtained from the ACT4 system.



- to present a dynamic impedance imaging technique with the aid of the linearized Kalman filter for the real-time reconstruction of the human chest.
- to apply reconstruction algorithms presented in this thesis to phantom studies of the mammography geometry for breast cancer detection.

The main goal of the present work is to apply a 3-D reconstruction algorithm with the planar electrode geometry to the early detection of breast cancer.

This thesis consists of five chapters. Beginning with an overview of EIT and a review of breast cancer detection, the application of EIT to breast cancer detection is introduced in Chapter 1. In Chapter 2, the forward problem using an analytical method in EIT is presented, that is, the analytical solutions of the mathematical models (gap model, ave-gap model and complete electrode model) in the 2-D circular and 3-D mammography geometries are discussed. And the characteristic resistance is presented to evaluate the accuracy of the mathematical models. In Chapter 3, derivation of the Jacobian matrix for the analytical solution and synthesized voltages for combining with the complex data is discussed. The reconstruction algorithms are also presented. Experimental studies are discussed in Chapter 4. In Chapter 5, the results of the thesis are summed up and suggestions for further development are given.

## II. The Forward Problem Using an Analytical Method in EIT

In EIT, small currents are injected through electrodes placed on the surface  $S$  of a body  $\Omega$  and the corresponding voltages are measured through these electrodes. The forward problem in electrical impedance imaging is to compute the voltages on the boundary  $S$  of the body  $\Omega$  given the internal admittivity (impedivity) distribution and applied currents.

In this chapter, the 2-D circular and 3-D mammography geometries are considered. In the 2-D circular geometry, we try to find the analytical solutions of the electrode mathematical models: gap model, ave-gap model and complete electrode (CE) model. The Rensselaer group has mainly used the gap model for the imaging reconstructions. Somersalo *et al.* (1992) introduced the solution of the CE model using the coercive bilinear form. In the section 2.2, we try to find the analytical solution of the CE model in another approach. In the 3-D mammography geometry, we try to find the analytical solutions of the electrode mathematical models: gap model, ave-gap model. Choi *et al.* (2004) presented a simplified mammography geometry model which has  $4 \times 4$  electrode arrays on the top and bottom planes (32-electrode) using the ave-gap model. In the section 2.3, we reproduce Choi *et al.*'s study and designed a new test phantom with  $6 \times 6$  electrode array on the top and bottom planes (four electrodes on each array are disconnected in the experimental study for the 64-electrode system).

### 2.1 Physical Model in EIT

The physical relationship between the internal admittivity (impedivity)

distribution and the boundary voltages is governed by a partial differential equation with appropriate boundary conditions. Mathematically, this can be formulated as follows: If  $u(p)$  is the electric potential and  $\gamma(p)$  is the internal admittivity distribution in the body  $\Omega$ , then  $u(p)$  satisfies

$$\nabla \cdot \gamma(p) \nabla u(p) = 0, \quad \text{for } p \text{ in } \Omega \quad (2.1)$$

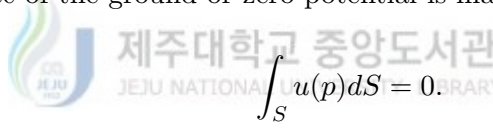
with boundary condition

$$\gamma(p) \frac{\partial u(p)}{\partial \nu} = j(p), \quad \text{for } p \text{ on } S \quad (2.2)$$

where  $\nu$  denotes the unit outward normal to the body and  $j(p)$  denotes the current density applied to the surface  $S$  of the body. The amount of current leaving the body must be the same as the amount entering (charge conservation theorem), which implies

$$\int_S j(p) dS = 0 \quad (2.3)$$

and a choice of the ground or zero potential is made



$$\int_S u(p) dS = 0. \quad (2.4)$$

## 2.2 2-D Circular Geometry

In this section, we consider the 2-D circular geometry which is a simple and well-studied geometry in the EIT field, and is depicted in Figure 2.1.

In Figure 2.1, the configuration of the  $\ell$ -th electrode  $e_\ell$  will be defined as

$$e_\ell = \left\{ (r_0, \theta) \mid \theta_\ell - \frac{f\Delta\theta}{2} \leq \theta \leq \theta_\ell + \frac{f\Delta\theta}{2} \right\} \quad (2.5)$$

where  $r_0$  denotes the radius of this geometry,  $\theta_\ell$  denotes the angle of the center

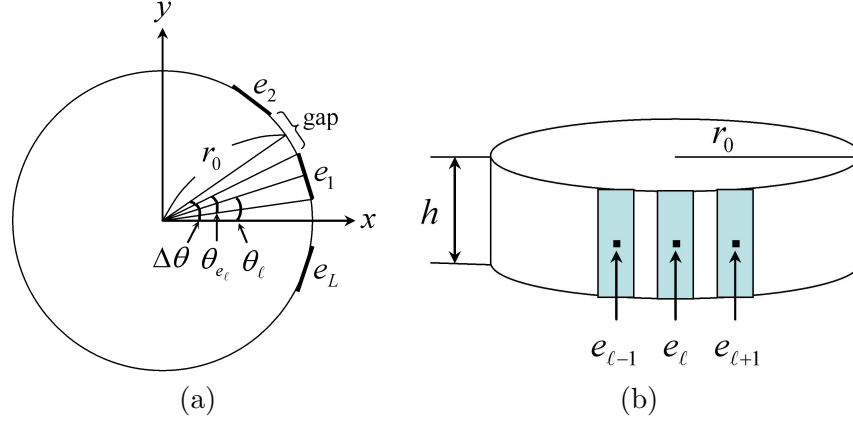


Figure 2.1: Description of the 2-D circular geometry (a) top view and (b) side view.

position of the  $\ell$ -th electrode and the angular fraction  $f$  is defined as

$$f \equiv \frac{\theta_{e_\ell}}{\Delta\theta} \quad (0 \leq f \leq 1) \quad (2.6)$$

where  $\theta_{e_\ell}$  denotes the angle of the  $\ell$ -th electrode and  $\Delta\theta$  represents the angle of division into  $L$  equal parts, that is,  $\Delta\theta \equiv 2\pi/L$  ( $L$ : the number of electrodes).

And the area  $|e_\ell|$  of the  $\ell$ -th electrode can be expressed as

$$|e_\ell| = w \times h = r_0 f \Delta\theta h \quad (2.7)$$

where  $w = r_0 f \Delta\theta$  is the width of the electrode and  $h$  is the height.

### 2.2.1 Gap model

In practice, we cannot specify current densities, but rather only currents which are applied through electrodes. Therefore, the boundary condition (2.2) can be discretized using the gap model (Cheng *et al.* 1989, Cheney *et al.* 1990, Somersalo *et al.* 1992), in which the current density is assumed to be zero in the gaps between electrodes and is also assumed to be constant over the

electrode region as follows:

$$j(\theta) = \begin{cases} I_\ell/|e_\ell|, & \text{on } e_\ell, \quad \ell = 1, 2, \dots, L \\ 0, & \text{otherwise} \end{cases} \quad (2.8)$$

where  $I_\ell$  denotes the current sent to the  $\ell$ -th electrode  $e_\ell$ ,  $|e_\ell|$  represents the area of the  $\ell$ -th electrode and  $L$  is the number of electrodes.

If the measured voltages are assumed to have the values of the potential at the center of each electrode and the admittivity distribution  $\gamma$  is assumed to be a constant admittivity ( $\gamma_0$ ) as an initial guess, then the governing equation (2.1) can be expressed analytically by writing it in polar coordinates as follows

$$\nabla^2 u(r, \theta) = \frac{\partial^2 u(r, \theta)}{\partial r^2} + \frac{1}{r} \frac{\partial u(r, \theta)}{\partial r} + \frac{1}{r^2} \frac{\partial^2 u(r, \theta)}{\partial \theta^2} = 0. \quad (2.9)$$

By using separation of variables technique  $u(r, \theta) = R(r)\Theta(\theta)$  and substituting it into (2.9), we obtain the following equation

$$R_{rr}\Theta + \frac{1}{r}R_r\Theta + \frac{1}{r^2}R\Theta_{\theta\theta} = 0 \quad (2.10)$$

and rewriting (2.10),

$$\frac{r^2}{R} \left[ R_{rr} + \frac{1}{r}R_r \right] = -\frac{\Theta_{\theta\theta}}{\Theta} = \xi \quad (2.11)$$

then the left-hand side will be a function of  $r$  and the right-hand side will be a function of  $\theta$  in (2.11), and for this equality to hold, the expression should be a constant. Therefore, we obtain the following ordinary differential equations

$$\Theta_{\theta\theta} + \xi\Theta = 0 \quad (2.12)$$

$$R_{rr} + \frac{1}{r}R_r - \frac{1}{r^2}\xi R = 0. \quad (2.13)$$

Here, the solution of (2.12) should be of the form

$$\Theta(\theta) = A \cos(\sqrt{\xi}\theta) + B \sin(\sqrt{\xi}\theta) \quad (2.14)$$

and  $u(r, \theta)$  is periodic with period  $2\pi$ ,  $\Theta(\theta + 2\pi) = \Theta(\theta)$ . So, a constant  $\xi$  will be

$$\sqrt{\xi} = n, \quad \xi = n^2, \quad n = 0, 1, 2, \dots \quad (2.15)$$

From (2.13) and (2.15),

$$R_{rr} + \frac{1}{r}R_r - \frac{n^2}{r^2}R = 0. \quad (2.16)$$

Let the solution of (2.16) be of the form

$$R(r) = r^\alpha. \quad (2.17)$$

Substituting (2.17) into (2.16), we obtain the solution as follows

$$R(r) = \begin{cases} r^n + r^{-n}, & n = 1, 2, \dots \\ A \ln r + B, & n = 0 \end{cases}. \quad (2.18)$$

In this solution,  $r^{-n}$  and  $A \ln r$  are not the desired solution, because they are bounded at the center of the body where  $r = 0$ , and  $B$  must be zero to satisfy the ground condition (2.4). So the solution of (2.16) should be

$$R(r) = r^n, \quad n = 1, 2, \dots \quad (2.19)$$

Hence, from (2.14) and (2.19), we can obtain the main solution of (2.9)

$$u(r, \theta) = \sum_{n=1}^{\infty} r^n [A_n \cos(n\theta) + B_n \sin(n\theta)]. \quad (2.20)$$

This solution (2.20) should satisfy the boundary condition (2.2),

$$\gamma_0 \frac{\partial u(r_0, \theta)}{\partial r} = \gamma_0 \sum_{n=1}^{\infty} n r_0^{n-1} [A_n \cos(n\theta) + B_n \sin(n\theta)] = j(\theta). \quad (2.21)$$

Let the Fourier series expansion of  $j(\theta)$  be written as

$$j(\theta) = \sum_{n=1}^{\infty} [a_n \cos(n\theta) + b_n \sin(n\theta)] \quad (2.22)$$

where

$$a_n = \frac{1}{\pi} \int_0^{2\pi} \cos(n\theta) j(\theta) d\theta \quad (2.23)$$

$$b_n = \frac{1}{\pi} \int_0^{2\pi} \sin(n\theta) j(\theta) d\theta. \quad (2.24)$$

Substituting (2.22) into (2.21) and using integral identities, we obtain coefficients  $A_n$  and  $B_n$  in (2.21)

$$A_n = \frac{a_n}{\gamma_0 n r_0^{n-1}}, \quad B_n = \frac{b_n}{\gamma_0 n r_0^{n-1}} \quad (2.25)$$

and substituting (2.25) into (2.20), we can obtain the analytical solution as

$$u(r, \theta) = \frac{r_0}{\gamma_0} \sum_{n=1}^{\infty} \left(\frac{r}{r_0}\right)^n \frac{1}{n} [a_n \cos(n\theta) + b_n \sin(n\theta)]. \quad (2.26)$$

Now, we try to find the Fourier coefficients  $a_n$  and  $b_n$ . In (2.8), the current density can be rewritten as follows

$$j(\theta) = \sum_{l=1}^L \frac{I_l}{|e_l|} \chi_{e_l}(\theta) \quad (2.27)$$

where

$$\chi_{e_l}(\theta) = \begin{cases} 1, & \text{when } \theta_l - \frac{f\Delta\theta}{2} \leq \theta \leq \theta_l + \frac{f\Delta\theta}{2} \\ 0, & \text{otherwise} \end{cases}. \quad (2.28)$$

Substituting (2.27) into (2.23) and (2.24), we have

$$\begin{aligned}
a_n &= \frac{1}{\pi} \sum_{l=1}^L \frac{I_l}{|e_l|} \int_0^{2\pi} \cos(n\theta) \chi_{e_l}(\theta) d\theta \\
&= \frac{1}{\pi} \sum_{l=1}^L \frac{I_l}{|e_l|} \int_{\theta_l - f\Delta\theta/2}^{\theta_l + f\Delta\theta/2} \cos(n\theta) d\theta \\
&= \frac{2}{n\pi} \sin\left(n \frac{f\Delta\theta}{2}\right) \sum_{l=1}^L \frac{I_l}{|e_l|} \cos(n\theta_l) \tag{2.29}
\end{aligned}$$

$$\begin{aligned}
b_n &= \frac{1}{\pi} \sum_{l=1}^L \frac{I_l}{|e_l|} \int_0^{2\pi} \sin(n\theta) \chi_{e_l}(\theta) d\theta \\
&= \frac{1}{\pi} \sum_{l=1}^L \frac{I_l}{|e_l|} \int_{\theta_l - f\Delta\theta/2}^{\theta_l + f\Delta\theta/2} \sin(n\theta) d\theta \\
&= \frac{2}{n\pi} \sin\left(n \frac{f\Delta\theta}{2}\right) \sum_{l=1}^L \frac{I_l}{|e_l|} \sin(n\theta_l). \tag{2.30}
\end{aligned}$$

Therefore, when the  $k$ -th current  $I_k$  is injected through the  $\ell$ -th electrode  $e_\ell$ , the  $k$ -th voltage  $U_k(\theta_\ell)$  induced on the  $\ell$ -th electrode  $e_\ell$  in the gap model will be

$$U_k(\theta_\ell) = u_k(r_0, \theta_\ell) = \frac{r_0}{\gamma_0} \sum_{n=1}^{\infty} \frac{1}{n} [a_{n,k} \cos(n\theta_\ell) + b_{n,k} \sin(n\theta_\ell)] \tag{2.31}$$

where  $\theta_\ell = 2\pi\ell/L$  ( $\ell = 1, 2, \dots, L$ ),  $a_{n,k}$  and  $b_{n,k}$  represent the Fourier coefficients as

$$a_{n,k} = \frac{2}{n\pi} \sin\left(n \frac{f\Delta\theta}{2}\right) \sum_{l=1}^L \frac{I_{l,k}}{|e_l|} \cos(n\theta_l) \tag{2.32}$$

$$b_{n,k} = \frac{2}{n\pi} \sin\left(n \frac{f\Delta\theta}{2}\right) \sum_{l=1}^L \frac{I_{l,k}}{|e_l|} \sin(n\theta_l). \tag{2.33}$$

### 2.2.2 Ave-gap model

The ave-gap model has the same boundary condition (2.2) as in the gap



model and this model predicts the voltage on the electrode as the average of the potential on that electrode given by the gap model in (2.26), that is,

$$U(\theta_\ell) = \frac{1}{|e_\ell|} \int_{e_\ell} u(r_0, \theta_\ell) dS = \frac{1}{|e_\ell|} \int_{\theta_\ell - f\Delta\theta/2}^{\theta_\ell + f\Delta\theta/2} u(r_0, \theta_\ell) dS. \quad (2.34)$$

Therefore, when the  $k$ -th current  $I_k$  is injected through the  $\ell$ -th electrode  $e_\ell$ , the  $k$ -th voltage  $U_k(\theta_\ell)$  induced on that electrode in the ave-gap model will be

$$U_k(\theta_\ell) = \frac{2r_0^2 h}{\gamma_0 |e_\ell|} \sum_{n=1}^{\infty} \frac{1}{n^2} \sin\left(n \frac{f\Delta\theta}{2}\right) [a_{n,k} \cos(n\theta_\ell) + b_{n,k} \sin(n\theta_\ell)] \quad (2.35)$$

where the Fourier coefficients  $a_{n,k}$  and  $b_{n,k}$  are the same as (2.32) and (2.33), respectively.

The ave-gap model improves on the gap model, because the voltages in the gap model have values of the potential at the center of each electrode, while the voltages in the ave-gap model have average values of the potential on each electrode. Both the gap and ave-gap model still overestimates the resistivities because they ignore the shunting effect of the electrodes and also the surface impedances that arise due to the electro-chemical effect between the electrodes and the saline/body.



### 2.2.3 Complete electrode model

The complete electrode (CE) model is the most accurate electrode model for EIT since it takes into account both the shunting effect of the electrodes and the surface impedances between the electrodes and tissue (Cheng 1989, Somersalo *et al.* 1992, Vauhkonen 1997, Vauhkonen 2004). The CE model uses the same partial differential equation (2.1) inside the body  $\Omega$ , but it replaces the boundary condition (2.2) with

$$\int_{e_\ell} \gamma \frac{\partial u(r, \theta)}{\partial r} dS = I_\ell, \quad \ell = 1, 2, \dots, L \quad (2.36)$$

$$\gamma \frac{\partial u(r, \theta)}{\partial r} = 0 \quad \text{on } S \setminus \bigcup_{\ell=1}^L e_\ell \quad (2.37)$$

$$u(r, \theta) + z_\ell \gamma \frac{\partial u(r, \theta)}{\partial r} = U_\ell \quad \text{on } e_\ell, \ell = 1, 2, \dots, L \quad (2.38)$$

where  $z_\ell$  is the surface impedance between the  $\ell$ -th electrode and tissue,  $U_\ell$  is the voltage on the  $\ell$ -th electrode. In addition, the following two constraints for the injected currents and measured voltages are needed to ensure the existence and uniqueness of the solution, that is, currents  $I_\ell$  satisfy

$$\sum_{\ell=1}^L I_\ell = 0 \quad (2.39)$$

in order to satisfy the conservation of charge, and voltages  $U_\ell$  satisfy

$$\sum_{\ell=1}^L U_\ell = 0 \quad (2.40)$$

in order to specify the ground or zero potential.

For the solution of the CE model using the analytical method, the procedure starts with the variational formulation (weak form) of the problem such as the procedure in the FEM (Vauhkonen 1997, Vauhkonen 2004). For more information of the variational formulation for the CE model, see Somersalo *et al.* (1992). The variational form of the CE model is of form

$$B((u, U), (v, V)) = \sum_{\ell=1}^L I_\ell V_\ell \quad \text{for any } (v, V) \in H^1(\Omega) \quad (2.41)$$

where  $B((u, U), (v, V))$  is defined as

$$B((u, U), (v, V)) = \int_{\Omega} \gamma \nabla u \cdot \nabla v dp + \sum_{\ell=1}^L \frac{1}{z_\ell} \int_{e_\ell} (u - U_\ell)(v - V_\ell) dS. \quad (2.42)$$

The  $k$ -th solution  $u_k(r, \theta)$  in the analytical technique can be written in

the form

$$u_k(r, \theta) = \sum_{n=1}^{\infty} u_{n,k} \varphi_n(r, \theta) \approx \sum_{n=1}^N u_{n,k} \varphi_n(r, \theta) \quad (2.43)$$

where  $N$  denotes the max number for coefficients of Fourier series and  $\varphi_n(r, \theta)$  are the basis functions as follows:

$$\varphi_n(r, \theta) = r^n \cos(n\theta), \quad n = 1, 2, \dots, N/2 \quad (2.44)$$

$$\varphi_n(r, \theta) = r^{(n-N/2)} \sin\{(n - N/2)\theta\}, \quad n = N/2 + 1, \dots, N. \quad (2.45)$$

Here, as  $N$  increases, values of the basis functions become larger, which causes the system matrix to be singular. To avoid this singular problem, we need the radius mapping,  $0 \leq r \leq r_0 \mapsto 0 \leq \hat{r} \leq \hat{r}_0 (= 1)$ , where  $\hat{r} = r/r_0$ . Hence, we can consider the following boundary conditions in the unit circular body  $\hat{\Omega}$ .

$$\int_{\hat{e}_\ell} \gamma \frac{\partial u(\hat{r}, \theta)}{\partial \hat{r}} d\hat{S} = I_\ell, \quad \ell = 1, 2, \dots, L \quad (2.46)$$

$$\gamma \frac{\partial u(\hat{r}, \theta)}{\partial \hat{r}} = 0 \quad \text{on } \hat{S} \setminus \bigcup_{\ell=1}^L \hat{e}_\ell \quad (2.47)$$

$$u(\hat{r}, \theta) + \hat{z}_\ell \gamma \frac{\partial u(\hat{r}, \theta)}{\partial \hat{r}} = U_\ell \quad \text{on } \hat{e}_\ell, \quad \ell = 1, 2, \dots, L. \quad (2.48)$$

Here, we obtain the same solution  $u_k(\hat{r}, \theta)$  in the unit circular body  $\hat{\Omega}$  as the solution  $u_k(r, \theta)$  in the circular body  $\Omega$  whose radius is  $r_0$ , but the surface impedance  $z_\ell$  will be changed as  $\hat{z}_\ell = z_\ell/r_0$ . The basis functions can be rewritten as

$$\varphi_n(\hat{r}, \theta) = \hat{r}^n \cos(n\theta), \quad n = 1, 2, \dots, N/2 \quad (2.49)$$

$$\varphi_n(\hat{r}, \theta) = \hat{r}^{(n-N/2)} \sin\{(n - N/2)\theta\}, \quad n = N/2 + 1, \dots, N. \quad (2.50)$$

The  $k$ -th voltage  $U_k$  on the electrodes is approximated as

$$U_k = \sum_{\ell=1}^{L-1} \beta_{\ell,k} \mathcal{N}_\ell \quad (2.51)$$

where  $\mathcal{N}_1 = [1, -1, 0, \dots, 0]^T$ ,  $\mathcal{N}_2 = [1, 0, -1, 0, \dots, 0]^T \in \mathbb{R}^L$ , etc. This choice for  $\mathcal{N}_\ell$  is to make sure that the constraint (2.40) is fulfilled. This voltage  $U_k$  can be written in the matrix form as

$$U_k = \mathcal{N} \beta_k \quad (2.52)$$

where  $\mathcal{N} \in \mathbb{R}^{L \times (L-1)}$  is a sparse matrix such that

$$\mathcal{N} \equiv [\mathcal{N}_1, \mathcal{N}_2, \mathcal{N}_3, \dots, \mathcal{N}_{L-1}] = \begin{bmatrix} 1 & 1 & \cdots & 1 \\ -1 & 0 & \cdots & 0 \\ 0 & -1 & \cdots & 0 \\ \vdots & \vdots & \ddots & \vdots \\ 0 & 0 & \cdots & -1 \end{bmatrix}. \quad (2.53)$$

Now, substituting (2.43) and (2.51) into the variational formulation (2.41) and by choosing  $v = \varphi_m$  and  $V = \mathcal{N}_\ell$ , when the  $k$ -th current pattern  $I_k$  is applied to the unit circular body, we obtain the  $k$ -th system equation that can be written in the matrix form as

$$\mathcal{A} \mathbf{x}_k = f_k \quad (2.54)$$

where the solution  $\mathbf{x}_k \equiv [u_k, \beta_k]^T \in \mathbb{C}^{N+L-1}$ ,  $u_k = [u_{1,k}, u_{2,k}, \dots, u_{N,k}]^T$  and  $\beta_k = [\beta_{1,k}, \beta_{2,k}, \dots, \beta_{L-1,k}]^T$  are coefficients to be determined, and the data vector  $f_k \equiv [0, \tilde{I}_k]^T$ ,  $0 = [0, 0, \dots, 0]^T \in \mathbb{C}^N$  and  $\tilde{I}_k = [I_{1,k} - I_{2,k}, I_{1,k} - I_{3,k}, \dots, I_{1,k} - I_{L,k}]^T \in \mathbb{C}^{L-1}$ . Thus the solution  $\mathbf{x}_k$  can be solved as

$$\mathbf{x}_k = \mathcal{A}^{-1} f_k. \quad (2.55)$$

And the system matrix  $\mathcal{A} \in \mathbb{C}^{(N+L-1) \times (N+L-1)}$  is the block matrix of the form

$$\mathcal{A} \equiv \begin{bmatrix} \mathcal{Q} + \mathcal{B} & \mathcal{CN} \\ (\mathcal{CN})^T & \mathcal{N}^T \mathcal{DN} \end{bmatrix} \quad (2.56)$$

where

$$\mathcal{Q}_{n,m} \equiv \int_{\hat{\Omega}} \gamma_0 \nabla \varphi_n \cdot \nabla \varphi_m d\hat{\rho}, \quad n, m = 1, 2, \dots, N \quad (2.57)$$

$$\mathcal{B}_{n,m} \equiv \sum_{\ell=1}^L \frac{1}{\hat{z}_\ell} \int_{\hat{e}_\ell} \varphi_n \varphi_m d\hat{S}, \quad n, m = 1, 2, \dots, N \quad (2.58)$$

$$\mathcal{C}_{n,l} \equiv -\frac{1}{\hat{z}_l} \int_{\hat{e}_l} \varphi_n d\hat{S}, \quad n = 1, 2, \dots, N, \quad l = 1, 2, \dots, L$$

$$\mathcal{D}_{\ell,l} \equiv \begin{cases} \frac{|\hat{e}_\ell|}{\hat{z}_\ell}, & \ell = l \\ 0, & \ell \neq l \end{cases}, \quad \ell, l = 1, 2, \dots, L \quad (2.59)$$

where  $|\hat{e}_\ell|$  is the area of the  $\ell$ -th electrode in the unit circular body  $\hat{\Omega}$ . For another analytical forward solution, see Somersalo *et al.* (1992).

#### 2.2.4 Comparison of the characteristic resistance

The relationship between currents  $I$  and voltages  $V$  is experimentally determined to be linear. Thus we can write

$$V = Z(\zeta)I \quad (2.60)$$

where  $Z(\zeta)$  is called the impedance matrix which is the Neumann-to-Dirichlet map, that is, it maps currents to voltages. In this section, we only consider the real part of the impedance matrix, that is, the resistance matrix  $R(\rho)$ . The nonzero eigenvalues of  $R(\rho)$  are called the characteristic resistances  $\rho_k$ , and the corresponding eigenvectors are the characteristic currents  $T_k$  (Cheng *et al.* 1989), that is,

$$R(\rho) T_k = \rho_k T_k. \quad (2.61)$$

We order the characteristic resistances  $\rho_k$  and characteristic currents  $T_k$  by the convention

$$\rho_1 \geq \rho_2 \geq \rho_3 \geq \cdots \geq \rho_{L-1} \geq 0. \quad (2.62)$$

The characteristic currents  $T_k$  are orthonormal, that is,

$$\langle T_k, T_\tau \rangle = \sum_{\ell=1}^L T_{\ell,k} T_{\ell,\tau} = \delta_{k,\tau} \quad (2.63)$$

where the bracket  $\langle \cdot, \cdot \rangle$  denotes the inner product and  $\delta_{k,\tau}$  denotes the Kronecker delta, that is,  $\delta_{k,\tau} = 0$  for  $k \neq \tau$ ,  $\delta_{k,\tau} = 1$  for  $k = \tau$ . Therefore, an arbitrary current pattern  $I_\tau$  can be expanded as

$$I_\tau = \sum_{k=1}^{L-1} \langle I_\tau, T_k \rangle T_k \quad (2.64)$$

and the resulting voltage pattern  $V_\tau$  can be found by

$$V_\tau = R(\rho) I_\tau = R(\rho) \sum_{k=1}^{L-1} \langle I_\tau, T_k \rangle T_k = \sum_{k=1}^{L-1} \langle I_\tau, T_k \rangle \rho_k T_k. \quad (2.65)$$

In other words, in order to solve the model for arbitrary applied currents, we only need to find the characteristic current  $T_k$  and resistances  $\rho_k$ .

When the currents  $T_k$  are applied to the circular phantom and the corresponding voltages  $V_k$  are measured in millivolts, the characteristic resistances  $\rho_k^{\text{exp}}$  for experimental data can be found by

$$\rho_k^{\text{exp}} = \frac{\langle V_k, T_k \rangle}{\langle T_k, T_k \rangle}. \quad (2.66)$$

Figure 2.2 shows the computed characteristic resistances for the different mathematical models compared with experimental data. As can be expected, the continuum model and gap model overestimate the resistivity of the tank because they ignore the shunting effect of the electrodes and also the surface

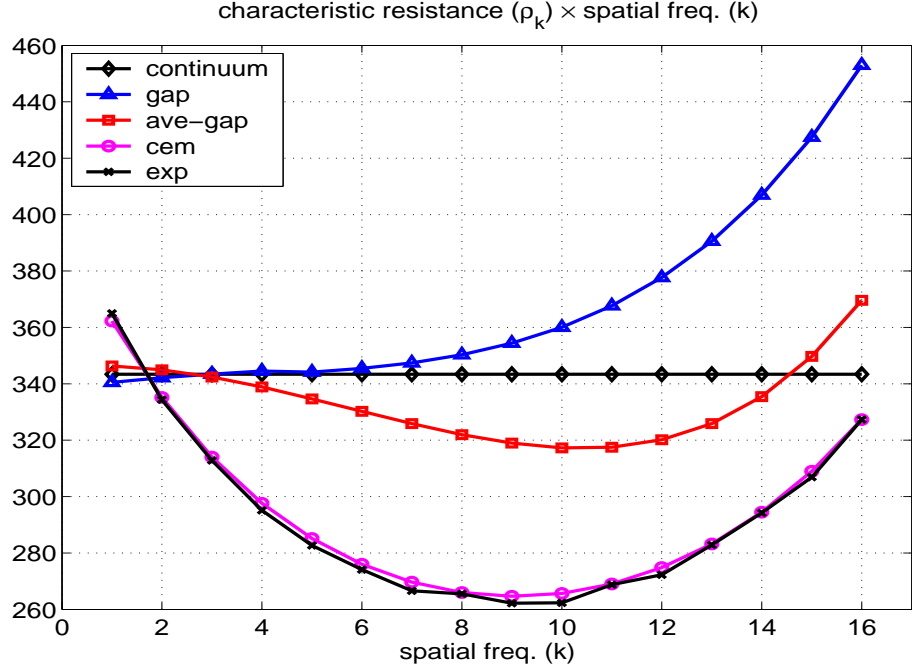
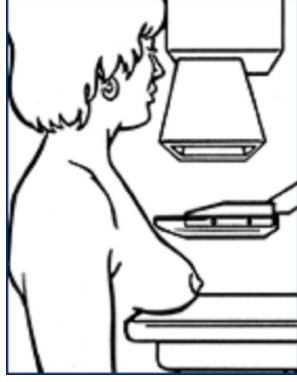


Figure 2.2: The product of characteristic resistance times spatial frequency is plotted versus spatial frequency for spatial frequencies between 1 and 16. Experimental measurements made with a homogeneous saline phantom of  $156.25 \Omega\text{-cm}$  resistivity are shown as asterisks.

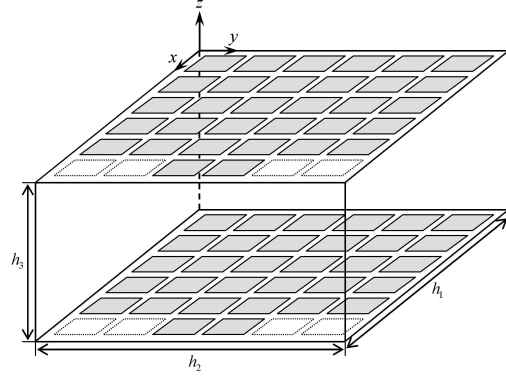
impedances. And the ave-gap model improves on the gap model because the voltages in the ave-gap model have average values of the potential on each electrode, but this model still overestimates the resistivity. The complete electrode (CE) model is the most accurate electrode model since it takes into account both the shunting effect of the electrodes and the surface impedances between the electrodes and the saline.

### 2.3 3-D Mammography Geometry

In this section, we consider the 3-D mammography geometry to image the impedance distribution of the breast. Figure 2.3 shows a schematic diagram of the X-ray mammography geometry and the simplified mammography



(a) X-ray mammography  
(American Cancer Society 2005b)



(b) The simplified model  
for the mammography geometry

Figure 2.3: Schematic diagram of the mammography geometry and its simplified model (a) In X-ray mammography, the breast is flattened by two plates and X-ray images are taken. (b) The mammography geometry is modeled as a rectangular box with electrodes on the top and bottom planes.

geometry model for the electrical impedance imaging. In the X-ray mammography, the breast is compressed between two radiolucent plates and two dimensional X-ray images of the breast are taken. In EIT, in order to image the impedance distribution of the breast, electrodes need to be placed so that they are in contact with upper and lower flattened surfaces of the breast. This simplified geometry is modeled as a rectangular box with electrodes on the top and bottom planes as shown in Figure 2.3(b).

In Figure 2.4, the configuration of the  $(a, b)$ -th electrode  $e_{(a,b)}$  will be defined as

$$e_{(a,b)} = \left\{ (x, y) \mid x_{(a,b)} - \frac{l_x}{2} \leq x \leq x_{(a,b)} + \frac{l_x}{2}, \quad y_{(a,b)} - \frac{l_y}{2} \leq y \leq y_{(a,b)} + \frac{l_y}{2} \right\} \quad (2.67)$$

where the center point  $(x_{(a,b)}, y_{(a,b)})$  of the  $(a, b)$ -th electrode  $e_{(a,b)}$  will be

$$x_{(a,b)} = \delta x_2 + (a-1) \times \delta x + \frac{2a-1}{2} \times l_x, \quad y_{(a,b)} = \delta y_2 + (b-1) \times \delta y + \frac{2b-1}{2} \times l_y \quad (2.68)$$



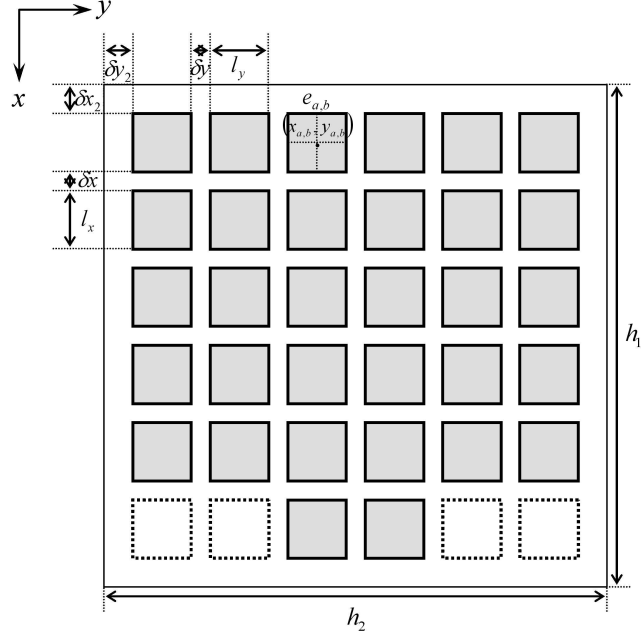


Figure 2.4: Description of the top plane with 32 electrodes in the 3-D mammography geometry. The shaded squares represent the electrodes.

where  $a = 1, 2, \dots, L_x$ ,  $b = 1, 2, \dots, L_y$ ,  $L_x$  and  $L_y$  are the number of the electrodes,  $\delta x$  and  $\delta y$  are length of gaps between electrodes,  $\delta x_2$  and  $\delta y_2$  are length of gaps between the electrode and edge,  $l_x$  and  $l_y$  are length of the electrode in  $x$ -,  $y$ -direction, respectively at the top plane. And the bottom plane has the same description of the electrodes as the top plane.

### 2.3.1 Gap model

The boundary condition (2.2) can be discretized using the gap model, in which the current density is assumed to be zero in the gaps between electrodes and be constant over the electrode region as follows:

$$j(x, y) = \begin{cases} I_{(a,b)} / |e_{(a,b)}|, & \text{on } e_{(a,b)}, \quad a = 1, 2, \dots, L_x, \quad b = 1, 2, \dots, L_y \\ 0, & \text{otherwise} \end{cases} \quad (2.69)$$

where  $I_{(a,b)}$  denotes the current sent to the  $(a,b)$ -th electrode  $e_{(a,b)}$ ,  $|e_{(a,b)}|$  represents the area of the  $(a,b)$ -th electrode.

If the measured voltages are assumed to have the values of the potential at the center of each electrode and the admittivity distribution  $\gamma$  is assumed to be a constant admittivity ( $\gamma_0$ ) as an initial guess, then the governing equation (2.1) can be expressed as follows

$$\nabla^2 u(x, y, z) = 0, \quad 0 \leq x \leq h_1, \quad 0 \leq y \leq h_2, \quad -h_3 \leq z \leq 0 \quad (2.70)$$

where  $h_1, h_2, h_3$  are the dimensions of the mammography geometry model as illustrated in Figure 2.3(b). Here, the current is assumed to flow only from the electrodes on the top plane to the electrodes on the bottom plane and it is assumed that no current can flow through the side walls of the rectangular tank. Hence, this replaces the boundary condition (2.2) with

$$\gamma_0 \frac{\partial u(x, y, z)}{\partial x} \Big|_{x=0} = 0, \quad \gamma_0 \frac{\partial u(x, y, z)}{\partial x} \Big|_{x=h_1} = 0 \quad (2.71)$$

$$\gamma_0 \frac{\partial u(x, y, z)}{\partial y} \Big|_{y=0} = 0, \quad \gamma_0 \frac{\partial u(x, y, z)}{\partial y} \Big|_{y=h_2} = 0 \quad (2.72)$$

$$\gamma_0 \frac{\partial u(x, y, z)}{\partial z} \Big|_{z=0} = j^{\mathbb{T}}(x, y) \quad (2.73)$$

$$\gamma_0 \frac{\partial u(x, y, z)}{\partial(-z)} \Big|_{z=-h_3} = j^{\mathbb{B}}(x, y) \quad (2.74)$$

where the superscript  $\mathbb{T}$  and  $\mathbb{B}$  denote the top plane and bottom plane, respectively.

By using separation of variables technique  $u(x, y, z) = X(x)Y(y)Z(z)$  and substituting it into (2.70), we obtain the following equation

$$X_{xx}YZ + XY_{yy}Z + XYZ_{zz} = 0 \quad (2.75)$$

and rewriting (2.75),

$$\frac{X_{xx}}{X} = -\left(\frac{Y_{yy}}{Y} + \frac{Z_{zz}}{Z}\right) = -\xi_1 \quad (2.76)$$

then the left-hand side will be a function of  $x$ , and for this equation to be true, the expression should be a constant. Therefore, we obtain the following ordinary differential equation with respect to  $x$

$$X_{xx} + \xi_1 X = 0. \quad (2.77)$$

Here, the solution of (2.77) should be of the form

$$X(x) = A_x \cos(\sqrt{\xi_1}x) + B_x \sin(\sqrt{\xi_1}x). \quad (2.78)$$

After using the boundary condition (2.71),  $B_x = 0$  and a constant  $\xi_1$  is

$$\xi_1 = \left(\frac{n\pi}{h_1}\right)^2, \quad n = 0, 1, 2, \dots \quad (2.79)$$

Hence, the solution of (2.77) is

$$X_n(x) = A_x \cos\left(\frac{n\pi}{h_1}x\right), \quad n = 0, 1, 2, \dots \quad (2.80)$$

We can rewrite the right-hand side of (2.76) as follows

$$\frac{Y_{yy}}{Y} = \xi_1 - \frac{Z_{zz}}{Z} = -\xi_2. \quad (2.81)$$

Both sides of (2.81) must be a constant. Therefore, we obtain the following ordinary differential equation with respect to  $y$

$$Y_{yy} + \xi_2 Y = 0. \quad (2.82)$$

Here, the solution of (2.82) should be of the form

$$Y(y) = A_y \cos(\sqrt{\xi_2}y) + B_y \sin(\sqrt{\xi_2}y). \quad (2.83)$$

After using the boundary condition (2.72),  $B_y = 0$  and a constant  $\xi_2$  is

$$\xi_2 = \left(\frac{m\pi}{h_2}\right)^2, \quad m = 0, 1, 2, \dots \quad (2.84)$$

Hence, the solution of (2.82) is

$$Y_m(y) = A_y \cos\left(\frac{m\pi}{h_2}y\right), \quad m = 0, 1, 2, \dots \quad (2.85)$$

Looking at the top and bottom planes, from the right-hand side of (2.81),

$$\frac{Z_{zz}}{Z} = \xi_1 + \xi_2 = \left(\frac{n\pi}{h_1}\right)^2 + \left(\frac{m\pi}{h_2}\right)^2 = \lambda_{n,m}^2 \quad (2.86)$$

where

$$\lambda_{n,m} \equiv \sqrt{\left(\frac{n\pi}{h_1}\right)^2 + \left(\frac{m\pi}{h_2}\right)^2}, \quad n, m = 0, 1, 2, \dots \quad (2.87)$$

Rewriting (2.86), we obtain the following two equations with respect to  $z$

$$Z_{zz} - \lambda_{n,m}^2 Z = 0, \quad \text{when } n \neq 0 \text{ or } m \neq 0 \quad (2.88)$$

$$Z_{zz} = 0, \quad \text{when } n = 0 \text{ and } m = 0. \quad (2.89)$$

Solving for these equations (2.88) and (2.89),

$$Z_{n,m}(z) = \begin{cases} A_z \cosh(\lambda_{n,m}z) + B_z \sinh(\lambda_{n,m}z), & \text{when } n \neq 0 \text{ or } m \neq 0 \\ A_{z0} + B_{z0}z, & \text{when } n = 0 \text{ and } m = 0 \end{cases}. \quad (2.90)$$

Therefore, the linear combination of all the analytical solutions (2.80), (2.85) and (2.90) are of the form

$$u(x, y, z) = A_{0,0} + B_{0,0}z + \sum_{n \neq 0 | m \neq 0}^{\infty} [A_{n,m} \cosh(\lambda_{n,m}z) + B_{n,m} \sinh(\lambda_{n,m}z)] \cos(\lambda_n x) \cos(\lambda_m y) \quad (2.91)$$

where  $n \neq 0 | m \neq 0$  means  $n \neq 0$  or  $m \neq 0$ ,  $A_{0,0} \equiv A_x A_y A_z$ ,  $B_{0,0} \equiv B_x B_y B_z$ ,  $A_{n,m} \equiv A_x A_y A_z$ ,  $B_{n,m} \equiv B_x B_y B_z$ , and

$$\lambda_{n,m} \equiv \sqrt{\left(\frac{n\pi}{h_1}\right)^2 + \left(\frac{m\pi}{h_2}\right)^2}, \quad \lambda_n \equiv \frac{n\pi}{h_1}, \quad \lambda_m \equiv \frac{m\pi}{h_2}. \quad (2.92)$$

Next step is to find the coefficients  $A_{n,m}$  and  $B_{n,m}$ . We need the boundary conditions (2.73) and (2.74) to obtain these coefficients. At the top plane ( $z = 0$ ), differentiating (2.91) and substituting it into (2.73), we obtain

$$\gamma_0 \frac{\partial u(x, y, z)}{\partial z} \Big|_{z=0} = \gamma_0 B_{0,0} + \gamma_0 \sum_{n \neq 0 | m \neq 0}^{\infty} \lambda_{n,m} B_{n,m} \cos(\lambda_n x) \cos(\lambda_m y) = j^{\mathbb{T}}(x, y) \quad (2.93)$$

and taking double integral in both sides of (2.93), we obtain the coefficient

$$B_{0,0}, \quad B_{0,0} = \frac{j_{0,0}^{\mathbb{T}}}{\gamma_0}, \quad \text{when } n = 0 \text{ and } m = 0 \quad (2.94)$$

where

$$j_{0,0}^{\mathbb{T}} = \frac{1}{h_1 h_2} \int_0^{h_1} \int_0^{h_2} j^{\mathbb{T}}(x, y) dx dy. \quad (2.95)$$

After multiplying both sides of (2.93) by  $\cos(\lambda_{\bar{n}}x) \cos(\lambda_{\bar{m}}y)$ , taking double integral and using integral identities, we let  $j_{n,m}^{\mathbb{T}}$  denote the Fourier coefficient of  $j^{\mathbb{T}}(x, y)$  as

$$j_{n,m}^{\mathbb{T}} = \frac{4}{h_1 h_2} \int_0^{h_1} \int_0^{h_2} \cos(\lambda_n x) \cos(\lambda_m y) j^{\mathbb{T}}(x, y) dx dy \quad (2.96)$$

then we obtain the following coefficient  $B_{n,m}$ ,

$$B_{n,m} = \frac{j_{n,m}^{\mathbb{T}}}{\gamma_0 \lambda_{n,m}}, \quad \text{when } n \neq 0 \text{ and } m \neq 0 \quad (2.97)$$

$$B_{n,0} = \frac{j_{n,0}^{\mathbb{T}}}{\gamma_0 \lambda_{n,0}}, \quad \text{when } n \neq 0 \text{ and } m = 0 \quad (2.98)$$

$$B_{0,m} = \frac{j_{0,m}^{\mathbb{T}}}{\gamma_0 \lambda_{0,m}}, \quad \text{when } n = 0 \text{ and } m \neq 0 \quad (2.99)$$

where  $\lambda_{n,0} = \lambda_n$ ,  $\lambda_{0,m} = \lambda_m$  and

$$j_{n,0}^{\mathbb{T}} = \frac{2}{h_1 h_2} \int_0^{h_1} \int_0^{h_2} \cos(\lambda_n x) j^{\mathbb{T}}(x, y) dx dy \quad (2.100)$$

$$j_{0,m}^{\mathbb{T}} = \frac{2}{h_1 h_2} \int_0^{h_1} \int_0^{h_2} \cos(\lambda_m y) j^{\mathbb{T}}(x, y) dx dy. \quad (2.101)$$

Substituting (2.94) and (2.97) ~ (2.99) into (2.93), the current density on the top plane is obtained as

$$j^{\mathbb{T}}(x, y) = j_{0,0}^{\mathbb{T}} + \sum_{n \neq 0 | m \neq 0}^{\infty} j_{n,m}^{\mathbb{T}} \cos(\lambda_n x) \cos(\lambda_m y). \quad (2.102)$$

At the bottom plane ( $z = -h_3$ ), differentiating (2.91) and substituting it into (2.74), we obtain

$$\begin{aligned} \gamma_0 \frac{\partial u(x, y, z)}{\partial(-z)} \Big|_{z=-h_3} &= -\gamma_0 B_{0,0} \\ &\quad -\gamma_0 \sum_{n \neq 0 | m \neq 0}^{\infty} \lambda_{n,m} \begin{bmatrix} -A_{n,m} \sinh(\lambda_{n,m} h_3) \\ +B_{n,m} \cosh(\lambda_{n,m} h_3) \end{bmatrix} \cos(\lambda_n x) \cos(\lambda_m y) \\ &= j^{\mathbb{B}}(x, y) \end{aligned} \quad (2.103)$$

and the same expression as (2.102) for the current density on the bottom plane can be written as follows

$$j^{\mathbb{B}}(x, y) = j_{0,0}^{\mathbb{B}} + \sum_{n \neq 0 | m \neq 0}^{\infty} j_{n,m}^{\mathbb{B}} \cos(\lambda_n x) \cos(\lambda_m y). \quad (2.104)$$

Here, (2.103) and (2.104) must be the same. Hence, we obtain the coefficient  $A_{n,m}$ ,

$$A_{n,m} = \frac{1}{\gamma_0 \lambda_{n,m}} \left[ j_{n,m}^{\mathbb{T}} \frac{\cosh(\lambda_{n,m} h_3)}{\sinh(\lambda_{n,m} h_3)} + j_{n,m}^{\mathbb{B}} \frac{1}{\sinh(\lambda_{n,m} h_3)} \right]. \quad (2.105)$$

Therefore, by substituting the coefficients  $A_{n,m}$  and  $B_{n,m}$  into (2.91) and rewriting (2.91), we can obtain the main solution in a simpler form as

$$u(x, y, z) = u^{\mathbb{T}}(x, y, z) + u^{\mathbb{B}}(x, y, z) + u_{0,0}(x, y, z) \quad (2.106)$$

where

$$u^{\mathbb{T}}(x, y, z) = \frac{1}{\gamma_0} \sum_{n \neq 0 | m \neq 0}^{\infty} \frac{j_{n,m}^{\mathbb{T}} \cosh\{\lambda_{n,m}(h_3 + z)\}}{\lambda_{n,m} \sinh(\lambda_{n,m} h_3)} \cos(\lambda_n x) \cos(\lambda_m y) \quad (2.107)$$

$$u^{\mathbb{B}}(x, y, z) = \frac{1}{\gamma_0} \sum_{n \neq 0 | m \neq 0}^{\infty} \frac{j_{n,m}^{\mathbb{B}} \cosh(\lambda_{n,m} z)}{\lambda_{n,m} \sinh(\lambda_{n,m} h_3)} \cos(\lambda_n x) \cos(\lambda_m y) \quad (2.108)$$

$$u_{0,0}(x, y, z) = \frac{j_{0,0}^{\mathbb{T}}}{\gamma_0} z + A_{0,0} \quad (2.109)$$

where  $A_{0,0}$  is arbitrary since it is a ground potential, so we can choose it to be zero.

Now, we try to find the Fourier coefficient  $j_{n,m}$  of the current density on the top and bottom planes. In (2.69), the current density can be rewritten as follows

$$j^*(x, y) = \sum_{a=1}^{L_x^*} \sum_{b=1}^{L_y^*} \frac{I_{(a,b)}^*}{|e_{(a,b)}|} \chi_{e_{(a,b)}}(x, y) \quad (2.110)$$

where the superscript  $*$  =  $\mathbb{T}$  (top plane) or  $*$  =  $\mathbb{B}$  (bottom plane),  $|e_{(a,b)}^{\mathbb{T}}| = |e_{(a,b)}^{\mathbb{B}}| = |e_{(a,b)}|$  for all  $(a, b)$  and

$$\chi_{e_{(a,b)}}(x, y) = \begin{cases} 1, & \text{when } (x, y) \in e_{(a,b)} \\ 0, & \text{otherwise} \end{cases}. \quad (2.111)$$

Substituting (2.110) into (2.96),

$$\begin{aligned}
j_{n,m}^* &= \frac{4}{h_1 h_2} \sum_{a=1}^{L_x^*} \sum_{b=1}^{L_y^*} \frac{I_{(a,b)}^*}{|e_{(a,b)}|} \int_0^{h_1} \int_0^{h_2} \cos(\lambda_n x) \cos(\lambda_m y) \chi_{e_{(a,b)}}(x, y) dx dy \\
&= \frac{4}{h_1 h_2} \sum_{a=1}^{L_x^*} \sum_{b=1}^{L_y^*} \frac{I_{(a,b)}^*}{|e_{(a,b)}|} \mathcal{J}_{n,m}^{(a,b)}, \quad \text{when } n \neq 0 \text{ and } m \neq 0 \quad (2.112)
\end{aligned}$$


where

$$\begin{aligned}
\mathcal{J}_{n,m}^{(a,b)} &\equiv \int_0^{h_1} \int_0^{h_2} \cos(\lambda_n x) \cos(\lambda_m y) \chi_{e_{(a,b)}}(x, y) dx dy \\
&= \frac{4}{\lambda_n \lambda_m} \sin\left(\lambda_n \frac{l_x}{2}\right) \cos(\lambda_n x_{(a,b)}) \sin\left(\lambda_m \frac{l_y}{2}\right) \cos(\lambda_m y_{(a,b)}). \quad (2.113)
\end{aligned}$$

Substituting (2.110) into (2.100),

$$\begin{aligned}
j_{n,0}^* &= \frac{2}{h_1 h_2} \sum_{a=1}^{L_x^*} \sum_{b=1}^{L_y^*} \frac{I_{(a,b)}^*}{|e_{(a,b)}|} \int_0^{h_1} \int_0^{h_2} \cos(\lambda_n x) \chi_{e_{(a,b)}}(x, y) dx dy \\
&= \frac{2}{h_1 h_2} \sum_{a=1}^{L_x^*} \sum_{b=1}^{L_y^*} \frac{I_{(a,b)}^*}{|e_{(a,b)}|} \mathcal{J}_{n,0}^{(a,b)}, \quad \text{when } n \neq 0 \text{ and } m = 0 \quad (2.114)
\end{aligned}$$

where



$$\begin{aligned}
\mathcal{J}_{n,0}^{(a,b)} &\equiv \int_0^{h_1} \int_0^{h_2} \cos(\lambda_n x) \chi_{e_{(a,b)}}(x, y) dx dy \\
&= \frac{2l_y}{\lambda_n} \sin\left(\lambda_n \frac{l_x}{2}\right) \cos(\lambda_n x_{(a,b)}). \quad (2.115)
\end{aligned}$$

Substituting (2.110) into (2.101),

$$\begin{aligned}
j_{0,m}^* &= \frac{2}{h_1 h_2} \sum_{a=1}^{L_x^*} \sum_{b=1}^{L_y^*} \frac{I_{(a,b)}^*}{|e_{(a,b)}|} \int_0^{h_1} \int_0^{h_2} \cos(\lambda_m y) \chi_{e_{(a,b)}}(x, y) dx dy \\
&= \frac{2}{h_1 h_2} \sum_{a=1}^{L_x^*} \sum_{b=1}^{L_y^*} \frac{I_{(a,b)}^*}{|e_{(a,b)}|} \mathcal{J}_{0,m}^{(a,b)}, \quad \text{when } n = 0 \text{ and } m \neq 0 \quad (2.116)
\end{aligned}$$



where

$$\begin{aligned}\mathcal{J}_{0,m}^{(a,b)} &\equiv \int_0^{h_1} \int_0^{h_2} \cos(\lambda_m y) \chi_{e_{(a,b)}}(x, y) dx dy \\ &= \frac{2l_x}{\lambda_m} \sin\left(\lambda_m \frac{l_y}{2}\right) \cos(\lambda_m y_{(a,b)}).\end{aligned}\quad (2.117)$$

Substituting (2.110) into (2.95),

$$\begin{aligned}j_{0,0}^* &= \frac{1}{h_1 h_2} \sum_{a=1}^{L_x^*} \sum_{b=1}^{L_y^*} \frac{I_{(a,b)}^*}{|e_{(a,b)}|} \int_0^{h_1} \int_0^{h_2} \chi_{e_{(a,b)}}(x, y) dx dy \\ &= \frac{1}{h_1 h_2} \sum_{a=1}^{L_x^*} \sum_{b=1}^{L_y^*} \frac{I_{(a,b)}^*}{|e_{(a,b)}|} \mathcal{J}_{0,0}^{(a,b)}, \quad \text{when } n=0 \text{ and } m=0\end{aligned}\quad (2.118)$$

where

$$\mathcal{J}_{0,0}^{(a,b)} \equiv \int_0^{h_1} \int_0^{h_2} \chi_{e_{(a,b)}}(x, y) dx dy = l_x l_y = |e_{(a,b)}|. \quad (2.119)$$

Here,  $\mathcal{J}_{n,m}^{(a,b)}$ ,  $\mathcal{J}_{n,0}^{(a,b)}$ ,  $\mathcal{J}_{0,m}^{(a,b)}$ , and  $\mathcal{J}_{0,0}^{(a,b)}$  are independent of the currents, and can be pre-computed and stored.

Therefore, we can find the voltages on the top and bottom planes from the potential solution (2.106) in the mammography geometry. The boundary voltages  $U^{\mathbb{T}}(x, y)$  on the top plane ( $z=0$ ) are

$$\begin{aligned}U^{\mathbb{T}}(x, y) &= u(x, y, 0) = u^{\mathbb{T}}(x, y, 0) + u^{\mathbb{B}}(x, y, 0) + u_{0,0}(x, y, 0) \\ &= \frac{1}{\gamma_0} \sum_{n \neq 0 | m \neq 0}^{\infty} \frac{\cos(\lambda_n x) \cos(\lambda_m y)}{\lambda_{n,m}} \left[ \frac{j_{n,m}^{\mathbb{T}}}{\tanh(\lambda_{n,m} h_3)} + \frac{j_{n,m}^{\mathbb{B}}}{\sinh(\lambda_{n,m} h_3)} \right]\end{aligned}\quad (2.120)$$

and the voltages  $U^{\mathbb{T}}(x_{(a,b)}, y_{(a,b)})$  induced on the  $(a, b)$ -th electrode in the gap model are

$$\begin{aligned}
U_{(a,b)}^{\mathbb{T}} &= U^{\mathbb{T}}(x_{(a,b)}, y_{(a,b)}) \\
&= \frac{1}{\gamma_0} \sum_{n \neq 0 | m \neq 0}^{\infty} \frac{\cos(\lambda_n x_{(a,b)}) \cos(\lambda_m y_{(a,b)})}{\lambda_{n,m}} \left[ \frac{j_{n,m}^{\mathbb{T}}}{\tanh(\lambda_{n,m} h_3)} + \frac{j_{n,m}^{\mathbb{B}}}{\sinh(\lambda_{n,m} h_3)} \right].
\end{aligned} \tag{2.121}$$

And the boundary voltages  $U^{\mathbb{B}}(x, y)$  on the bottom plane ( $z = -h_3$ ) are

$$\begin{aligned}
U^{\mathbb{B}}(x, y) &= u(x, y, -h_3) = u^{\mathbb{T}}(x, y, -h_3) + u^{\mathbb{B}}(x, y, -h_3) + u_{0,0}(x, y, -h_3) \\
&= -\frac{j_{0,0}^{\mathbb{T}}}{\gamma_0} h_3 \\
&\quad + \frac{1}{\gamma_0} \sum_{n \neq 0 | m \neq 0}^{\infty} \frac{\cos(\lambda_n x) \cos(\lambda_m y)}{\lambda_{n,m}} \left[ \frac{j_{n,m}^{\mathbb{T}}}{\sinh(\lambda_{n,m} h_3)} + \frac{j_{n,m}^{\mathbb{B}}}{\tanh(\lambda_{n,m} h_3)} \right]
\end{aligned} \tag{2.122}$$

and the voltages  $U^{\mathbb{B}}(x_{(a,b)}, y_{(a,b)})$  induced on the  $(a, b)$ -th electrode are

$$\begin{aligned}
U_{(a,b)}^{\mathbb{B}} &= U^{\mathbb{B}}(x_{(a,b)}, y_{(a,b)}) \\
&= -\frac{j_{0,0}^{\mathbb{T}}}{\gamma_0} h_3 \\
&\quad + \frac{1}{\gamma_0} \sum_{n \neq 0 | m \neq 0}^{\infty} \frac{\cos(\lambda_n x_{(a,b)}) \cos(\lambda_m y_{(a,b)})}{\lambda_{n,m}} \left[ \frac{j_{n,m}^{\mathbb{T}}}{\sinh(\lambda_{n,m} h_3)} + \frac{j_{n,m}^{\mathbb{B}}}{\tanh(\lambda_{n,m} h_3)} \right].
\end{aligned} \tag{2.123}$$

### 2.3.2 Ave-gap model

The ave-gap model has the same boundary condition (2.71) ~ (2.74) and the same current density (2.69) as in the gap model and this model predicts the voltage on the electrode as the average of the potential on that electrode given by the gap model in (2.120) and (2.122), that is,

$$U^{\mathbb{T}}(x, y) = \frac{1}{|e_{(a,b)}^{\mathbb{T}}|} \iint_{e_{(a,b)}^{\mathbb{T}}} u(x, y, 0) dS, \quad \text{when } z = 0 \quad (2.124)$$

$$U^{\mathbb{B}}(x, y) = \frac{1}{|e_{(a,b)}^{\mathbb{B}}|} \iint_{e_{(a,b)}^{\mathbb{B}}} u(x, y, -h_3) dS, \quad \text{when } z = -h_3 \quad (2.125)$$

Therefore, the voltages  $U^{\mathbb{T}}(x_{(a,b)}, y_{(a,b)})$  induced on the  $(a, b)$ -th electrode at the top plane are

$$\begin{aligned} U_{(a,b)}^{\mathbb{T}} &= U^{\mathbb{T}}(x_{(a,b)}, y_{(a,b)}) \\ &= \frac{1}{\gamma_0 |e_{(a,b)}|} \sum_{n \neq 0 | m \neq 0}^{\infty} \frac{\mathcal{J}_{n,m}^{(a,b)}}{\lambda_{n,m}} \left[ \frac{j_{n,m}^{\mathbb{T}}}{\tanh(\lambda_{n,m} h_3)} + \frac{j_{n,m}^{\mathbb{B}}}{\sinh(\lambda_{n,m} h_3)} \right] \end{aligned} \quad (2.126)$$

and the voltages  $U^{\mathbb{B}}(x_{(a,b)}, y_{(a,b)})$  induced on the  $(a, b)$ -th electrode at the bottom plane are

$$\begin{aligned} U_{(a,b)}^{\mathbb{B}} &= U^{\mathbb{B}}(x_{(a,b)}, y_{(a,b)}) \\ &= -\frac{j_{0,0}^{\mathbb{T}}}{\gamma_0} h_3 + \frac{1}{\gamma_0 |e_{(a,b)}|} \sum_{n \neq 0 | m \neq 0}^{\infty} \frac{\mathcal{J}_{n,m}^{(a,b)}}{\lambda_{n,m}} \left[ \frac{j_{n,m}^{\mathbb{T}}}{\sinh(\lambda_{n,m} h_3)} + \frac{j_{n,m}^{\mathbb{B}}}{\tanh(\lambda_{n,m} h_3)} \right] \end{aligned} \quad (2.127)$$

where  $\mathcal{J}_{n,m}^{(a,b)}$ ,  $\mathcal{J}_{n,0}^{(a,b)}$ ,  $\mathcal{J}_{0,m}^{(a,b)}$ , and  $\mathcal{J}_{0,0}^{(a,b)}$  are given in (2.113), (2.115), (2.117), and (2.119), respectively.

## 2.4 Canonical Patterns

Since the applied current patterns have influence on the voltage measurement data which contains the information about the unknown admittivity distribution inside the body, it is necessary to apply specific current patterns that maximize the voltage signal. It is known that the current patterns that

maximize the voltage correspond to the eigenfunctions of the Neumann-to-Dirichlet map (Gisser *et al.* 1990, Isaacson 1986).

In this thesis, we compute the eigenfunctions that maximize the voltage signal for a homogeneous medium of the 3-D mammography geometry. The procedure for computing the canonical current patterns is as follows.

(i) Guess  $L-1$  orthonormal set of the current patterns  $I_k$  for which  $\sum_{\ell=1}^L I_{\ell,k} = 0$  and  $\langle I_k, I_\tau \rangle = \delta_{k,\tau}$  ( $k, \tau = 1, 2, \dots, L-1$ ).

(ii) Compute the voltages  $U_k$  ( $\sum_{\ell=1}^L U_{\ell,k} = 0$ ) that would result from applying  $I_k$  to the forward solver with a homogeneous admittivity distribution ( $\gamma_0 = 1$ ).

(iii) Compute the inner product of the applied currents  $I_\tau$  and the resulting voltages  $U_x$ .

$$R_{\tau,x} \equiv \langle I_\tau, U_x \rangle, \quad \tau, x = 1, 2, \dots, L-1. \quad (2.128)$$

(iv) Compute the eigenfunctions  $C_k$ , that is, eigenvectors of  $R$  in (2.128).

$$RC_k = \rho_k C_k, \quad \rho_1 \geq \rho_2 \geq \dots \geq \rho_{L-1} \geq 0. \quad (2.129)$$

(v) Compute the new current patterns  $I_k^{new}$  which are orthogonal

$$I_k^{new} = I_k C_k. \quad (2.130)$$

(vi) If the norm errors between  $\rho_k$  and  $\rho_k^{new}$  are less than the tolerance  $\varepsilon$ , that is,

$$\|\rho_k - \rho_k^{new}\| < \varepsilon \quad (2.131)$$

stop, otherwise replace  $I_k^{new}$  with  $I_k$  and go to step (ii).

(vii) Finally, scale the new current patterns  $I_k^{new}$  by the maximum amplitude allowed.

In this procedure, the new current patterns usually converge after 2 ~ 3

iterations. These canonical currents maximize the voltage signals for a given power. When using ACT4, we synthesize the voltages that would give rise to these currents and apply these voltages instead. When these canonical currents are normalized, we have the orthonormal set of the canonical currents,  $T_k$ . In the inverse algorithm, we use the orthonormal set of the canonical currents.



### III. The Inverse Problem in EIT

In EIT, given the injected current patterns and their corresponding voltage measurements, the inverse problem is to determine the admittivity (impedivity) distribution inside the body. The inverse problem is both ill-posed and nonlinear with respect to the admittivity distribution. Because of an ill-posedness, one has to consider the regularization method.

In this chapter, before the discussion of EIT reconstruction algorithms, computation of the Jacobian matrix in EIT is given. After this, reconstruction methods that are mainly used in the Rensselaer group, that is, linearization and NOSER algorithm are reviewed. And other reconstruction algorithms, that is, fast inversion algorithm and linearized Kalman filtering algorithm are introduced to find the admittivity (impedivity) distribution inside the body.

#### 3.1 Jacobian Matrix in EIT

In the inverse problem, the admittivity  $\gamma$  is assumed to be piecewise constant, which can be expressed as

$$\gamma(p) = \sum_{s=1}^{N_s} \gamma_s \chi_s(p) \quad (3.1)$$

where  $N_s$  is the number of the mesh elements,  $\chi_s(p)$  denotes the characteristic function, that is,  $\chi_s(p) = 1$  for  $p$  contained in the  $s$ -th mesh element  $\Omega_s$  and  $\chi_s(p) = 0$  otherwise. It will turn out to be more convenient to work with the impedivity  $\zeta$ , which is the reciprocal of the admittivity  $\gamma$ . Assumption (3.1) in terms of the impedivity is

$$\zeta(p) = \sum_{s=1}^{N_s} \zeta_s \chi_s(p). \quad (3.2)$$

In the inverse algorithm, the Jacobian, the derivative of the voltages  $U(\zeta)$  with respect to the impedivity distribution  $\zeta$  is required. The Jacobian matrix in EIT can be computed as follows. It is possible to write the  $k$ -th applied current patterns  $I_k$  in terms of the orthonormal basis current patterns  $T_\tau$  as

$$I_k = \sum_{\tau=1}^K \langle T_\tau, I_k \rangle T_\tau, \quad k = 1, 2, \dots, K \quad (3.3)$$

where  $K (= L - 1)$  is the number of the applied current patterns and the orthonormal basis current patterns  $T_\tau$  satisfy

$$\langle T_k, T_\tau \rangle = \sum_{l=1}^L T_{l,k} T_{l,\tau} = \delta_{k,\tau}, \quad k, \tau = 1, 2, \dots, K \quad (3.4)$$

where the bracket  $\langle \cdot, \cdot \rangle$  denotes the inner product and  $\delta_{k,\tau}$  denotes the Kronecker delta, that is,  $\delta_{k,\tau} = 0$  for  $k \neq \tau$ ,  $\delta_{k,\tau} = 1$  for  $k = \tau$ .

Multiplying both sides of (3.3) by the impedance matrix  $Z(\zeta)$  which is the Neumann-to-Dirichlet map, we obtain the following equation

$$U_k(\zeta) = Z(\zeta)I_k = \sum_{\tau=1}^K \langle T_\tau, Z(\zeta)I_k \rangle T_\tau = \sum_{\tau=1}^K \langle T_\tau, U_k(\zeta) \rangle T_\tau. \quad (3.5)$$

Differentiating (3.5) with respect to each  $\zeta_s$ , the derivative of the  $k$ -th voltages  $U_k(\zeta)$  becomes

$$\frac{\partial U_k(\zeta)}{\partial \zeta_s} = \sum_{\tau=1}^K \left\langle T_\tau, \frac{\partial U_k(\zeta)}{\partial \zeta_s} \right\rangle T_\tau. \quad (3.6)$$

Here, the Jacobian matrix is denoted  $J_{\ell,k}^s \equiv \partial U_{\ell,k}(\zeta) / \partial \zeta_s$  and it can be rewritten as

$$J_{\ell,k}^s \equiv \frac{\partial U_{\ell,k}(\zeta)}{\partial \zeta_s} = \sum_{\tau=1}^K \mathcal{R}_{k,\tau}^s T_{\ell,\tau} \quad (3.7)$$

where

$$\mathcal{R}_{k,\tau}^s \equiv \left\langle T_\tau, \frac{\partial U_k(\zeta)}{\partial \zeta_s} \right\rangle \quad (3.8)$$


and  $\mathcal{R}_{k,\tau}^s$  can be computed as follows

$$\mathcal{R}_{k,\tau}^s \equiv \left\langle T_\tau, \frac{\partial U_k(\zeta)}{\partial \zeta_s} \right\rangle = \left\langle \frac{\partial U_k(\zeta)}{\partial \zeta_s}, T_\tau \right\rangle \approx \frac{1}{\zeta_s^2} \int_{\Omega_s} \nabla u_k(\zeta) \cdot \nabla u_\tau(\zeta) dp \quad (3.9)$$

where  $\Omega_s$  is the  $s$ -th mesh element and  $u_k(\zeta)$  is the solution to the problem (Cheney *et al.* 1990).

### 3.1.1 Gap model and ave-gap model

Let  $\zeta_0$  denote the impedivity distribution in a homogeneous medium. Given that the  $k$ -th current  $T_k$  in the orthonormal set of the basis functions (canonical currents) is applied to the body, it can be shown that the  $k$ -th potential  $u_k$  is proportional to the  $k$ -th potential arising from a constant distribution of one. This fact is independent of the three models typically used for calculating the boundary voltages: continuum model, gap model and ave-gap model. Hence, it is possible to write the forward solution as



$$u_k(\zeta_0) = \zeta_0 u_k(1) \quad (3.10)$$

where  $u_k(1)$  represents the forward solution that the impedivity inside the body is constant and equal to 1. Therefore,  $\mathcal{R}_{k,\tau}^s$  in (3.9) can be rewritten simply as

$$\mathcal{R}_{k,\tau}^s = \int_{\Omega_s} \nabla u_k(1) \cdot \nabla u_\tau(1) dp. \quad (3.11)$$

Note that the matrix  $\mathcal{R}$  is independent of the measured voltage data, so it can be pre-computed and stored for use with other reconstructions in the same geometry.



### 3.1.2 Complete electrode model

Let  $u_k(\zeta_0)$  denote the  $k$ -th potential in a homogeneous medium, given that the  $k$ -th orthonormal basis current  $T_k$  is applied to the body. In the CE model, the  $k$ -th analytical solution  $u_k(\zeta_0)$  in (2.43) can be written as

$$u_k(\zeta_0) = \sum_{n=1}^N u_{n,k}(\zeta_0)\varphi_n. \quad (3.12)$$

Substituting this solution (3.12) into the right-hand side of (3.9), we have

$$\begin{aligned} \mathcal{R}_{k,\tau}^s &= \frac{1}{\zeta_0^2} \int_{\Omega_s} \nabla u_k(\zeta_0) \cdot \nabla u_\tau(\zeta_0) dp \\ &= \frac{1}{\zeta_0^2} \int_{\Omega_s} \nabla \left( \sum_{n=1}^N u_{n,k}(\zeta_0)\varphi_n \right) \cdot \nabla \left( \sum_{m=1}^N u_{m,\tau}(\zeta_0)\varphi_m \right) dp \\ &= \frac{1}{\zeta_0^2} \sum_{n=1}^N \sum_{m=1}^N u_{n,k}(\zeta_0)u_{m,\tau}(\zeta_0) \int_{\Omega_s} \nabla \varphi_n \cdot \nabla \varphi_m dp \end{aligned} \quad (3.13)$$

where  $u_{n,k}(\zeta_0)$  and  $u_{m,\tau}(\zeta_0)$  can be obtained from (2.55).

### 3.2 Linearization

The linearization approach as the 3-D reconstruction algorithm was introduced by Mueller *et al.* (1999) to determine the conductivity distribution using a single  $4 \times 4$  rectangular electrode array. This algorithm is based on the assumption that the spatially varying admittivity  $\gamma$  differs only slightly from a constant admittivity  $\gamma_0$  by a perturbation  $\eta$  that is small in magnitude relative to  $\gamma_0$ .

When the  $k$ -th current pattern is applied to the body, the solution  $u_k(\gamma, p) = u_k(\gamma)$  and the boundary condition to the inhomogeneous forward problem from (2.1) and (2.2) are

$$\nabla \cdot \gamma(p)\nabla u_k(\gamma) = 0, \quad \text{for } p \text{ in } \Omega \quad (3.14)$$

$$\gamma(p) \frac{\partial u_k(\gamma)}{\partial \nu} = j_k(p), \quad \text{for } p \text{ on } S \quad (3.15)$$

and when the  $\tau$ -th current pattern is applied, the solution  $u_\tau(\gamma_0, p) = u_\tau(\gamma_0)$  and the boundary condition to the homogeneous forward problem from (2.1) and (2.2) are

$$\nabla \cdot \gamma_0 \nabla u_\tau(\gamma_0) = 0, \quad \text{for } p \text{ in } \Omega \quad (3.16)$$

$$\gamma_0 \frac{\partial u_\tau(\gamma_0)}{\partial \nu} = j_\tau(p), \quad \text{for } p \text{ on } S \quad (3.17)$$

where  $p = (r, \theta)$  for the 2-D circular geometry,  $p = (x, y, z)$  for the 3-D mammography geometry.

Multiplying (3.14) and (3.16) by  $u_\tau(\gamma_0)$  and  $u_k(\gamma)$ , respectively and taking the volume integral, we obtain

$$\int_{\Omega} [u_\tau(\gamma_0) \nabla \cdot \{\gamma \nabla u_k(\gamma)\} - u_k(\gamma) \nabla \cdot \{\gamma_0 \nabla u_\tau(\gamma_0)\}] dp = 0 \quad (3.18)$$

and an application of the divergence theorem yields

$$\int_S \left[ u_\tau(\gamma_0) \gamma \frac{\partial u_k(\gamma)}{\partial \nu} - u_k(\gamma) \gamma_0 \frac{\partial u_\tau(\gamma_0)}{\partial \nu} \right] dS = \int_{\Omega} \eta \nabla u_\tau(\gamma_0) \cdot \nabla u_k(\gamma) dp \quad (3.19)$$

where  $\eta \equiv \gamma - \gamma_0$ .

Let  $D_{k,\tau}$  be the term on the left-hand side of (3.19) as

$$D_{k,\tau} \equiv \int_S [u_\tau(\gamma_0) j_k - u_k(\gamma) j_\tau] dS. \quad (3.20)$$

Substituting the approximation of the current density (2.27) (for the 2-D circular geometry) or (2.110) (for the 3-D mammography geometry) into (3.20) and by applying the orthonormal basis current patterns  $T_k$  through the electrodes, in the ave-gap model, we have

$$\begin{aligned}
D_{k,\tau} &= \sum_{\ell=1}^L \left[ T_{\ell,k} \frac{1}{|e_\ell|} \int_{e_\ell} u_\tau(\gamma) dS - T_{\ell,\tau} \frac{1}{|e_\ell|} \int_{e_\ell} u_k(\gamma) dS \right] \\
&= \sum_{\ell=1}^L [T_{\ell,k} U_{\ell,\tau}(\gamma) - T_{\ell,\tau} V_{\ell,k}(\gamma)]
\end{aligned} \tag{3.21}$$

where  $U_{\ell,\tau}(\gamma)$  is the  $\tau$ -th computed voltage on the  $\ell$ -th electrode in the homogeneous case and  $V_{\ell,k}(\gamma)$  is the  $k$ -th measured voltage on the  $\ell$ -th electrode in the inhomogeneous case. In the CE model, rewriting (2.38),

$$u_k(\gamma) = U_{\ell,k}(\gamma) - z_\ell \gamma \frac{\partial u_k(\gamma)}{\partial \nu} = U_{\ell,k}(\gamma) - z_\ell j_k \tag{3.22}$$

and substituting it into (3.20), we obtain

$$\begin{aligned}
D_{k,\tau} &= \sum_{\ell=1}^L \int_{e_\ell} [\{U_{\ell,\tau}(\gamma) - z_\ell j_\tau\} j_k - \{V_{\ell,k}(\gamma) - z_\ell j_k\} j_\tau] dS \\
&= \sum_{\ell=1}^L \int_{e_\ell} [U_{\ell,\tau}(\gamma) j_k - V_{\ell,k}(\gamma) j_\tau] dS \\
&= \sum_{\ell=1}^L [T_{\ell,k} U_{\ell,\tau}(\gamma) - T_{\ell,\tau} V_{\ell,k}(\gamma)]
\end{aligned} \tag{3.23}$$

On the right-hand side of (3.19), linearizing  $u_k(\gamma)$  about  $\gamma_0$ , it yields

$$u_k(\gamma) \approx u_k(\gamma_0) + \delta u_k(\gamma - \gamma_0) = u_k(\gamma_0) + \delta u_k(\eta) \tag{3.24}$$

where  $\delta u_k(\eta) = O(\eta)$ . Substituting this linearization (3.24) into the right-hand side of (3.19), we obtain

$$\begin{aligned}
D_{k,\tau} &= \int_{\Omega} \eta \nabla u_k(\gamma_0) \cdot \nabla u_\tau(\gamma_0) dp + O(\eta^2) \\
&\approx \int_{\Omega} \eta \nabla u_k(\gamma_0) \cdot \nabla u_\tau(\gamma_0) dp
\end{aligned} \tag{3.25}$$

where  $O(\eta^2)$  is close to zero as  $\eta$  is small ( $|\eta|/\gamma_0 \ll 1$ ). Here, we can guess that the data matrix  $D \in \mathbb{C}^{K \times K}$  is the symmetry matrix.

We can express  $\eta$  as a linear combination of the characteristic functions from (3.1)

$$\eta(p) = \sum_{s=1}^{N_s} \eta_s \chi_s(p) \quad (3.26)$$

and substituting it into (3.25), we obtain

$$\begin{aligned} D_{k,\tau} &= \int_{\Omega} \left( \sum_{s=1}^{N_s} \eta_s \chi_s(p) \right) \nabla u_k(\gamma_0) \cdot \nabla u_{\tau}(\gamma_0) dp \\ &= \sum_{s=1}^{N_s} \eta_s \int_{\Omega_s} \nabla u_k(\gamma_0) \cdot \nabla u_{\tau}(\gamma_0) dp \\ &= \sum_{s=1}^{N_s} \eta_s \mathcal{A}_{k,\tau}^s \end{aligned} \quad (3.27)$$

where

$$\begin{aligned} \mathcal{A}_{k,\tau}^s &\equiv \int_{\Omega_s} \nabla u_k(\gamma_0) \cdot \nabla u_{\tau}(\gamma_0) dp \\ &= \frac{1}{\gamma_0^2} \mathcal{R}_{k,\tau}^s \end{aligned} \quad (3.28)$$

where  $\mathcal{R}_{k,\tau}^s$  is computed from (3.9) in a homogeneous medium. Reshaping (3.27) to the vector form, it can be written in a simpler form as

$$\mathcal{A} \eta = D \quad (3.29)$$

where  $\mathcal{A} \in \mathbb{C}^{KK \times N_s}$ ,  $\eta \in \mathbb{C}^{N_s}$  and  $D \in \mathbb{C}^{KK}$ .

In EIT, the inverse problem is inherently ill-posed. Since the severe ill-posedness of the problem is evident in the distribution of the singular value of the matrix  $\mathcal{A}$ , it is necessary to regularize the matrix  $\mathcal{A}$  to make it well-conditioned. Therefore, we solve the following system

$$(\mathcal{A}^T \mathcal{A} + \alpha \mathcal{G}) \eta = \mathcal{A}^T D \quad (3.30)$$

instead of (3.29), where  $0 < \alpha < 1$  is a small regularization parameter and  $\mathcal{G} \in \mathbb{C}^{N_s \times N_s}$  is the regularization matrix. This method is equivalent to solving the least-squares minimization problem such as

$$\min_{\eta} [\|\mathcal{A}\eta - D\|_2^2 + \alpha \|\mathcal{G}\eta\|_2^2]. \quad (3.31)$$

Here, we choose the regularization matrix,  $\mathcal{G} = I$  (the identity matrix) for the Tikhonov regularization and  $\mathcal{G} = \text{diag}(\mathcal{A}^T \mathcal{A})$  for the NOSER-type regularization. Therefore, solving (3.30), we obtain this solution  $\eta$  as

$$\eta = (\mathcal{A}^T \mathcal{A} + \alpha \mathcal{G})^{-1} \mathcal{A}^T D. \quad (3.32)$$

### 3.3 Fast Inversion using a Spectral Representation

As we increase the number of electrodes, it takes more time to compute the admittivity distribution  $\gamma$  in the inverse problem. In this section, in order to reduce the computation time in the linearization method, we try to modify the linearization method using the eigenvector and eigenvalue in (3.32).

Rewriting the inversion term in (3.32), we have

$$\begin{aligned} (\mathcal{A}^T \mathcal{A} + \alpha \mathcal{G})^{-1} &= (\mathcal{A}^T \mathcal{A} + \alpha \mathcal{G}^{1/2} \mathcal{G}^{1/2})^{-1} \\ &= \left[ \mathcal{G}^{1/2} \left( \mathcal{G}^{-1/2} \mathcal{A}^T \mathcal{A} \mathcal{G}^{-1/2} + \alpha I \right) \mathcal{G}^{1/2} \right]^{-1} \\ &= \mathcal{G}^{-1/2} \left( \mathcal{G}^{-1/2} \mathcal{A}^T \mathcal{A} \mathcal{G}^{-1/2} + \alpha I \right)^{-1} \mathcal{G}^{-1/2} \\ &= \mathcal{G}^{-1/2} (\mathcal{P} + \alpha I)^{-1} \mathcal{G}^{-1/2} \end{aligned} \quad (3.33)$$

where  $I$  is the  $N_s \times N_s$  identity matrix, the regularization matrix  $\mathcal{G}$  is the

diagonal matrix and

$$\mathcal{P} \equiv \mathcal{G}^{-1/2} \mathcal{A}^T \mathcal{A} \mathcal{G}^{-1/2}. \quad (3.34)$$

Let  $\Psi^s$  and  $\psi_s$  be the  $s$ -th eigenvector and eigenvalue of the matrix  $\mathcal{P}$  in (3.34), respectively. Then we obtain

$$\mathcal{P} \Psi^s = \psi_s \Psi^s, \quad s = 1, 2, \dots, N_s \quad (3.35)$$

where  $\Psi^s = [\Psi_1^s, \Psi_2^s, \dots, \Psi_{N_s}^s]^T$  and since  $\Psi^s$  is the orthonormal basis function, it satisfies

$$\langle \Psi^s, \Psi^t \rangle = (\Psi^s)^T \Psi^t = \delta_{s,t} \quad (3.36)$$

where the bracket  $\langle \cdot, \cdot \rangle$  denotes the inner product and  $\delta_{s,t}$  is the Kronecker delta. Given any vector  $\phi$ , it can be expressed as follows:

$$\phi = \sum_{s=1}^{N_s} \Psi^s \langle \Psi^s, \phi \rangle = \sum_{s=1}^{N_s} \Psi^s (\Psi^s)^T \phi. \quad (3.37)$$

Now, using the eigenvector  $\Psi^s$  and eigenvalue  $\psi_s$  of the matrix  $\mathcal{P}$ , the inversion term in the right-hand side of (3.33), that is,  $(\mathcal{P} + \alpha I)^{-1}$  can be expressed as

$$(\mathcal{P} + \alpha I)^{-1} = \sum_{s=1}^{N_s} \frac{1}{\psi_s + \alpha} \Psi^s (\Psi^s)^T. \quad (3.38)$$

We can prove the above equation (3.38) using (3.35) and (3.37),

$$\begin{aligned}
I &= (\mathcal{P} + \alpha I) \sum_{s=1}^{N_s} \frac{1}{\psi_s + \alpha} \Psi^s (\Psi^s)^T & (3.39) \\
&= \sum_{s=1}^{N_s} \frac{1}{\psi_s + \alpha} (\mathcal{P} \Psi^s + \alpha I \Psi^s) (\Psi^s)^T \\
&= \sum_{s=1}^{N_s} \frac{1}{\psi_s + \alpha} (\psi^s \Psi^s + \alpha \Psi^s) (\Psi^s)^T \\
&= \sum_{s=1}^{N_s} \frac{\psi^s + \alpha}{\psi_s + \alpha} \Psi^s (\Psi^s)^T \\
&= \sum_{s=1}^{N_s} \Psi^s (\Psi^s)^T \\
&= I
\end{aligned}$$

where  $I$  is the identity matrix. Substituting (3.38) into (3.33), we obtain

$$(\mathcal{A}^T \mathcal{A} + \alpha \mathcal{G})^{-1} = \mathcal{G}^{-1/2} \left[ \sum_{s=1}^{N_s} \frac{1}{\psi_s + \alpha} \Psi^s (\Psi^s)^T \right] \mathcal{G}^{-1/2}. \quad (3.40)$$

Therefore, (3.32) can be modified as follows:

$$\begin{aligned}
\eta &= (\mathcal{A}^T \mathcal{A} + \alpha \mathcal{G})^{-1} \mathcal{A}^T D \\
&= \mathcal{G}^{-1/2} \left[ \sum_{s=1}^{N_s} \frac{1}{\psi_s + \alpha} \Psi^s (\Psi^s)^T \right] \mathcal{G}^{-1/2} \mathcal{A}^T D. & (3.41)
\end{aligned}$$

Here,  $\mathcal{A}$  and  $\mathcal{A}^T \mathcal{A}$  can be pre-computed off-line,  $\mathcal{G}^{-1/2}$ , the eigenvector  $\Psi^s$  and eigenvalue  $\psi_s$  of the matrix  $\mathcal{P}$  can also be pre-calculated. Note that we don't need to compute the inverse matrix in the inverse problem of (3.41), so it is possible to reduce the computation time with this approach in the real-time application.

### 3.4 NOSER Algorithm

The NOSER algorithm, called Newton's One Step Error Reconstructor used by the Impedance Imaging group at Rensselaer Polytechnic Institute, is a least squares method. This algorithm attempts to solve the inverse problem in EIT by employing one step of Newton's method to minimize the sum of the squared error between experimentally measured voltages and voltages calculated by a forward solver (Cheney *et al.* 1990).

#### 3.4.1 Formulation of the NOSER algorithm

Taking the sum of the squared difference between experimentally measured voltages  $V_k$  and voltages  $U_k(\zeta)$  obtained from a forward solution, the square error equation can be written as

$$\mathcal{E}(\zeta) = \sum_{k=1}^K \|V_k - U_k(\zeta)\|^2 = \sum_{k=1}^K \sum_{\ell=1}^L [V_{\ell,k} - U_{\ell,k}(\zeta)]^2 \quad (3.42)$$

where  $K$  is the number of applied patterns,  $L$  is the number of electrodes and  $\zeta$  is the impedivity distribution.

We consider the error equation (3.42) as a function of  $N_s$  variables,  $\zeta_1, \zeta_2, \dots, \zeta_{N_s}$  from (3.2). To minimize this function, we take the partial derivative with respect to the  $s$ -th variable  $\zeta_s$  and set it to zero:

$$\frac{\partial \mathcal{E}(\zeta)}{\partial \zeta_s} = -2 \sum_{k=1}^K \sum_{\ell=1}^L [V_{\ell,k} - U_{\ell,k}(\zeta)] \frac{\partial U_{\ell,k}(\zeta)}{\partial \zeta_s} = 0. \quad (3.43)$$

If we let  $F_s(\zeta)$  be the left-hand side of (3.43),

$$F_s(\zeta) \equiv \frac{\partial \mathcal{E}(\zeta)}{\partial \zeta_s} = -2 \sum_{k=1}^K \sum_{\ell=1}^L [V_{\ell,k} - U_{\ell,k}(\zeta)] \frac{\partial U_{\ell,k}(\zeta)}{\partial \zeta_s} \quad (3.44)$$



then we can write the following notation

$$F(\zeta) = [F_1(\zeta), F_2(\zeta), \dots, F_s(\zeta), \dots, F_{N_s}(\zeta)]^T = 0. \quad (3.45)$$

In the linearized approach, in order to obtain the solution of (3.45),  $F(\zeta)$  is approximated with the first order Taylor polynomial at the initial guess  $\zeta_0$  as

$$F(\zeta) = F(\zeta_0) + H(\zeta_0)(\zeta_{new} - \zeta_0) = 0 \quad (3.46)$$

where  $H(\zeta_0) \equiv F'(\zeta_0)$  is called the Hessian matrix. For the new parameter  $\zeta_{new}$ , rearranging this equation, then we can obtain the NOSER algorithm as

$$\zeta_{new} = \zeta_0 - [H(\zeta_0)]^{-1} F(\zeta_0) \quad (3.47)$$

and this is one step of Newton's method.

### 3.4.2 Determinations of $F(\zeta_0)$ and Hessian matrix $H(\zeta_0)$

Before computing the new parameter  $\zeta_{new}$  in the NOSER algorithm (3.47), we have to determine the quantities,  $F(\zeta_0)$  and  $H(\zeta_0)$ .

First, using the definition of the Jacobian  $J_{\ell,k}^s$  in (3.7), the component of  $F(\zeta_0)$  in (3.44) can be calculated as

$$\begin{aligned} F_s(\zeta_0) &= -2 \sum_{k=1}^K \sum_{\ell=1}^L [V_{\ell,k} - U_{\ell,k}(\zeta_0)] \frac{\partial U_{\ell,k}(\zeta_0)}{\partial \zeta_s} \\ &= -2 \sum_{k=1}^K \sum_{\ell=1}^L [V_{\ell,k} - U_{\ell,k}(\zeta_0)] J_{\ell,k}^s \end{aligned} \quad (3.48)$$

and applying the vector inner product notation, this equation can be rewritten as

$$F_s(\zeta_0) = -2 \sum_{k=1}^K \langle [V_k - U_k(\zeta_0)], J_k^s \rangle. \quad (3.49)$$

To find a component of the Hessian matrix  $H(\zeta_0)$ ,  $F_s(\zeta_0)$  must be dif-

ferentiated with respect to the  $t$ -th variable  $\zeta_t$ . Mathematically, this can be expressed as

$$\begin{aligned}
H_{s,t}(\zeta_0) &= \frac{\partial}{\partial \zeta_t} \frac{\partial \mathcal{E}(\zeta_0)}{\partial \zeta_s}, \quad s, t = 1, 2, \dots, N_s \\
&= 2 \sum_{k=1}^K \sum_{\ell=1}^L \frac{\partial U_{\ell,k}(\zeta_0)}{\partial \zeta_s} \frac{\partial U_{\ell,k}(\zeta_0)}{\partial \zeta_t} - 2 \sum_{k=1}^K \sum_{\ell=1}^L [V_{\ell,k} - U_{\ell,k}(\zeta_0)] \frac{\partial^2 U_{\ell,k}(\zeta_0)}{\partial \zeta_s \partial \zeta_t}.
\end{aligned} \tag{3.50}$$

Here, let  $\mathcal{A}_{s,t}$  be the first term of (3.50). Using the vector inner product identity and the definition of  $\mathcal{R}_{k,\tau}^s$  in (3.8), the first term of (3.50) can be manipulated as follows:

$$\begin{aligned}
\mathcal{A}_{s,t} &\equiv 2 \sum_{k=1}^K \sum_{\ell=1}^L \frac{\partial U_{\ell,k}(\zeta_0)}{\partial \zeta_s} \frac{\partial U_{\ell,k}(\zeta_0)}{\partial \zeta_t} \\
&= 2 \sum_{k=1}^K \sum_{\tau=1}^K \left\langle \frac{\partial U_k(\zeta_0)}{\partial \zeta_s}, T_\tau \right\rangle \left\langle \frac{\partial U_k(\zeta_0)}{\partial \zeta_t}, T_\tau \right\rangle \\
&= 2 \sum_{k=1}^K \sum_{\tau=1}^K \mathcal{R}_{k,\tau}^s \mathcal{R}_{k,\tau}^t.
\end{aligned} \tag{3.51}$$

The second term of (3.50) is more complicated to compute. However, if the initial guess  $\zeta_0$  is close to the true impedivity distribution  $\zeta$ , then the difference between the predicted voltages  $U_{\ell,k}(\zeta_0)$  and measured voltages  $V_{\ell,k}$  will be small. This fact produces the following approximation

$$\alpha \mathcal{A}_{s,t} \delta_{s,t} \tag{3.52}$$

where  $\delta_{s,t}$  is the Kronecker delta and the regularization parameter  $\alpha$  is employed to get around the ill-conditionedness of the Hessian matrix  $H(\zeta_0)$ . Therefore, the Hessian matrix can be rewritten as

$$H_{s,t}(\zeta_0) \approx \mathcal{A}_{s,t} + \alpha \mathcal{A}_{s,t} \delta_{s,t}. \tag{3.53}$$

### 3.5 Linearized Kalman Filter

We consider the underlying inverse problem as a state estimation problem to estimate the time-varying impedivity distribution. Suppose that a measurement has been made at time  $t_k$  and that the information it provides is to be applied in updating the estimate of the state of a system at time  $t_k$ . It is also assumed that the problem has been discretized with respect to the time variable.

#### 3.5.1 Formulation of the time-varying model

In the state estimation problem, we need the so-called time-varying (dynamic) model which consists of the state equation (the temporal evolution of the impedivity distribution) and the observation equation (the relationship between the impedivity distribution and voltage on the boundary). In general, the temporal evolution of the impedivity distribution  $\zeta_k$  in the body  $\Omega$  is assumed to be of the linear form

$$\zeta_{k+1} = \mathcal{F}_k \zeta_k + w_k \quad (3.54)$$

where  $F_k \in \mathbb{C}^{N_s \times N_s}$  is the state transition matrix at time  $t_k$  and  $N_s$  is the number of states (impedivity distribution). Usually in EIT, there is no *a priori* information on the time evolution of the impedivity distribution so we take  $\mathcal{F}_k \equiv I_{N_s}$  (the identity matrix) for all  $t_k$  to obtain the so-called random-walk model. It is assumed that  $w_k$  is white Gaussian noise with the following known covariance matrix  $\Gamma_k^w \in \mathbb{C}^{N_s \times N_s}$ ,

$$\Gamma_k^w \equiv E [w_k w_k^T] \quad (3.55)$$

which determines the rate of time evolution in the impedivity distribution.

Next, consider the observation model. Let  $V_k \in \mathbb{C}^L$ , defined as

$$V_k \equiv [V_{1,k}, V_{2,k}, \dots, V_{L,k}]^T \quad (3.56)$$

be the actual surface measurement voltages induced by the  $k$ -th current pattern. Then the relationship between the impedivity distribution and boundary voltages can be described by the following nonlinear mapping with measurement error

$$V_k = U_k(\zeta_k) + v_k \quad (3.57)$$

where the measurement error  $v_k \in \mathbb{C}^L$  is assumed to be white Gaussian noise.

Linearizing (3.57) about the nominal value (best impedivity value)  $\zeta_0 = 1/\gamma_0$ , we obtain

$$V_k = U_k(\zeta_0) + J_k(\zeta_0) (\zeta_k - \zeta_0) + \text{H.O.Ts} + v_k \quad (3.58)$$

where H.O.Ts represents the higher-order terms which are assumed to be additional white Gaussian noise, and  $J_k(\zeta_0) \in \mathbb{C}^{L \times N_s}$  is the Jacobian matrix defined by

$$J_k(\zeta_0) \equiv \left. \frac{\partial U_k}{\partial \zeta} \right|_{\zeta=\zeta_0} \quad (3.59)$$

and this Jacobian matrix  $J_k(\zeta_0)$  is computed in (3.7).

Let us define a pseudo-measurement as

$$y_k \equiv V_k - U_k(\zeta_0) + J_k(\zeta_0)\zeta_0 \quad (3.60)$$

then we obtain the following linearized measurement equation as

$$y_k = J_k(\zeta_0)\zeta_k + \bar{v}_k \quad (3.61)$$

where  $\bar{v}_k \in \mathbb{C}^L$  is assumed to be composed of the measurement and lineariza-

tion errors with the following known covariance as

$$\Gamma_k \equiv E [\bar{v}_k \bar{v}_k^T]. \quad (3.62)$$

### 3.5.2 Inverse solver based on the linearized Kalman filter

In the Kalman filtering approach we estimate the state vector  $\zeta_k$  on the basis of all the measurements taken up to the time  $t_k$ . With the Gaussian assumptions the required estimate is obtained by minimizing the cost functional which is formulated on the basis of the above state and measurement equations (3.54) and (3.61), respectively. The cost functional for the linearized Kalman filter (LKF) is of the form

$$\Xi(\zeta_k) = \frac{1}{2} \left[ \|\zeta_k - \zeta_0\|_{C_k^{-1}} + \|y_k - J_k(\zeta_0)\zeta_k\|_{\Gamma_k^{-1}} \right] \quad (3.63)$$

where  $\|x\|_A$  denotes  $x^T A x$ , and  $C_k \in \mathbb{C}^{N_s \times N_s}$  is the error covariance matrix, which is defined by

$$C_k \equiv E [(\zeta_k - \zeta_0)(\zeta_k - \zeta_0)^T]. \quad (3.64)$$

The two norms on the right-hand side in (3.63) refer to the weighted norms, having the inverse of the given covariances as weighting matrices.

By minimizing the cost functional (3.63), we can obtain the recursive linearized Kalman filtering algorithm. The relation of the filter to the EIT system is illustrated in the block diagram of Figure 3.1. The basic steps of the computational procedure for the Kalman estimator are as follows: (Gelb 1974, Grewal and Andrews 2001):

- time updating (prediction)

$$C_{k|k-1} = \mathcal{F}_{k-1} C_{k-1|k-1} \mathcal{F}_{k-1}^T + \Gamma_{k-1}^w \quad (3.65)$$

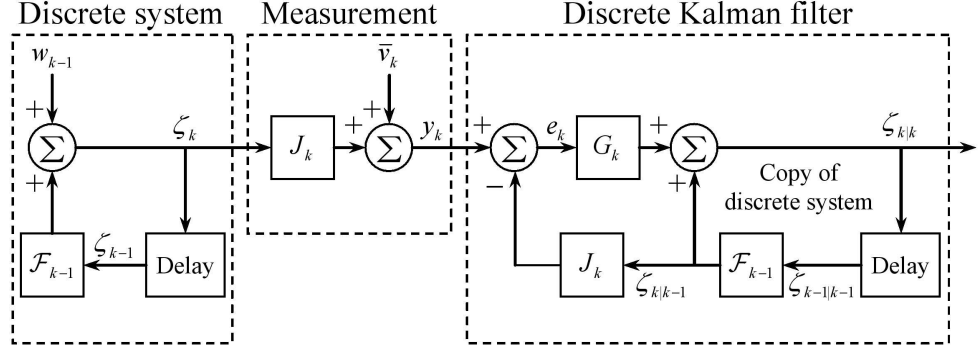


Figure 3.1: Block diagram of the time-varying model and Kalman filter.

$$\zeta_{k|k-1} = \mathcal{F}_{k-1} \zeta_{k-1|k-1} \quad (3.66)$$

- measurement updating (filtering)

$$G_k = C_{k|k-1} J_k^T (J_k C_{k|k-1} J_k^T + \Gamma_k)^{-1} \quad (3.67)$$

$$C_{k|k} = (I_{N_s} - G_k J_k) C_{k|k-1} \quad (3.68)$$

$$\zeta_{k|k} = \zeta_{k|k-1} + G_k (y_k - J_k \zeta_{k|k-1}). \quad (3.69)$$

Hence, we can find the estimated state vector  $\zeta_{k|k} \in \mathbb{C}^{N_s}$  for the true state vector  $\zeta_k$  in a recursive minimum mean square error sense. The Kalman gain matrix  $G_k \in \mathbb{C}^{N_s \times L}$  in (3.67) does not depend on the state vector, because the Jacobian matrix only depends on the nominal value  $\zeta_0$  in (3.59). Therefore, it is possible to pre-compute the error covariance extrapolation (3.65), Kalman gain matrix (3.67), and error covariance update (3.68) off-line and store the Kalman gain matrix for minimizing the on-line computational time.

The most striking feature is that the Kalman filtering technique is an on-line recursive form in place of the off-line batch form of the NOSER or modified Newton-Raphson algorithm. Therefore, there is no need to store the past measurements in order to estimate the present state.

### 3.6 Synthesized Voltages and Best Impedivity Approximation

Usually, in the EIT systems, current patterns are applied to the body and the corresponding voltages are measured through the electrodes. The reconstruction algorithms are developed on this concept. The ACT4 system under development at the Rensselaer group generates complex voltage sources that are injected into the body and the resulting complex current measurements are taken. In order to apply these complex data from the ACT4 system to the reconstruction algorithms, the means to find the synthesized voltages is introduced in this section.

#### 3.6.1 Finding synthesized complex voltages

In the complex algorithm, since all of the variables are complex numbers, the algorithm is more complicated and it takes some time to estimate the admittivity (impedivity) distribution. In this section, for simplicity and effective computation, we try to find the synthesized complex voltages  $W_k$  which are based on the orthonormal set of the real canonical currents  $T_k$  from the applied complex currents  $I_\tau$  and measured complex voltages  $V_\tau$ , or from the applied complex voltages  $V_\tau$  and measured complex currents  $I_\tau$ .

For the 2-D circular geometry, we consider the following orthonormal set of the trigonometric basis functions (canonical currents) (Edic 1994):

$$T_{\ell,k} = \begin{cases} c_k \cos(k\theta_\ell), & \ell = 1, \dots, L, k = 1, \dots, L/2 \\ s_k \sin((k - L/2)\theta_\ell), & \ell = 1, \dots, L, k = L/2 + 1, \dots, L - 1 \end{cases} \quad (3.70)$$

where

$$\theta_\ell = 2\pi\ell/L \quad (3.71)$$

$$c_k = \begin{cases} \sqrt{\frac{2}{L}}, & k = 1, 2, \dots, L/2 - 1 \\ \sqrt{\frac{1}{L}}, & k = L/2 \end{cases} \quad (3.72)$$

$$s_k = \sqrt{\frac{2}{L}}, \quad k = L/2 + 1, \dots, L - 1 \quad (3.73)$$

and for the 3-D mammography geometry, we also consider the orthonormal set of the canonical currents that were described in section 2.4. A set of these canonical currents  $T_k \in \mathbb{R}^L$  satisfy

$$\langle T_k, T_\tau \rangle = \sum_{\ell=1}^L T_{\ell,k} T_{\ell,\tau} = \delta_{k,\tau}, \quad k, \tau = 1, 2, \dots, K \quad (3.74)$$

where  $\delta_{k,\tau}$  denotes the Kronecker delta, that is,  $\delta_{k,\tau} = 0$  for  $k \neq \tau$ ,  $\delta_{k,\tau} = 1$  for  $k = \tau$ ,  $K$  is the number of applied patterns, and the bracket denotes the inner product.

An arbitrary complex current vector  $I_\tau \in \mathbb{C}^L$  can be represented as a weighted summation of normalized canonical current vectors. Since a set of these canonical current vectors is orthonormal, it is possible to write the following identity:

$$I_\tau = \sum_{k=1}^K \langle I_\tau, T_k \rangle T_k. \quad (3.75)$$

Multiplying both sides of (3.75) by the impedance matrix  $Z(\zeta)$  which is the Neumann-to-Dirichlet map, we obtain the following equation:

$$V_{\ell,\tau} = \sum_{k=1}^K P_{\tau,k} W_{\ell,k}, \quad \ell = 1, 2, \dots, L \quad (3.76)$$

where  $V_\tau \equiv Z(\zeta)I_\tau \in \mathbb{C}^L$ ,  $W_k \equiv Z(\zeta)T_k \in \mathbb{C}^L$ , and  $P_{\tau,k} \equiv \langle I_\tau, T_k \rangle \in \mathbb{C}^{K \times K}$ , and therefore, we can obtain the synthesized complex voltage  $W_k$  as follows

$$W_{\ell,k} = \sum_{\tau=1}^K Y_{k,\tau} V_{\ell,\tau}, \quad \ell = 1, 2, \dots, L \quad (3.77)$$

where  $Y \equiv P^{-1} \in \mathbb{C}^{K \times K}$ . These synthesized voltages should satisfy



$$\sum_{\ell=1}^L W_{\ell,k} = 0. \quad (3.78)$$

Now we can use the normalized canonical currents  $T_k$  and the synthesized complex voltages  $W_k$  in (3.77) instead of the complex currents  $I_\tau$  and complex voltages  $V_\tau$ , respectively, for all imaging reconstructions in the inverse problem. Hence, we can say that the normalized  $k$ -th canonical current  $T_k$  is applied to the body through the electrodes and the resulting complex voltage  $W_k$  is measured, and then an approximation to the impedivity (admittivity) distribution inside the body is estimated.

### 3.6.2 Finding the best constant impedivity approximation

The best constant impedivity approximation to the synthesized complex voltage data can be computed according to the following formula: Let  $\zeta_0$  denote the impedivity distribution in a homogeneous medium. Given that the  $k$ -th current is applied to the body, it can be shown that the  $k$ -th voltage on the  $\ell$ -th electrode is proportional to the  $k$ -th voltage arising from a constant distribution of one. Hence, it is possible to write the forward solution as

$$U_{\ell,k}(\zeta_0) = \zeta_0 U_{\ell,k}(1) \quad (3.79)$$

where  $U_{\ell,k}(1)$  represents the forward voltage that would be calculated on the  $\ell$ -th electrode and that the impedivity inside the body is constant and equal to 1.

To find the best fit to the data, we minimize the following error function

$$\mathcal{E}(\zeta) = \min_{\zeta_0} \sum_{k=1}^K \sum_{\ell=1}^L [W_{\ell,k} - \zeta_0 U_{\ell,k}(1)]^2. \quad (3.80)$$

Minimizing this error function  $\mathcal{E}(\zeta)$  with respect to  $\zeta_0$ , we have the following equation

$$\frac{\partial \mathcal{E}(\zeta)}{\partial \zeta_0} = -2 \left[ \sum_{k=1}^K \sum_{\ell=1}^L \{W_{\ell,k} - \zeta_0 U_{\ell,k}(1)\} U_{\ell,k}(1) \right] = 0. \quad (3.81)$$

Solving this equation for  $\zeta_0$ , the solution  $\zeta_0$  is given as

$$\zeta_0 = \frac{\sum_{k=1}^K \sum_{\ell=1}^L W_{\ell,k} U_{\ell,k}(1)}{\sum_{k=1}^K \sum_{\ell=1}^L U_{\ell,k}(1) U_{\ell,k}(1)}. \quad (3.82)$$

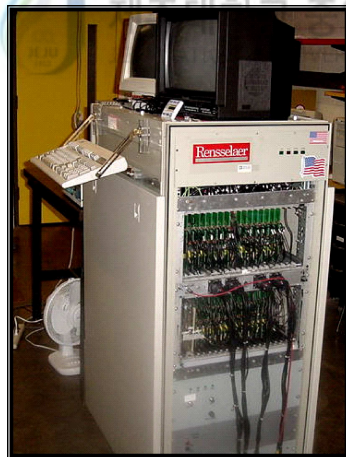


## IV. Experimental Studies

In this chapter, the 2-D circular and 3-D mammography geometries are considered for the experimental studies and the reconstruction algorithms are also applied to them. In the 2-D circular geometry, we evaluate performances of the reconstruction algorithms using FEM simulation data and experimental data. In the 3-D mammography geometry, we consider phantom studies for the breast cancer detection.

### 4.1 Experimental Setup

The ACT3 (adaptive current tomography) system in Figure 4.1(a) is a real-time impedance imaging device that has been used by the Rensselaer group. The ACT3 system (Cook *et al.* 1994, Edic *et al.* 1995) uses a 28.8 kHz current signal to sequentially apply 31 distinct current patterns to the



(a) ACT3



(b) ACT4

Figure 4.1: The ACT3 and ACT4 systems.

body. It measures both real and quadrature voltages on each electrode using 32 independent voltmeters. It has been used extensively to image ventilation and perfusion in human subjects.

The improved ACT4 system in Figure 4.1(b) is presently in its final stage of construction. The ACT4 system can support up to 64 electrodes with an excitation frequency that is selectable from a discrete set in the range from 300 Hz to 1 MHz for breast cancer detection (Ross 2003, Liu *et al.* 2005). The design specifications of both systems are shown in Table 4.1.

Table 4.1: Comparison of ACT3 and ACT4 design specifications (Ross 2003).

Feature	ACT3	ACT4
Current Sources	32	64
Voltage Sources	–	64
Voltmeters	32	64
$\mu$ Ammeters	–	64
Electrodes	32	64
Operating Frequency	28.8 kHz	300 Hz $\sim$ 1 MHz
Maximum Image Reconstruction Rate	20 frames/sec	30 frames/sec
System Precision	15 or 16 bits	$\geq$ 16 bits
Minimum distinguishable object	1 $\sim$ 3 cm	0.3 $\sim$ 1 cm



## 4.2 2-D Circular Geometry

In this section, we evaluated the reconstruction performances of the proposed algorithms using FEM simulation data and experimental data. In order to describe the admittivity distribution inside the body using the simulation and experimental data, the Joshua tree mesh (Cheney *et al.* 1990, Edic 1994) was used in the inverse problem and it was assumed that the admittivity is constant within each element.

The total number of independent current patterns is limited by the number of electrodes. Because of the conservation of charge (2.39), there are only 31 independent current patterns for a 32-electrode EIT system (63 indepen-

dent current patterns for a 64-electrode system). The best current patterns for a circularly symmetric admittivity distribution are the trigonometric current patterns in a circular geometry. Therefore, trigonometric current patterns are applied to the circular chest phantom through 32 electrodes. The trigonometric current patterns are of the form

$$I_{\ell,k} = \begin{cases} \cos(k\theta_\ell), & \ell = 1, \dots, L, k = 1, \dots, L/2 \\ \sin((k - L/2)\theta_\ell), & \ell = 1, \dots, L, k = L/2 + 1, \dots, L - 1 \end{cases} \quad (4.1)$$

where  $\theta_\ell = 2\pi\ell/L$  and these patterns make an orthogonal set of current patterns.

#### 4.2.1 Static imaging reconstruction

We considered the static imaging reconstruction which means that the internal admittivity distribution and the objects inside the body are time-invariant within the time required to acquire a full set of measurement data. For the static imaging reconstruction the linearization method was used to illustrate the reconstruction performances with different mathematical models. We compared the linearization method with the fast inversion algorithm with the goal of reducing the computational time. The range of conductivity and permittivity values in  $mS/m$  is given in the scale beneath each set of images. For the simulation data we computed voltages with the FEM and for the experimental data we obtained voltages with a chest phantom in a simplified geometry of the human chest.

##### 4.2.1.1 FEM simulation data

To generate the measured voltages on the electrodes, we computed the FEM forward solver and obtained complex voltages on the boundary using the 2-D EIDORS MATLAB demo version (Vauhkonen *et al.* 2001) in a simplified

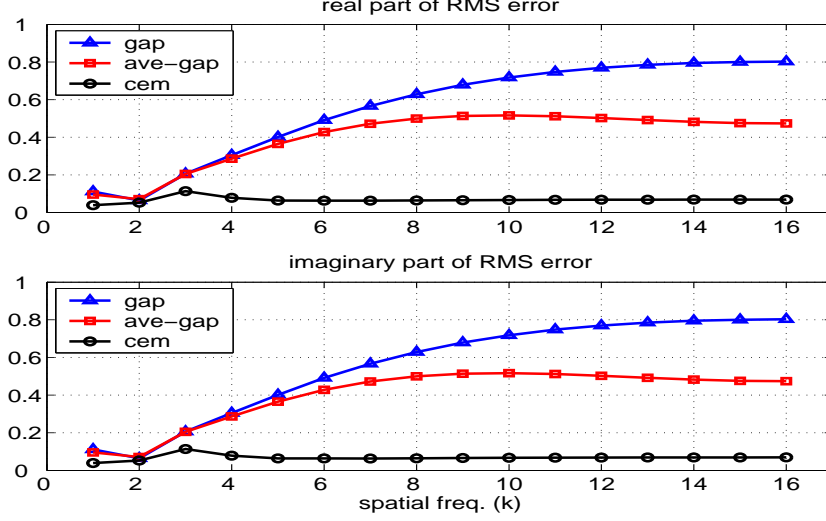


Figure 4.2: RMS (root-mean-square) errors for each mathematical model.

geometry of the human chest. For the FEM forward solver, we generated the forward fine mesh which has 3216 elements and 1737 nodes.

The geometry of the simulation phantom used was as follows: radius 15 *cm*, width of the electrode 2.54 *cm*, height 1 *cm*, and the amplitude of the currents 0.5 *mA*. The NOSER-type regularization was used and the regularization parameter  $\alpha$  was set to 0.1. The admittivity (impedivity) of the background was  $640 + i64 \text{ mS/m}$  ( $154.7 - i15.47 \text{ } \Omega\text{cm}$ ), the lungs  $400 + i40 \text{ mS/m}$  ( $247.5 - i24.75 \text{ } \Omega\text{cm}$ ), and the heart  $1500 + i150 \text{ mS/m}$  ( $66.0 - i6.60 \text{ } \Omega\text{cm}$ ).

To compare forward solutions calculated from each mathematical model with experimental data, we defined the RMS (root-mean-square) error as

$$RMSE(k) \equiv \sqrt{\frac{(V_k - U_k)^T (V_k - U_k)}{V_k^T V_k}} \quad (4.2)$$

where  $V_k$  is the measured voltage and  $U_k$  is the forward voltage calculated from each mathematical model. The RMS (root-mean-square) errors for each mathematical model are shown in Figure 4.2. It can be seen clearly that the

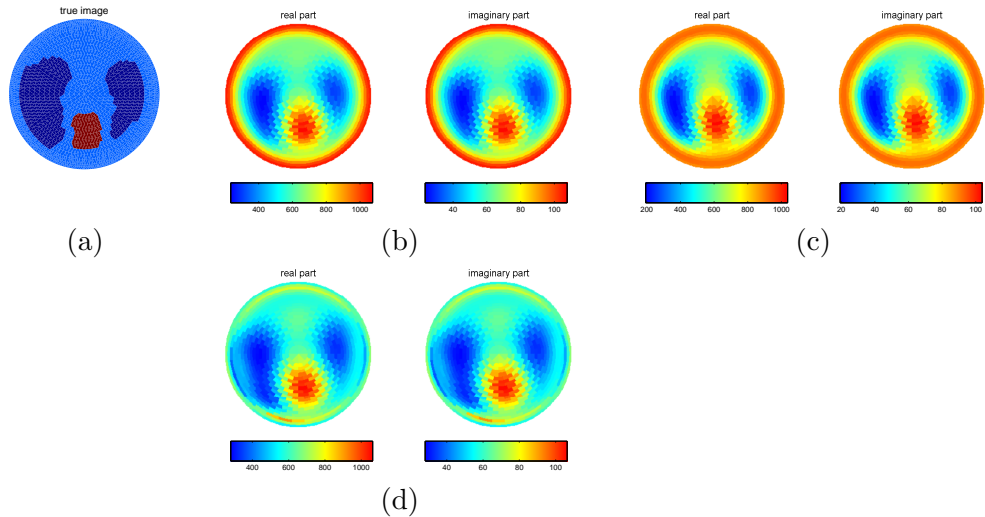


Figure 4.3: Static images with different mathematical models which are reconstructed by the linearization method using FEM simulation data: (a) true image, (b) gap model, (c) ave-gap model and (d) complete electrode model. The range of conductivity and permittivity values is given in  $mS/m$ .

CE model has smaller error than other models. The gap model has bigger error than the ave-gap model since the gap model has values of the potential at the center of each electrode, whereas the ave-gap model has average values of the potential on each electrode.

Figure 4.3 shows static images with different mathematical models which are reconstructed by the linearization method using FEM simulation data. The simulation phantom which is a simplified geometry of the human chest is shown in Figure 4.3(a). Figures 4.3(b), 4.3(c) and 4.3(d) are the reconstructed images obtained by using the gap model, ave-gap model and CE model, respectively. The reconstructed images of the gap model and the ave-gap model have ring effect which is the high admittivity region at the boundary of the phantom. Reason is that both models don't consider the shunting effect of the electrodes as well as the surface impedances in the forward solver. On the other hand, the reconstructed image of the CE model does not have this ring effect and hence the images of the lungs are closer to the true lungs than other

models because this model takes into account both the shunting effect and the surface impedances.

#### 4.2.1.2 Chest phantom experimental data

To obtain the measured voltages on the electrodes, we used a chest phantom and obtained complex voltages from the ACT3 system. It is worth mentioning here, that for acquiring complex voltages, the ACT3 system has an intrinsic limitation, even though not severe, that sometimes it does not converge to the accurate imaginary values for voltage measurements.

The geometry of the chest phantom used was as follows: radius 15 *cm*, width of the electrode 2.54 *cm*, saline level 2.3 *cm*, and the amplitude of the currents 0.5 *mA*. The admittivity of the saline solution was  $640 + i0 \text{ mS/m}$  ( $154.7 - i0 \text{ } \Omega\text{cm}$ ), the agar lungs  $400 + i0 \text{ mS/m}$  ( $250 - i0 \text{ } \Omega\text{cm}$ ), and agar heart  $1512 + i0 \text{ mS/m}$  ( $66.14 - i0 \text{ } \Omega\text{cm}$ ). Here, the agar does not give a permittivity value in the admittivity.

Figure 4.4 shows static images with different mathematical models which are reconstructed by the linearization method using chest phantom experimental data. The chest phantom used as a simplified geometry of the human chest is shown in Figure 4.4(a), which has different sizes of the lungs and the heart. Figures 4.4(b), 4.4(c) and 4.4(d) are the reconstructed images obtained by using the gap model, ave-gap model and CE model, respectively. The results obtained by using experimental data are similar to those that were obtained by using the simulation data.

It should be noted that in the static imaging, the gap model and the ave-gap model are visually similar as seen in Figure 4.4. However, the ave-gap model usually has lower RMS errors as compared to the gap model as shown in Figure 4.2. So, in a way the ave-gap model is better than the gap model. As mentioned before, the CE model does not have the ring effect that the gap model and the ave-gap model have. In the CE model, we set



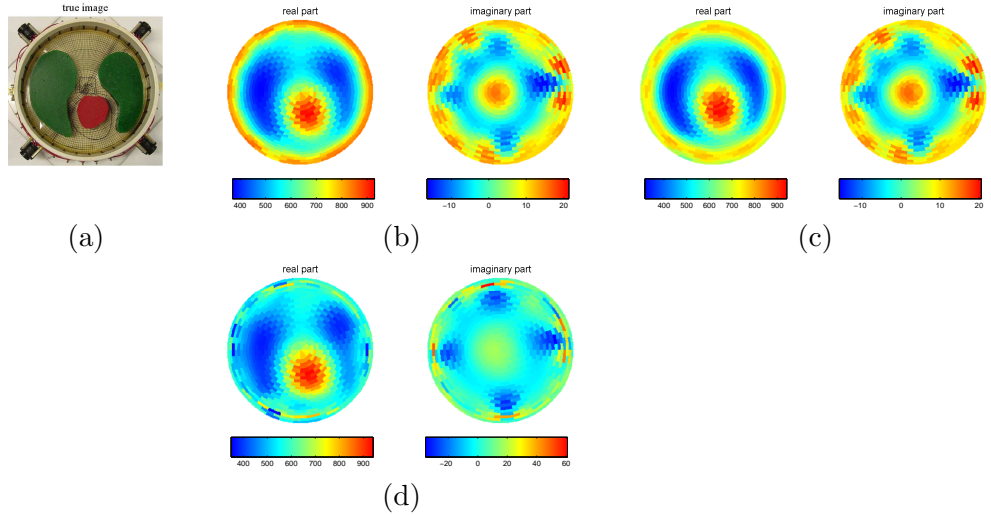


Figure 4.4: Static images with different mathematical models which are reconstructed by the linearization method using experimental data: (a) true image, (b) gap model, (c) ave-gap model and (d) complete electrode model. The range of conductivity and permittivity values is given in  $mS/m$ .

all the electrodes to have the same surface impedances as initial values which are only real. This causes misleading values at positions near the electrodes, especially in the imaginary part. Also, the dynamic range of the imaginary part increases because all the electrodes have different surface impedances in practice. If we were to find appropriate values of the surface impedances in the chest phantom, the CE model is expected to produce a better resolution of the reconstructed images.

#### 4.2.1.3 Comparison between the linearization method and the fast inversion algorithm

In this subsection, we compare the performances of the linearization method with the fast inversion algorithm with the goal of reducing the computational time.

Figure 4.5 shows the difference of the estimated admittivity distribu-

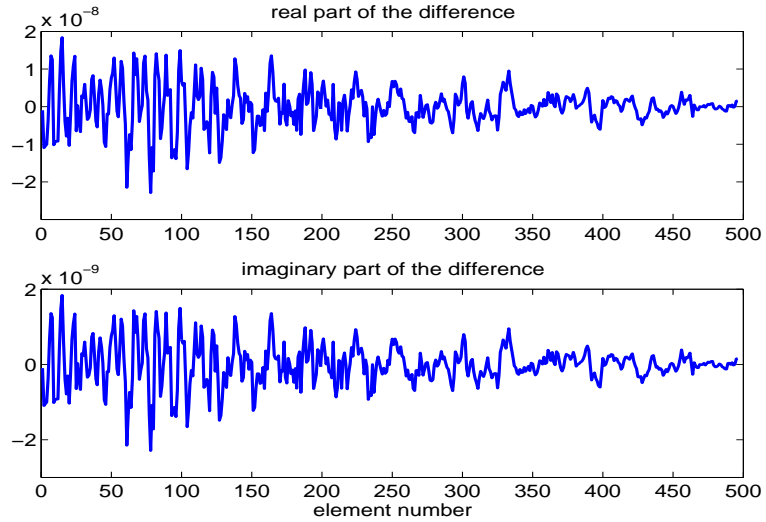


Figure 4.5: The difference of the estimated admittivity distributions between the linearization method and fast inversion algorithm.

tions between the linearization method and fast inversion algorithm in the 32-electrode chest phantom. As can be expected, both algorithms produce the same results. Mathematically the two algorithms are the same.

To compare the computational time of both algorithms, we only consider the elapsed time for computing (3.32) and (3.41). Table 4.2 shows the elapsed time of the linearization method and fast inversion algorithm in the 32- and 64-electrode EIT system. It can be seen clearly that the fast inversion algorithm using a spectral representation produces the same results as obtained by the linearization method. However, it has a reduced computational burden.

Table 4.2: Elapsed time of the linearization method and fast inversion algorithm in the 32- and 64-electrode EIT system (computer used: Pentium(R) 4 CPU 2.66GHz, 512MB RAM, Windows XP, MATLAB R13).

	Linearization Method	Fast Inversion Algorithm
32-electrode system	0.5 sec	0.343 sec
64-electrode system	31.203 sec	23.735 sec

#### 4.2.1.4 Discussion

For the static image reconstruction the linearization method was used to illustrate the reconstruction performances of different mathematical models using FEM simulation data and experimental data.

We also discussed the ring effect in reconstructed images for different models and recommended the CE model as the most appropriate model based on the simulation and experimental results. We also compared the linearization method against the fast inversion algorithm in view of the computation burden and showed that the fast inversion algorithm using a spectral representation produced the same results as the one obtained by the linearization method but with the advantage of having reduced computational burden.

#### 4.2.2 Dynamic imaging reconstruction

In the design of the LKF algorithm, it was assumed that the covariance matrices are diagonal and time-invariant; the covariance matrices of process and measurement noises were  $\Gamma_k^w = 10^{-6}I_L$ ,  $\Gamma_k = 10^{-4}I_L$ , respectively, and initial value of the error covariance matrix was  $C_{0|0} = I_{N_s}$  for computing the Kalman gain matrix off-line. It was possible to use the LKF algorithm without the regularization parameter in the analytical method, while the regularization parameter was set to 0.1 only for the NOSER algorithm. The range of resistivity and capacitive reactivity values in  $\Omega\text{-cm}$  is given in the scale beneath each set of images.

We considered dynamically changing scenarios, that is, it was assumed that the size of the heart was changing within the data acquisition time (one classical frame), but the admittivities of the different sizes (big and small) of the heart were kept the same, and the volume and the admittivity of the lungs were fixed. It represents the scenario when the person holds his/her breath during the acquisition of measurement data. For the simulation data we computed voltages with the FEM and for the experimental data we obtained

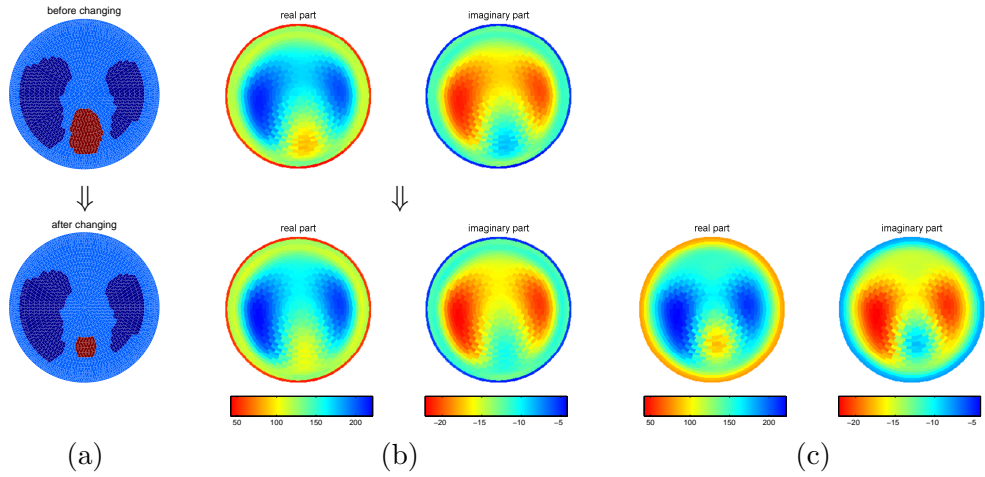


Figure 4.6: Reconstructed images: (a) true change of the heart size, (b) images by LKF with all current patterns and (c) image by NOSER with all current patterns. The range of resistivity and capacitive reactivity values is given in  $\Omega\text{-cm}$ .

voltages with a chest phantom in a simplified geometry of the human chest.

#### 4.2.2.1 FEM simulation data

The geometry of the simulation phantom used was as follows: radius 15  $cm$ , width of the electrode 2.54  $cm$ , height 1  $cm$ , and the amplitude of the currents 0.5  $mA$ . The admittivity (impedivity) of the background was  $640 + i64 mS/m$  ( $154.7 - i15.47 \Omega cm$ ), the lungs  $400 + i40 mS/m$  ( $247.5 - i24.75 \Omega cm$ ), and the heart  $1500 + i150 mS/m$  ( $66.0 - i6.60 \Omega cm$ ).

We used the following scenario: The big heart was used when the first 16 current patterns were injected and then the size was rapidly changed, and the small heart was used for the next 15 current patterns.

The simulation phantom with different sizes of the heart is shown in Figure 4.6(a) as true images. Figures 4.6(b) and 4.6(c) are images reconstructed by the LKF and NOSER algorithm, respectively when all current patterns in (4.1) are sequentially injected to the body. In Figure 4.6, it can be seen that the LKF algorithm gives the temporal resolution when the size of the heart

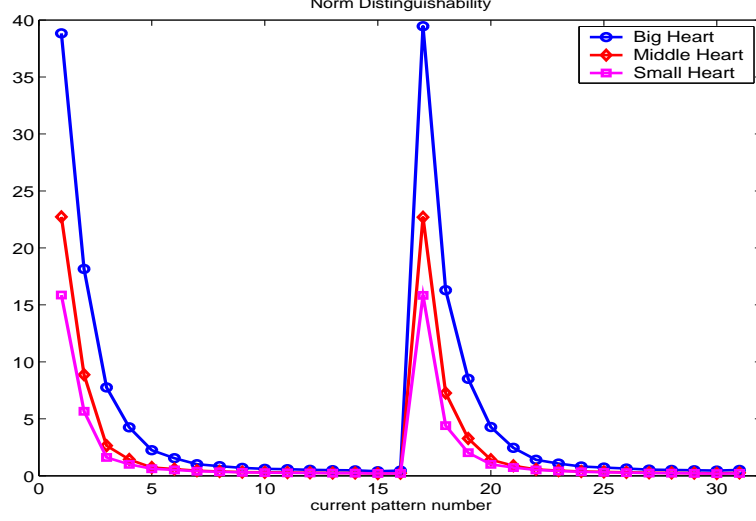


Figure 4.7: Norm distinguishability for the each heart according to the current pattern.

changes, while the NOSER algorithm fails to do so and shows that there is no change.

We define distinguishability as a measurement of the ability to differentiate between the homogeneous and inhomogeneous admittivities inside the body (Isaacson 1986). As the spatial frequency in (4.1) increases, it gives lower norm distinguishability in Figure 4.7. The norm distinguishability in the mean square sense, was defined by (Cheney and Isaacson 1992, Isaacson 1986)

$$\delta_I(\zeta, \zeta_0, j_k) \equiv \sqrt{\frac{\sum_{\ell=1}^L |V_{\ell,k}(\zeta, j_k) - V_{\ell,k}(\zeta_0, j_k)|^2}{\sum_{\ell=1}^L |I_{\ell,k}|^2}} \quad (4.3)$$

where  $V_{\ell,k}(\zeta, j_k)$  denotes the  $k$ -th measured voltage in the inhomogeneous phantom with a target, and  $V_{\ell,k}(\zeta_0, j_k)$  denotes the  $k$ -th measured voltage when current density  $j_k$  is applied in the homogeneous phantom with no target. In Figure 4.7, when we only use the different sizes of the heart in the chest phantom, it shows the norm distinguishability for each heart according to the current pattern in (4.1). The low spatial frequencies for trigonometric current

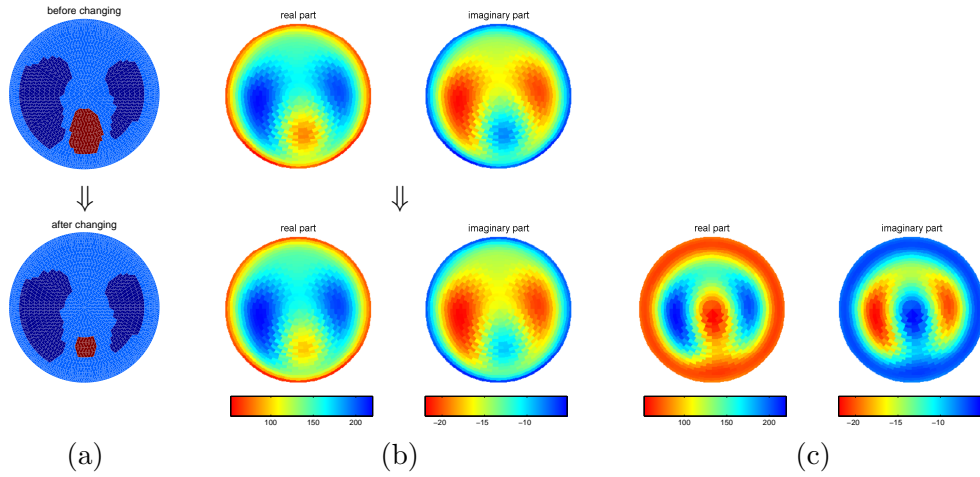


Figure 4.8: Reconstructed images: (a) true change of the heart size, (b) images by LKF with 8 current patterns and (c) image by NOSER with 8 current patterns. The range of resistivity and capacitive reactivity values is given in  $\Omega\text{-cm}$ .

patterns contain more information about the chest phantom and can be seen with high distinguishability between current patterns 1 and 4 and between current patterns 16 and 19 in Figure 4.7. Therefore, it is advisable that the low spatial frequencies in trigonometric current patterns should be used.

Figures 4.8(b) and 4.8(c) are images reconstructed by the LKF and NOSER algorithm, respectively when only 8 current patterns, that is,  $\cos(\theta), \dots, \cos(4\theta), \sin(\theta), \dots, \sin(4\theta)$  in (4.1) are repeatedly applied to the body. As can be expected, the LKF algorithm gives the spatial and temporal resolution on changing the size of the heart, while the reconstructed images obtained from the NOSER algorithm are blurred and the temporal information on the time-variability of the heart is lost.

The LKF and NOSER algorithm of elapsed time for estimating the impedance distribution are 62 *m*-sec and 218 *m*-sec (computer used: Pentium(R) 4 CPU 2.66GHz, 512MB RAM, Windows XP, MATLAB R13), respectively in one classical frame. The LKF algorithm produces 31 images, while the NOSER algorithm produces 1 image in one classical frame.

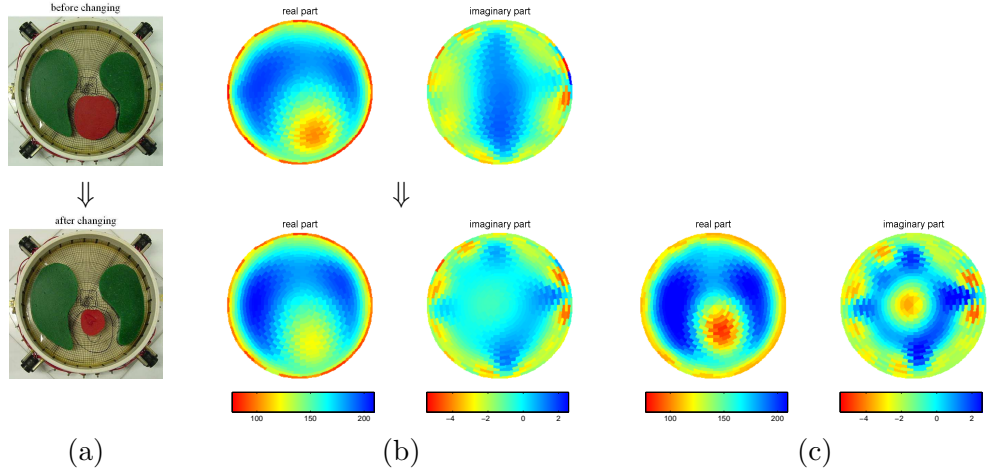


Figure 4.9: Reconstructed images: (a) true change of the heart size, (b) images by LKF with all current patterns and (c) image by NOSER with all current patterns. The range of resistivity and capacitive reactivity values is given in  $\Omega\text{-cm}$ .

#### 4.2.2.2 Chest phantom experimental data

The geometry of the chest phantom used was as follows: radius  $15\text{ cm}$ , width of the electrode  $2.54\text{ cm}$ , saline level  $2.3\text{ cm}$ , and the amplitude of the currents  $0.5\text{ mA}$ . The admittivity of the saline solution was  $640 + i0\text{ mS/m}$  ( $154.7 - i0\ \Omega\text{cm}$ ), the agar lungs  $400 + i0\text{ mS/m}$  ( $250 - i0\ \Omega\text{cm}$ ), and agar heart  $1512 + i0\text{ mS/m}$  ( $66.14 - i0\ \Omega\text{cm}$ ).

In the experiment, the scenario used is as follows: The big heart (length:  $10\text{ cm}$ , width:  $9.4\text{ cm}$ ) was used while the current patterns 1 to 16 were injected and then the size was rapidly changed, and the small heart (length:  $6.1\text{ cm}$ , width:  $5.5\text{ cm}$ ) was used while the current patterns 17 to 31 were applied to the chest phantom.

The chest phantom with different sizes of the heart is shown in Figure 4.9(a) as true images. Figures 4.9(b) and 4.9(c) are images reconstructed by the LKF and NOSER algorithm, respectively when all current patterns in (4.1) are sequentially injected to the chest phantom. Similar to the simulation results mentioned before, the LKF algorithm gives the temporal resolution

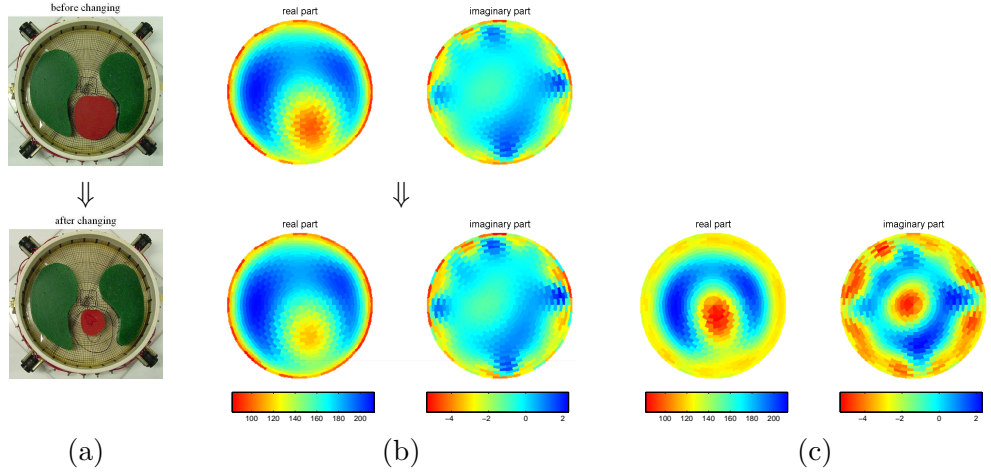


Figure 4.10: Reconstructed images: (a) true change of the heart size, (b) images by LKF with 8 current patterns and (c) image by NOSER with 8 current patterns. The range of resistivity and capacitive reactivity values is given in  $\Omega\text{-cm}$ .

when the size of the heart changes, whereas the NOSER algorithm fails to provide any information on temporal changes.

Figures 4.10(b) and 4.10(c) are images reconstructed by the LKF and NOSER algorithm, respectively when only 8 current patterns, that is,  $\cos(\theta), \dots, \cos(4\theta), \sin(\theta), \dots, \sin(4\theta)$  in (4.1) are repeatedly applied to the chest phantom. Here it is also shown that the LKF algorithm outperforms NOSER algorithm.

#### 4.2.2.3 Discussion

Simulation and phantom experiment were conducted to illustrate the reconstruction performance in the sense of spatio-temporal resolution. In this study, we considered dynamically changing scenarios, that is, it was assumed that the size of the heart was changing within the data acquisition time (one classical frame), but the admittivities of the different sizes (big and small) of the heart were kept the same, and the volume and the admittivity of the lungs were fixed. It represents the scenario when the person holds his/her



breath during the acquisition of measurement data. For the simulation data we computed voltages with the FEM and for the experimental data we obtained voltages with a chest phantom in a simplified geometry of the human chest.

The static imaging technique failed to obtain satisfactory temporal resolution for the reconstructed images when rapid changes in the impedivity distribution happen within the data acquisition time. But the dynamic imaging technique can provide an estimate of the impedivity distribution after each current pattern was applied to the body. Hence, the temporal resolution can be enhanced with the aid of the linearized Kalman filter.

### 4.3 3-D Mammography Geometry

In this section, we evaluated the 3-D reconstruction performances of the proposed algorithms using experimental data at 10 kHz, which were collected from a saline-filled phantom using the 64-electrode ACT4 instrument.

#### 4.3.1 3-D test phantom and voxel configuration

The 64-electrode test phantom for the 3-D mammography geometry is shown in Figure 4.11. It was made of plexiglas and its inner shape was designed to resemble the shape of the human breast. The planar electrode arrays are located on the front and back side walls, which correspond to the top and bottom electrode arrays of the mammography geometry model in Figure 2.3(b). Each electrode array has 36 electrodes coated with silver on a printed circuit board (PCB) and the gaps between adjacent electrodes are filled with epoxy. Four electrodes (the dotted squares in Figure 4.12(a)) on it are disconnected in the experimental study for the 64-electrode test phantom. In the electrode array, the size of each electrode is  $10 \times 10 \text{ mm}$  ( $l_x = l_y = 0.01$ ), the length of the gap between adjacent electrodes is  $1 \text{ mm}$  ( $\delta x = \delta y = 0.001$ ) and the length of the gap near the boundary is  $2 \text{ mm}$  ( $\delta x_2 = \delta y_2 = 0.002$ ). The

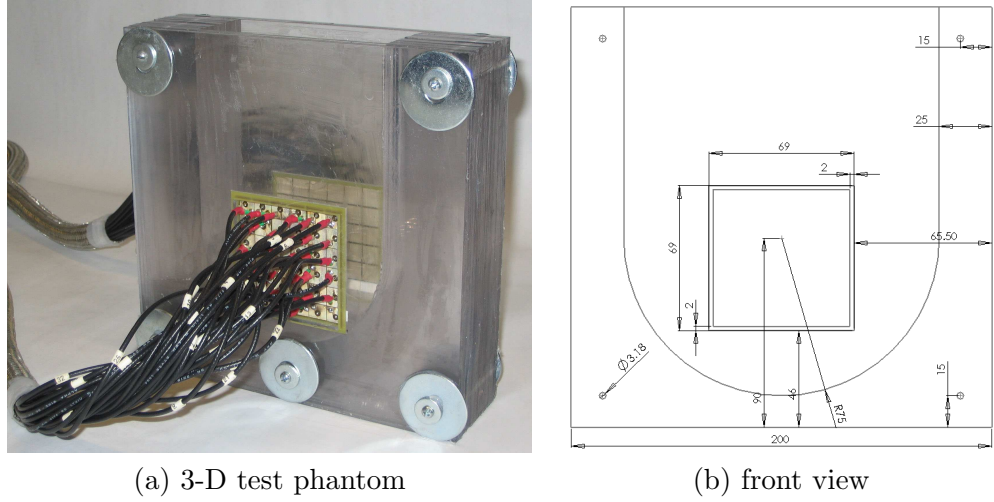


Figure 4.11: The 64-electrode test phantom for the 3-D mammography geometry used in the experiment.

dimension of the mammography geometry model is  $69(h_1) \times 69(h_2) \times 40(h_3)$  mm.

In order to describe the admittivity distribution inside the body, the 3-D domain is approximated by a sufficiently large set of  $N_s$  voxels, and the characteristic function  $\chi_s(p)$  is chosen over the  $s$ -th voxel. It is assumed that the admittivity is constant within each voxel. The voxel configuration is limited by the number of independent measurements and the size depth of the smallest detectable object in the body. The voxel configuration consists of 8 layers with  $16 \times 16$  voxels in each layer and the dimension of each voxel is  $5.44 \times 5.44 \times 5$  mm. The configuration must model the unbounded domain in a practical manner. This feature is modeled by including more voxels around the boundary of the electrode array. The configuration is depicted in Figure 4.12.

### 4.3.2 Image reconstruction

In order to conduct the experiments, a test phantom in Figure 4.11(a) was filled with a conductivity  $300 \text{ mS/m}$  of the saline solution to a depth of

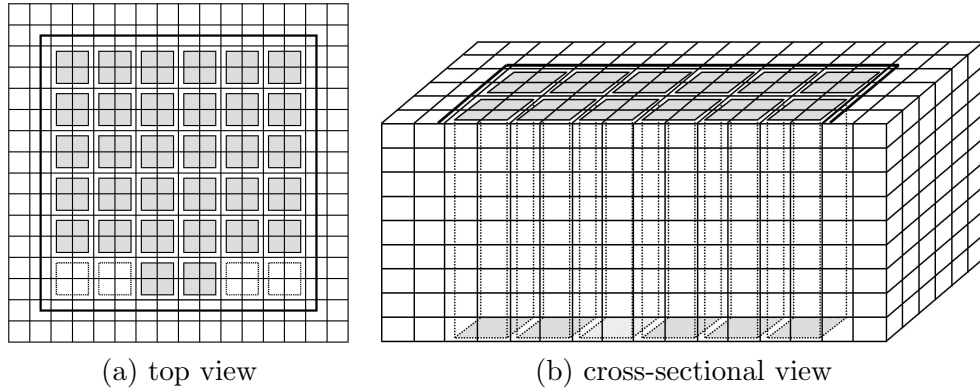


Figure 4.12: Voxel configuration used in the inverse problem. The bold lines represent the edges of the electrode array, the shaded squares represent the electrodes and the dotted squares denotes the disconnected electrodes in the left figure.

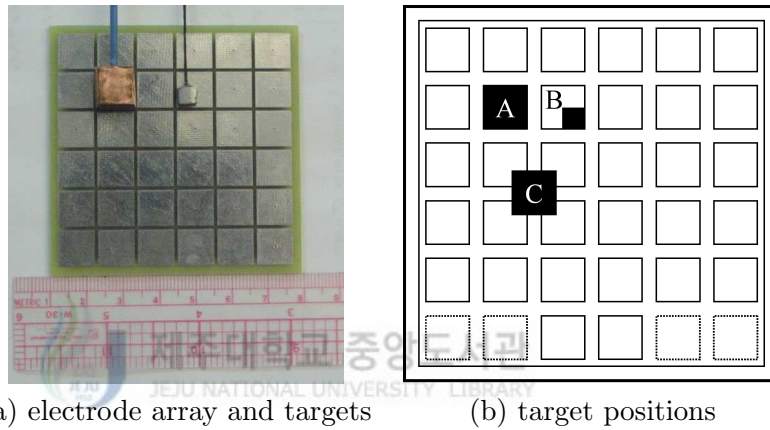


Figure 4.13: The conductor targets (shaded rectangles) are placed 5 mm distant from the electrode array in three positions. Position A: 10 mm copper target beneath the electrode, position B: 5 mm solder target beneath the electrode, position C: 10 mm copper target beneath the gap between the four adjacent electrodes.

10 cm. This conductivity was chosen to approximate that of healthy breast tissue. Targets used in this experiment are as follows:  $4 \times 5 \times 4.5$  mm target made of solder,  $10 \times 10 \times 10$  mm target made of plexiglas covered with a thin oxidized copper foil. Each target was suspended in the phantom at several spatial positions using a thin insulated rod (Figure 4.13(a)).

We displayed the reconstructed admittivity distribution as static images and also plotted difference images, which were obtained by subtracting the reconstructed admittivity distribution of the homogeneous case from that of the inhomogeneous case. Since we only seek to reconstruct the admittivity distribution accurately in the region directly below the electrode array, only those voxels are included in the image. Since each electrode array has four electrodes disconnected, those electrodes are not displayed in the images. Each reconstructed image is displayed in grey-scale.

To study the spatial resolution in the  $x$ - $y$  plane of the electrodes, a 5 mm solder target and a 10 mm copper target were placed at a distance of 5 mm from the face of the electrode in position A and position B, respectively, and a 10 mm copper target was placed at a distance of 5 mm from the gap between the four adjacent electrodes in position C in Figure 4.13(b). To study the spatial resolution in the  $z$ -axis, a 10 mm copper target was positioned 7.5 mm, 10 mm, 12.5 mm and 15 mm distant from the face of the electrode in position A. Note that since the 3-D test phantom is symmetrical, it is sufficient to test the target locations in one half the phantom depth ( $z$ -axis), that is, from layer 1 to layer 4.



#### 4.3.2.1 Distinguishability

For the distinguishability study in the 3-D mammography geometry using the complex data obtained from the ACT4 system, the norm distinguishability (4.3) needs to be replaced as follows:

$$\delta_T(\zeta, \zeta_0, j_k) \equiv \sqrt{\frac{\sum_{\ell=1}^L |W_{\ell,k}(\zeta, j_k) - W_{\ell,k}(\zeta_0, j_k)|^2}{\sum_{\ell=1}^L |T_{\ell,k}|^2}} \quad (4.4)$$

where  $W_{\ell,k}(\zeta, j_k)$  denotes the  $k$ -th synthesized voltage in the inhomogeneous phantom with a target, and  $W_{\ell,k}(\zeta_0, j_k)$  denotes the  $k$ -th synthesized voltage in the homogeneous phantom with no target.  $T_{\ell,k}$  represents the normalized

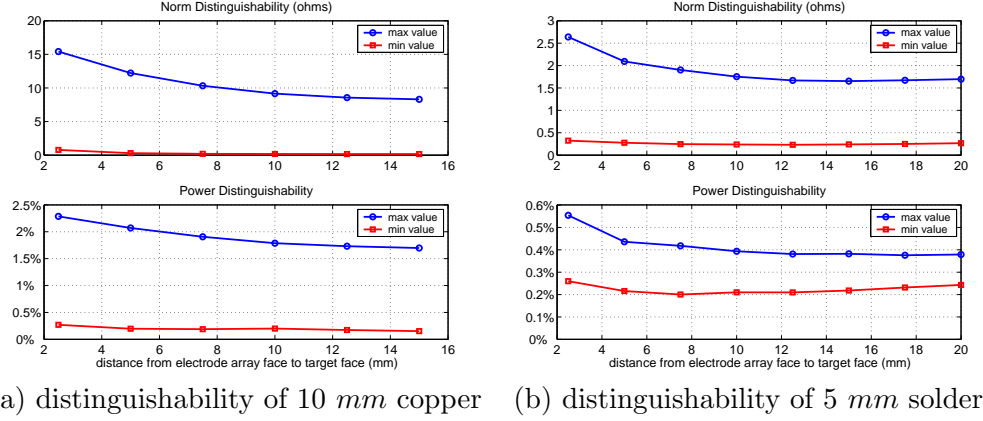


Figure 4.14: The norm and power distinguishabilities according to the different depth between the electrode array face and the target face in the 3-D mammography geometry using the complex data obtained from the ACT4 system.

$k$ -th canonical current pattern.

Power distinguishability is defined as the measured power change between the homogeneous and inhomogeneous cases, divided by the power applied in the homogeneous case (Cheney and Isaacson 1992, Kao *et al.* 2003),

$$\delta_P(\zeta, \zeta_0, j_k) \equiv \frac{|P_k(\zeta, j_k) - P_k(\zeta_0, j_k)|}{|P_k(\zeta_0, j_k)|} \quad (4.5)$$

where the  $k$ -th power  $P_k \equiv \sum_{\ell=1}^L T_k W_k$ .

Figure 4.14 shows the norm and power distinguishabilities according to different depths between the electrode array face and the target face in the 3-D mammography geometry using the complex data obtained from the ACT4 system. Figure 4.14(a) shows the distinguishability of the 10 mm copper and Figure 4.14(b) shows the distinguishability of the 5 mm solder in one half the phantom depth ( $z$ -axis) since the 3-D test phantom is symmetrical. Distinguishability decreases as the target moves away from the top electrode array and reaches its lowest value when target is at the middle position between the two electrode arrays. Furthermore, these experimental data were obtained

during the last phase of the ACT4 system development, so they may contain some level of error due to the imprecise calibration. Hence, in Figure 4.14(b), the power distinguishability reaches closer to the noise level, which means that this target may not be detected. Therefore, to study the spatial resolution in the  $z$ -axis, we use the 10  $mm$  copper target.

#### 4.3.2.2 Fast inversion algorithm reconstruction

In the design of the fast inversion algorithm, we set the regularization parameters ( $\alpha$ ) to be 0.7 and 0.02 for the static images and difference images, respectively. The conductivity and permittivity distributions were simultaneously estimated and reconstructed using the fast inversion algorithm. The images reconstructed from the experimental data with the 10  $mm$  and 5  $mm$  targets in 3 positions are displayed in Figure 4.15 ~ 4.17. Within each layer, each square denotes the conductivity or permittivity in the corresponding voxel. The range of conductivity or permittivity values in  $mS/m$  is given in the scale beneath each set of images.

Figure 4.15(a) and (b) are the reconstructed static images of 10  $mm$  copper target which was placed at a distance of 5  $mm$  from the face of the electrode in position A, and Figure 4.15(c) and (d) are the reconstructed difference images. In the reconstructed static images, the inhomogeneity in position A was estimated, but the static images were sharper than the difference images. This is due to the discrepancy between the simplified forward model and the test phantom, and not considering the shunting effect and surface impedances of the electrodes in the forward modeling. These data may contain some level of error due to the imprecise calibration of the ACT4 instrument. The data presented were obtained during the last phase of the instrument development, and the final calibration had not been performed when it was necessary to present these results. This also causes the faint or blurred images in the imaginary part (permittivity) of the admittivities. Figure 4.16 shows

the reconstructed difference images of 5 mm solder target which was placed at a distance of 5 mm from the face of the electrode in position B. Figure 4.17 shows the reconstructed difference images of 10 mm copper target which was placed at a distance of 5 mm from the gap between the four adjacent electrodes in position C. The inhomogeneity's positions in the difference images were well characterized by the reconstruction from experimental data. The reconstructed images are better when the inhomogeneities are directly beneath the electrodes. In the reconstructions, the image became fainter, but was still less pronounced in the lower and/or upper voxel layers. It is conjectured that this phenomenon is due in part to the smoothing effect of the regularization.

Figure 4.18 shows the difference images reconstructed from the experimental data with the 10 mm copper target at the different depths in the  $z$ -axis. As can be expected, when the copper target was moved at a distance of 7.5 mm from the face of the electrode in position A, it became more prominent in the third layer and less prominent in the second and fourth layers. When the copper target was moved at a distance of 10 mm, it became more prominent in the third and fourth layers. When the copper target was moved at a distance of 12.5 mm, it became more prominent in the fourth layer and less prominent in the third and fifth layers. And also when the copper target was moved at a distance of 15 mm, it became more prominent in the fourth and fifth layers.

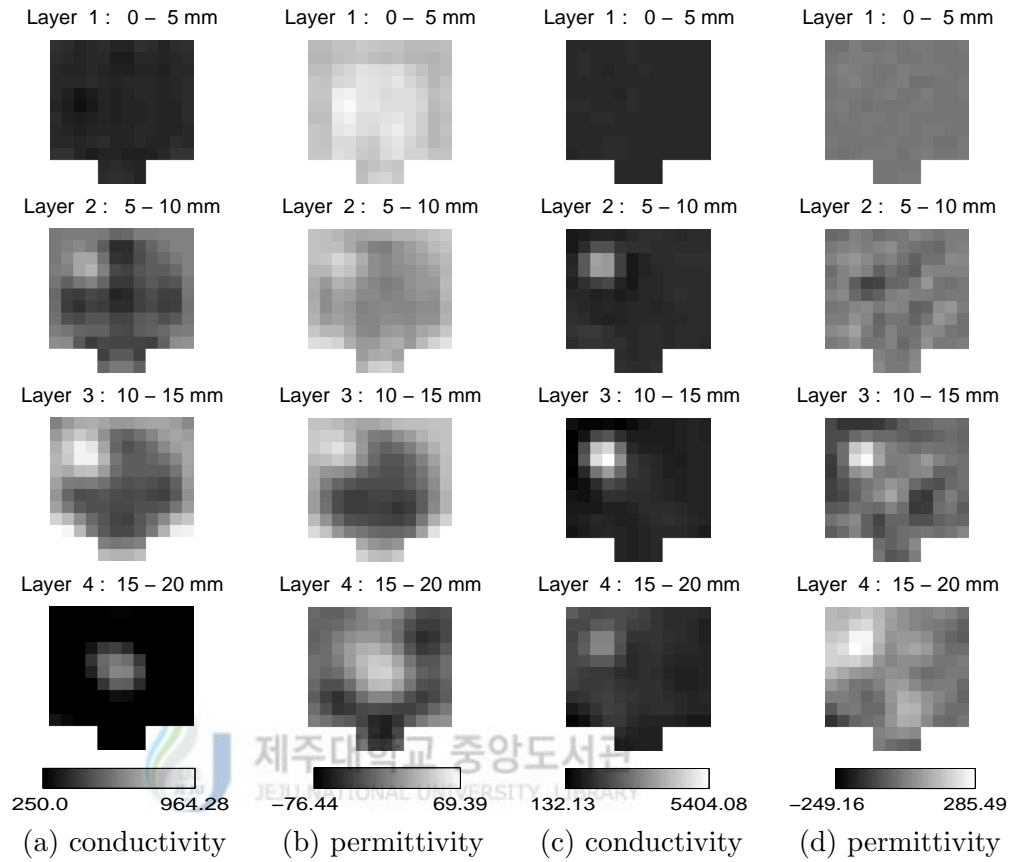


Figure 4.15: Reconstructed images of the 10 mm copper target. The copper target was placed 5 mm distant from the face of the electrode in position A. The range of conductivity and permittivity values is given in  $mS/m$ . (a) real part of the estimated admittivities in the static images, (b) imaginary part of the estimated admittivities in the static images, (c) real part of the estimated admittivities in the difference images and (d) imaginary part of the estimated admittivities in the difference images.



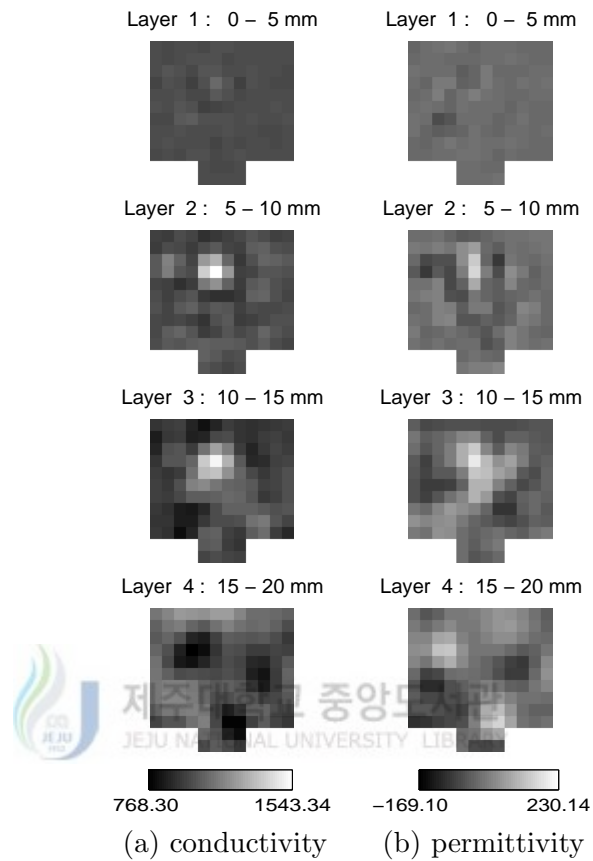


Figure 4.16: Reconstructed difference images of the 5 mm solder target. The solder target was placed 5 mm distant from the electrode in position B. The range of conductivity and permittivity values is given in  $mS/m$ . (a) real part of the estimated admittivities and (b) imaginary part of the estimated admittivities.

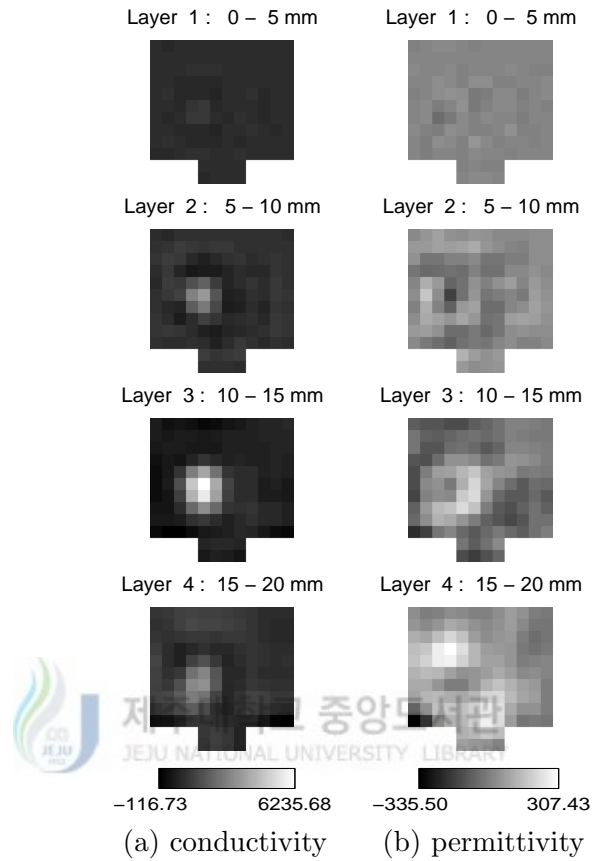


Figure 4.17: Reconstructed difference images of the 10 mm copper target. The copper target was placed 5 mm distant from the gap between the four adjacent electrodes in position C. The range of conductivity and permittivity values is given in  $mS/m$ . (a) real part of the estimated admittivities and (b) imaginary part of the estimated admittivities.



(a) depth 7.5 mm (b) depth 10 mm (c) depth 12.5 mm (d) depth 15 mm

Figure 4.18: Reconstructed difference images of the 10 mm copper target according to the different depths in the  $z$ -axis. The copper target was positioned 7.5 mm, 10 mm, 12.5 mm and 15 mm distant from the face of the electrode in position A. The range of conductivity values is given in  $mS/m$ .

### 4.3.2.3 NOSER algorithm reconstruction

In the design of the NOSER algorithm, we set the regularization parameters ( $\alpha$ ) to be 0.07 for the difference images. The resistivity and capacitive reactivity distributions were simultaneously estimated and reconstructed using the NOSER algorithm. The images reconstructed from the experimental data with the 10 mm and 5 mm targets in 3 positions are displayed in Figure 4.19 ~ 4.21. Within each layer, each square denotes the resistivity or capacitive reactivity in the corresponding voxel. The range of resistivity and capacitive reactivity values in  $\Omega\text{-cm}$  is given in the scale beneath each set of images.

Figure 4.19 shows the reconstructed difference images of 10 mm copper target which was placed at a distance of 5 mm from the face of the electrode in position A. Figure 4.20 shows the reconstructed difference images of 5 mm solder target which was placed at a distance of 5 mm from the face of the electrode in position B. Figure 4.21 shows the reconstructed difference images of 10 mm copper target which was placed at a distance of 5 mm from the gap between the four adjacent electrodes in position C. The inhomogeneity's positions in the difference images were well characterized by the reconstruction from experimental data. The reconstructed images are better when the inhomogeneities are directly beneath the electrodes.

Figure 4.22 shows the difference images reconstructed from the experimental data with the 10 mm copper target at the different depths in the  $z$ -axis. As can be expected, when the copper target was moved at a distance of 7.5 mm from the face of the electrode in position A, it became more prominent in the third layer and less prominent in the second and fourth layers. When the copper target was moved at a distance of 10 mm, it became more prominent in the third and fourth layers. When the copper target was moved at a distance of 12.5 mm, it became more prominent in the fourth layer and less prominent in the third and fifth layers. And when the copper target was moved at a distance of 15 mm, it became more prominent in the fourth and fifth layers. In the reconstructions, the image became faint, but was still less

prominent in the lower and/or upper voxel layers.

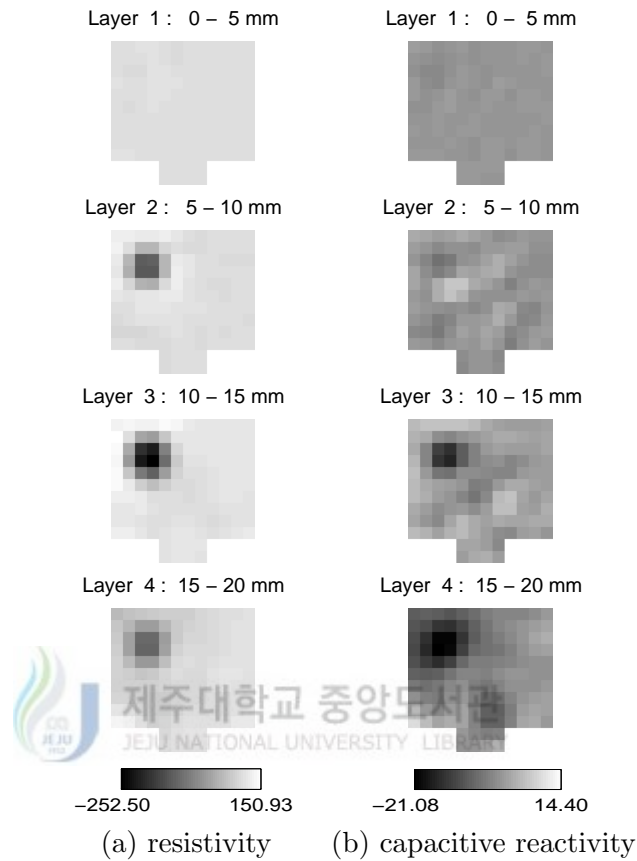


Figure 4.19: Reconstructed difference images of the 10 *mm* copper target. The copper target was placed 5 *mm* distant from the face of the electrode in position A. The range of resistivity and capacitive reactivity values is given in  $\Omega\text{-cm}$ . (a) real part of the estimated impedivities and (b) imaginary part of the estimated impedivities.

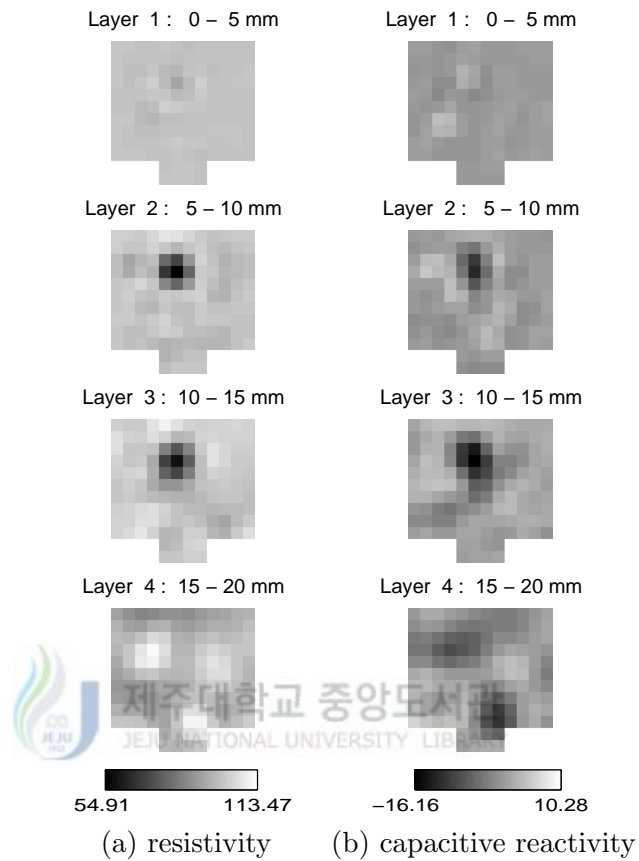


Figure 4.20: Reconstructed difference images of the 5 mm solder target. The solder target was placed 5 mm distant from the electrode in position B. The range of resistivity and capacitive reactivity values is given in  $\Omega\text{-cm}$ . (a) real part of the estimated impedivities and (b) imaginary part of the estimated impedivities.

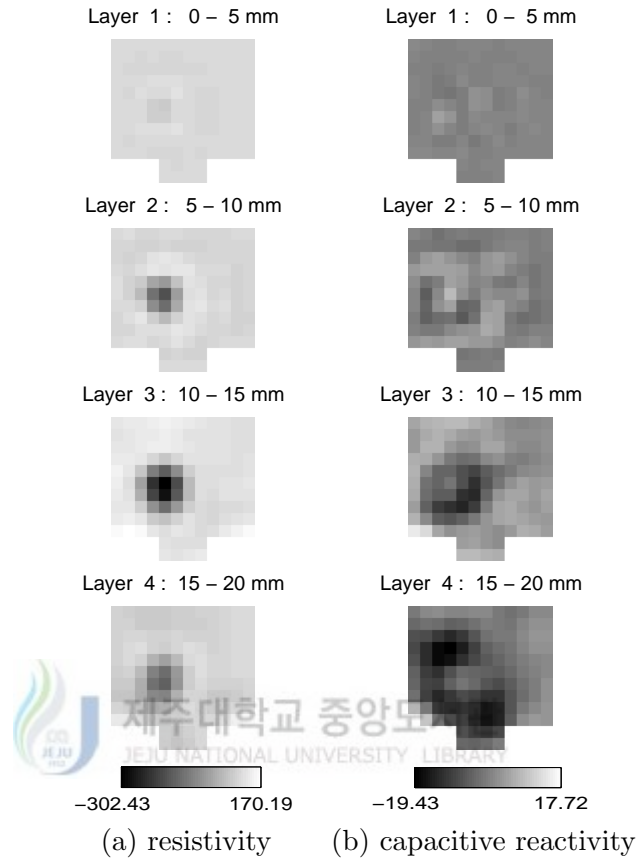


Figure 4.21: Reconstructed difference images of the 10 mm copper target. The copper target was placed 5 mm distant from the gap between the four adjacent electrodes in position C. The range of resistivity and capacitive reactivity values is given in  $\Omega\text{-cm}$ . (a) real part of the estimated impedivities and (b) imaginary part of the estimated impedivities.



(a) depth 7.5 mm (b) depth 10 mm (c) depth 12.5 mm (d) depth 15 mm

Figure 4.22: Reconstructed difference images of the 10 mm copper target according to the different depths in the  $z$ -axis. The copper target was positioned 7.5 mm, 10 mm, 12.5 mm and 15 mm distant from the face of the electrode in position A. The range of resistivity values is given in  $\Omega\text{-cm}$ .



#### 4.3.2.4 Linearized Kalman filter (LKF) reconstruction

In the design of the LKF algorithm, it was assumed that the covariance matrices are diagonal; the covariance matrices of process and measurement noises were  $\Gamma_k^w = 10^{-6}I_L$ ,  $\Gamma_k = 5 \times 10^{-2}I_L$ , respectively, and initial value of the error covariance matrix was  $C_{0|0} = I_{N_s}$  for computing the Kalman gain matrix off-line. It was available to perform the LKF algorithm without the regularization parameter in the analytical method.

The resistivity and capacitive reactivity distributions were simultaneously estimated and reconstructed using the LKF algorithm. The images reconstructed from the experimental data with the 10 mm and 5 mm targets in 3 positions are displayed in Figure 4.23 ~ 4.25. Within each layer, each square denotes the resistivity or capacitive reactivity in the corresponding voxel. The range of resistivity and capacitive reactivity values in  $\Omega\text{-cm}$  is given in the scale beneath each set of images.

Figure 4.23 shows the reconstructed difference images of 10 mm copper target which was placed at a distance of 5 mm from the face of the electrode in position A. Figure 4.24 shows the reconstructed difference images of 5 mm solder target which was placed at a distance of 5 mm from the face of the electrode in position B. Figure 4.25 shows the reconstructed difference images of 10 mm copper target which was placed at a distance of 5 mm from the gap between the four adjacent electrodes in position C. The inhomogeneity's positions in the difference images were well characterized by the reconstruction from experimental data. The reconstructed images are better when the inhomogeneities are directly beneath the electrodes.

Figure 4.26 shows the difference images reconstructed from the experimental data with the 10 mm copper target at the different depths in the  $z$ -axis. As can be expected, when the copper target was moved at a distance of 7.5 mm from the face of the electrode in position A, it became more prominent in the third layer and less prominent in the second and fourth layers. When the copper target was moved at a distance of 10 mm, it became more

prominent in the third and fourth layers. When the copper target was moved at a distance of 12.5 *mm*, it became more prominent in the fourth layer and less prominent in the third and fifth layers. And when the copper target was moved at a distance of 15 *mm*, it became more prominent in the fourth and fifth layers. In the reconstructions, the image became faint, but was still less prominent in the lower and/or upper voxel layers.



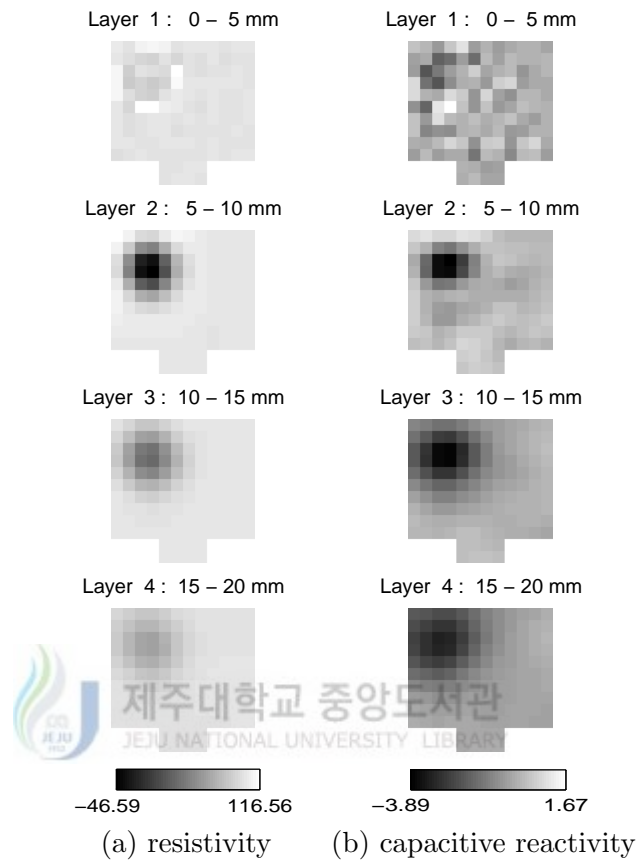


Figure 4.23: Reconstructed difference images of the 10 mm copper target. The copper target was placed 5 mm distant from the face of the electrode in position A. The range of resistivity and capacitive reactivity values is given in  $\Omega\text{-cm}$ . (a) real part of the estimated impedivities and (b) imaginary part of the estimated impedivities.

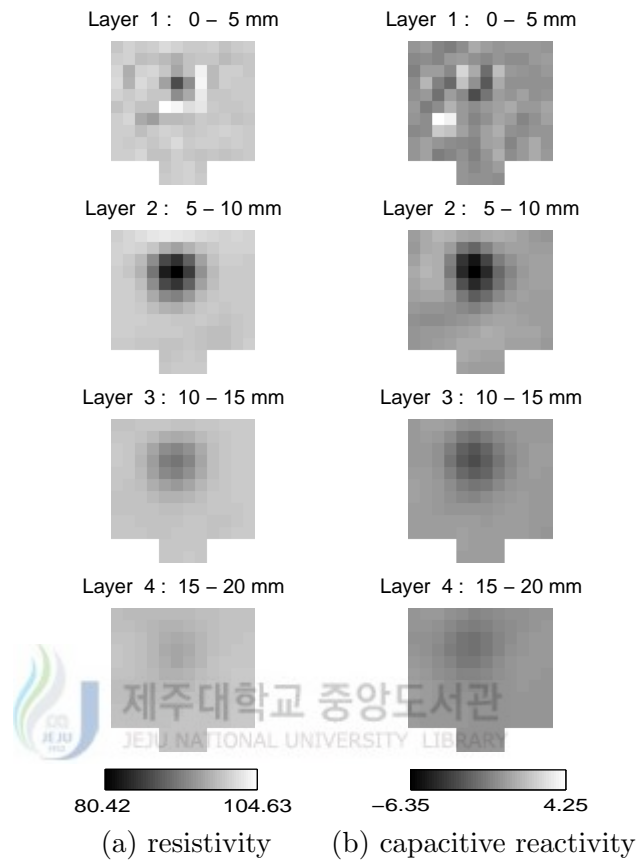


Figure 4.24: Reconstructed difference images of the 5 mm solder target. The solder target was placed 5 mm distant from the electrode in position B. The range of resistivity and capacitive reactivity values is given in  $\Omega\text{-cm}$ . (a) real part of the estimated impedivities and (b) imaginary part of the estimated impedivities.

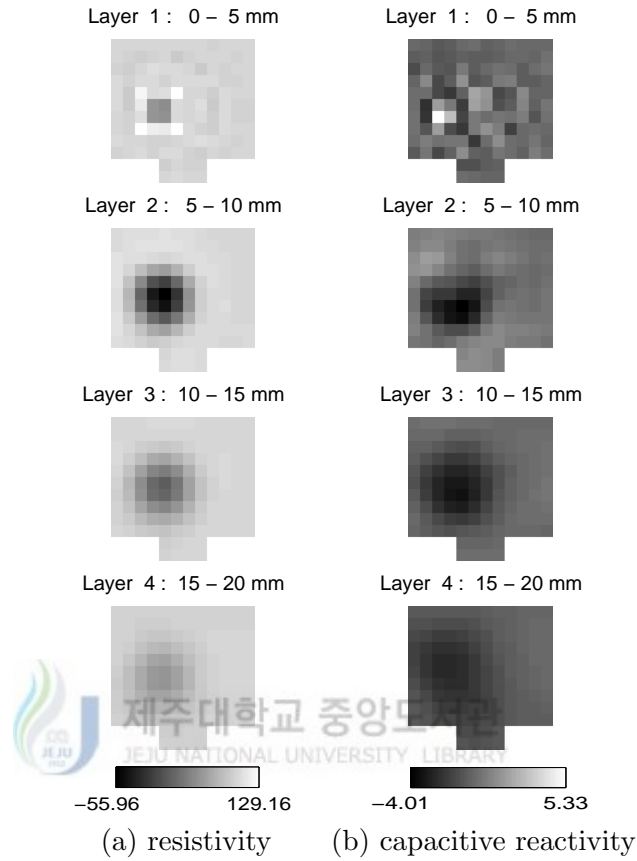
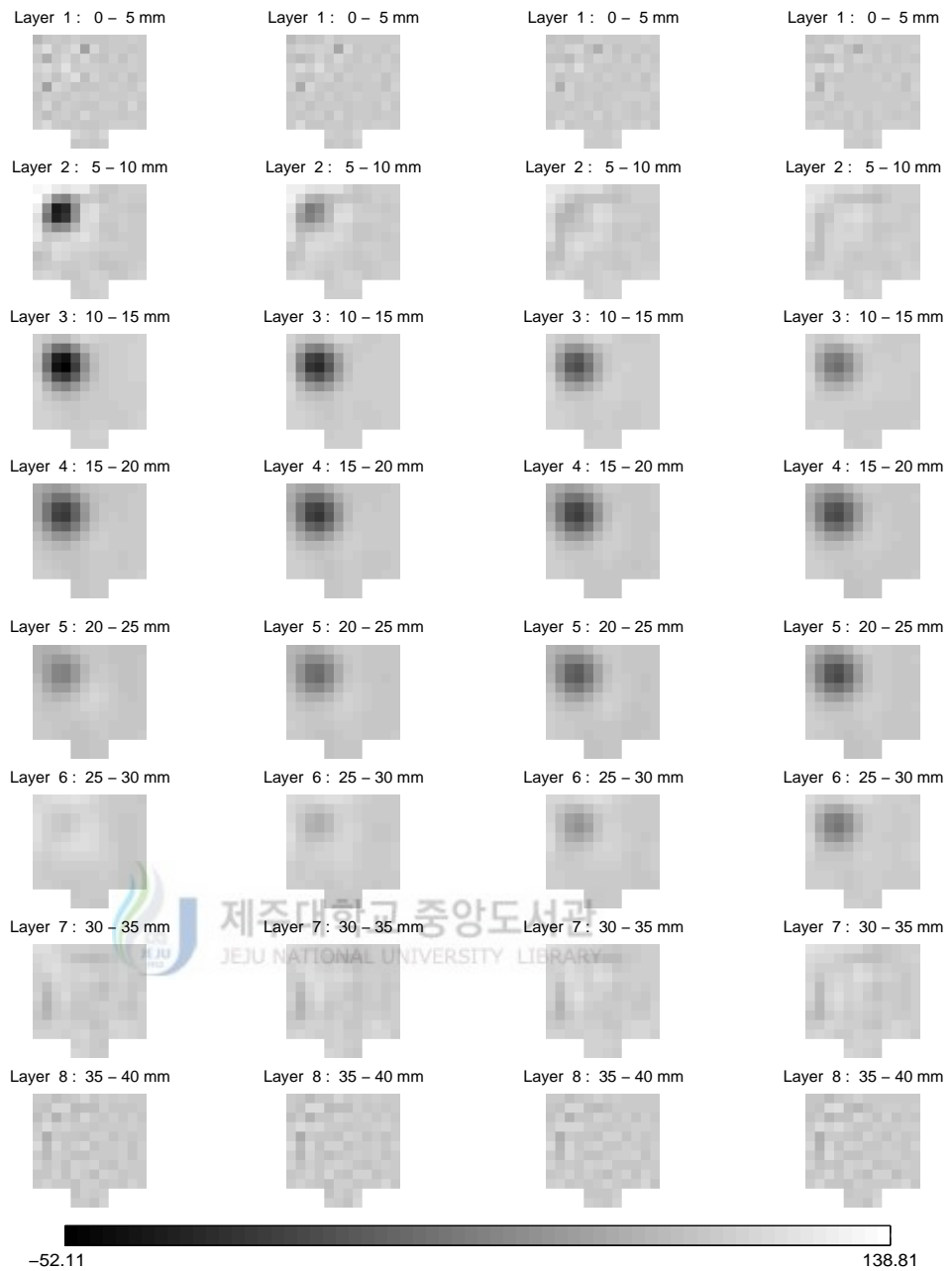


Figure 4.25: Reconstructed difference images of the 10 mm copper target. The copper target was placed 5 mm distant from the gap between the four adjacent electrodes in position C. The range of resistivity and capacitive reactivity values is given in  $\Omega\text{-cm}$ . (a) real part of the estimated impedivities and (b) imaginary part of the estimated impedivities.



(a) depth 7.5 mm (b) depth 10 mm (c) depth 12.5 mm (d) depth 15 mm

Figure 4.26: Reconstructed difference images of the 10 mm copper target according to the different depths in the  $z$ -axis. The copper target was positioned 7.5 mm, 10 mm, 12.5 mm and 15 mm distant from the face of the electrode in position A. The range of resistivity values is given in  $\Omega\text{-cm}$ .

### 4.3.3 Discussion

Breast phantom studies were conducted to illustrate the 3-D reconstruction performances using experimental data collected from a saline-filled phantom using the 64-electrode ACT4 instrument. The conductivity of the saline solution was chosen to approximate that of healthy breast tissue. Three targets as tumors were suspended in the phantom at several spatial position using a thin insulated rod in order to study the spatial resolution in the  $x$ - $y$  plane of the electrodes and  $z$ -axis.

In this study, the conductivity and permittivity or resistivity and capacitive reactivity distributions were simultaneously estimated and reconstructed using the 3-D reconstruction algorithms. In the reconstructed static images, the inhomogeneities were estimated, but the static images were sharper than the difference images. This is due to the discrepancy between the simplified forward model and the test phantom, and not considering the shunting effect and surface impedance of the electrodes in the forward modeling. And the data may contain some level of error due to the imprecise calibration of the ACT4 instrument. The data presented were obtained during the last phase of the instrument development, and the final calibration had not been performed when it was necessary to present these results. This causes the faint or blurred images in imaginary part of the admittivities or impedivities. As a result, the static images corresponding to experimental data resulted in poor target distinguishability. The difference images showed much better resolution since most of the electrode effects are subtracted away. In this study, the reconstructed results demonstrated that in the  $x$ - $y$  plane of the electrodes and at the different depths in the  $z$ -axis, the inhomogeneity's positions are well characterized in the reconstruction.

## V. Conclusions

In this work, the 2-D circular and 3-D mammography geometries are considered. The forward problem in both geometries was solved by the analytical method based on the separation of variables and Fourier series, and the analytical solutions of the different mathematical models were formulated. The result of the characteristic resistance study showed that the forward solution of the CE model was very close to the experimental data.

The ACT4 system was operated as a voltage source for this work, that is, the voltage patterns are applied to the body and the corresponding current patterns are measured. To apply the experimental data from the ACT4 system to the reconstruction, we need to modify the reconstruction algorithm. Therefore, for simplicity and effective computation, and to use the ACT4 experimental data, we found synthesized complex voltage patterns based on the normalized canonical currents from the applied complex voltages and measured complex currents. These synthesized complex voltages were applied to reconstruction algorithms for estimating the admittivity distribution from the experimental data of both geometries.

For the dynamic applications, the inverse problem was treated as a state estimation problem. The nonlinear measurement equation was linearized about the best homogeneous impedivity value as an initial guess, and the state (impedivity distribution) was estimated with the aid of the Kalman estimator. In particular, the Kalman gain matrix was pre-computed off-line and stored to minimize the on-line computational time. In this way, a dynamic complex impedance imaging technique was developed with the aid of the linearized Kalman filter (LKF) for real-time reconstruction of the human chest.

In the phantom study of the 2-D circular geometry, to illustrate the reconstruction performances in the sense of spatio-temporal resolution, we



considered dynamically changing scenarios, that is, it was assumed that the size of the heart was changing within the data acquisition time (one classical frame), but the admittivities of the different sizes (big and small) of the heart were kept the same, and the volume and the admittivity of the lungs were fixed. It represents the scenario when the person holds his/her breath during the acquisition of measurement data. For the simulation data we computed voltages with the FEM and for the experimental data we obtained voltages with a chest phantom in a simplified geometry of the human chest. The static imaging technique failed to obtain satisfactory temporal resolution for the reconstructed images when rapid changes in the impedivity distribution happen within the data acquisition time. But the dynamic imaging technique can provide an estimate of the impedivity distribution after each current pattern was applied to the body. Hence, the temporal resolution can be enhanced with the aid of the linearized Kalman filter.

In the phantom study of the 3-D mammography geometry, we evaluated the 3-D reconstruction performances of the proposed algorithms using experimental data collected from a saline-filled phantom using the 64-electrode ACT4 instrument. The conductivity of the saline solution was chosen to approximate that of healthy breast tissue. Three targets as tumors were suspended in the phantom at several spatial positions using a thin insulated rod in order to study the spatial resolution in the  $x$ - $y$  plane of the electrodes and  $z$ -axis.

In this study, the conductivity and permittivity or resistivity and capacitive reactivity distributions were simultaneously estimated and reconstructed using the reconstruction algorithms. In the reconstructed static images, the inhomogeneities were estimated, but the static images were sharper than the difference images. This is due to the discrepancy between the simplified forward model and the test phantom, and not considering the shunting effect and surface impedance of the electrodes in the forward modeling. And the data may contain some level of error due to the imprecise calibration of the

ACT4 instrument. The data presented were obtained during the last phase of the instrument development, and the final calibration had not been performed when it was necessary to present these results. This causes the faint or blurred images in imaginary part of the admittivities or impedivities. As a result, the static images corresponding to experimental data resulted in poor target distinguishability. The difference images showed better resolution since most of the electrode effects are subtracted away. The reconstructed results demonstrate that in the  $x$ - $y$  plane of the electrodes and according the different depths in the  $z$ -axis, the inhomogeneity's positions are well characterized in the reconstruction.

In the 3-D mammography geometry, in order to improve the static images in the reconstruction we try to find the forward solution of the CE model which takes into account the shunting effect and surface impedance. Since the 2-D forward solution of the CE model was already done, the 3-D forward solution will be solved soon. We are also considering modifying the boundary conditions of the mammography geometry.

This work is a fundamental study for breast cancer detection as the application of EIT. The main goal of the present work is to apply a 3-D reconstruction algorithm with the planar electrode geometry to the early detection of breast cancer.

## Summary

Breast cancer is the most commonly diagnosed malignant tumor among women in the western world. Early detection of breast cancer is the most effective method for reducing breast cancer mortality rate.

It has been reported that breast tumors have typically higher conductivity and permittivity, that is, there are significant differences in electric properties between normal breast tissues and breast tumors. Therefore, electrical impedance of tissue could be used as an indicator for breast cancer detection.

Electrical impedance tomography (EIT) is an imaging modality that estimates the electrical properties in a body. In EIT, small electrical currents are injected through electrodes placed on the surface of the body and the corresponding voltages are measured through these electrodes. These voltage and current data are used in reconstruction algorithms to reconstruct and display the internal electrical properties.

In this thesis, the 2-D circular and 3-D mammography geometries are considered, and reconstruction algorithms are applied to both geometries. The forward problem in both geometries was solved by the analytical method based on the separation of variables and Fourier series, and the analytical solutions of the different mathematical models were formulated.

To apply the experimental data from the ACT4 system to the reconstruction, we found synthesized complex voltage patterns based on the normalized canonical currents, which are combined with the applied complex voltages and measured complex currents.

In the phantom study of the 2-D circular geometry, to illustrate the reconstruction performance in the sense of spatio-temporal resolution, we considered dynamically changing scenarios, that is, it was assumed that the size of the heart was changing within the data acquisition time (one classical frame),

but the admittivities of the different sizes (big and small) of the heart were kept the same, and the volume and the admittivity of the lungs were fixed. It represents the scenario when the person holds his/her breath during the acquisition of measurement data. For the simulation data we computed voltages with the FEM and for the experimental data we obtained voltages with a chest phantom in a simplified geometry of the human chest.

In the phantom study of the 3-D mammography geometry, the 3-D reconstruction performance is illustrated using experimental data collected from a saline-filled phantom using the 64-electrode ACT4 instrument. The conductivity of the saline solution was chosen to approximate that of healthy breast tissue. Three targets as tumors were suspended in the phantom at several spatial positions using a thin insulated rod in order to study the spatial resolution in the  $x$ - $y$  plane of the electrodes and  $z$ -axis.

In this study, the admittivity or impedivity distributions were simultaneously estimated and reconstructed using the reconstruction algorithms. In the reconstructed static images, the inhomogeneities were estimated. The static images corresponding to experimental data resulted in poor target distinguishability. The difference images showed better resolution since most of the electrode effects are subtracted away. The reconstructed results demonstrate that in the  $x$ - $y$  plane of the electrodes and according the different depths in the  $z$ -axis, the inhomogeneity's positions are well characterized in the reconstruction.

## References

- American Cancer Society 2005a *Breast cancer facts and figures 2005-2006*, (Atlanta: American Cancer Society)  
(<http://www.cancer.org/docroot/home/>)
- American Cancer Society 2005b Mammograms and Other Breast Imaging Procedures *Cancer Reference Information*, American Cancer Society homepage (<http://www.cancer.org/docroot/home/>)
- Boone K, Barber D and Brown B 1997 Imaging with electricity: report of the European concerted action on impedance tomography *J. Med. Eng. Technol.* **21** 201–232
- Boring C C, Squires T S and Tong T 1994 Cancer statistic, *CA Cancer J. Clin.* **44** 7–26
- Cheney M and Isaacson D 1992 Distinguishability in impedance imaging *IEEE Trans. Biomed. Eng.* **39** 852–860
- Cheney M, Isaacson D, Newell J C, Simske S and Goble J 1990 NOSER: An algorithm for solving the inverse conductivity problem *Int. J. Imaging Syst. Technol.* **2** 65–75
- Cheng K S, Isaacson D, Newell J C and Gisser D G 1989 Electrode models for electric current computed tomography *IEEE Trans. Biomed. Eng.* **36** 918–924
- Cherepenin V, Karpov A, Korjenevsky A, Kornienko V, Mazaletskaya A, Mazourov D and Meister D 2001 A 3D electrical impedance tomography (EIT) system for breast cancer detection *Physiol. Meas.* **22** 9–18
- Choi M H, Kao T J, Isaacson D, Saulnier G J and Newell J C 2004 A simplified model of mammography geometry for breast cancer imaging with electrical impedance tomography *Proc. 26th Conf. of the IEEE-EMBS San Francisco* 1310–1313
- Cook R D, Saulnier G J, Gisser D G, Goble J C, Newell J C and Isaacson D 1994 ACT3: A high speed high precision electrical impedance tomography *IEEE Trans. Biomed. Eng.* **41** 713–722

- Dartmouth College 2001 EIS Breast Imaging Research at Dartmouth College (<http://www-nml.dartmouth.edu/biomedprg/EIS/index.html>)
- Edell S L and Eisen M D 1999 Current imaging modalities for the diagnosis of breast cancer *Del. Med. J.* **71** 377-382
- Edic P M 1994 The Implementation of a Real-Time Electrical Impedance Tomograph *PhD Thesis* Rensselaer Polytechnic Institute, USA
- Edic P M, Saulnier G J, Newell J C and Isaacson D 1995 A real-time electrical impedance tomography *IEEE Trans. Biomed. Eng.* **42** 849-859
- FDA 1999 TransScan T-Scan 2000 (<http://www.fda.gov/cdrh/pdf/p970033.html>)
- Fricke H and Morse S 1926 The electrical capacity of tumors of the breast *J. Cancer Res.* **10** 340-376
- Gelb A 1974 *Applied Optimal Estimation* (Massachusetts: The M.I.T. Press)
- Gisser D G, Isaacson D and Newell J C 1990 Electric current computed tomography and eigenvalues *SIAM J. Appl. Math.* **50** 1623-1634
- Grewal M S and Andrews A P 2001 *Kalman Filtering: Theory and Practice, Using MATLAB* (New York: John Wiley & Sons. Inc.)
- Imaginis 2000 T-scan breast imaging (<http://imaginis.com/t-scan/>)
- Isaacson D 1986 Distinguishability of conductivities by electric current computed tomography *IEEE Trans. Med. Imag.* **MI-5** 92-95
- Jossinet J 1998 The impedivity of freshly excised human breast tissue *Physiol. Meas.* **19** 61-75
- Kao T J, Newell J C, Isaacson D and Saulnier G J 2005 A 3-D reconstruction algorithm for electrical impedance tomography using a handheld probe for breast cancer detection *Proc. 6th Conf. on Biomed. Appl. of EIT* London
- Kao T J, Newell J C, Saulnier G J and Isaacson D 2003 Distinguishability of inhomogeneities using planar electrode arrays and different patterns of applied excitation *Physiol. Meas.* **24** 403-411
- Kim K Y, Kang S I, Kim M C, Kim S, Lee Y J and Vauhkonen M 2002 Dynamic image reconstruction in electrical impedance tomography with known internal structures *IEEE Trans. Magn.* **38** 1301-1304

- Kim K Y, Kim B S, Kim M C, Lee Y J and Vauhkonen M 2001 Image reconstruction in time-varying electrical impedance tomography based on the extended Kalman filter *Meas. Sci. Technol.* **12** 1032–1039
- Liu N, Saulnier G J, Newell J C and Kao T J 2005 ACT4: A high-precision, multi-frequency electrical impedance tomograph *Proc. 6th Conf. on Biomed. Appl. of EIT* London
- Mirabel Medical 2002 T-Scan™ 2000ED (<http://www.transscan.co.il/>)
- Mueller J L, Isaacson D and Newell J C 1999 A reconstruction algorithm for electrical impedance tomography data collected on rectangular electrode arrays *IEEE Trans. Biomed. Eng.* **46** 1379–1386
- Osterman K S, Kerner T E, Williams D B, Hartov A, Poplack S P and Paulsen K D 2000 Multifrequency electrical impedance imaging: preliminary in vivo experience in breast *Physiol. Meas.* **21** 99–109
- Ross A S 2003 An adaptive current tomograph for breast cancer detection *PhD Thesis* Rensselaer Polytechnic Institute, USA
- Singhal H and Thomson S 2004 Breast Cancer Evaluation, eMedicine homepage (<http://www.emedicine.com/med/topic3287.htm>)
- Somersalo E, Cheney M and Isaacson D 1992 Existence and uniqueness for electrode models for electric current computed tomography *SIAM J. Appl. Math.* **52** 1023–1040
- Surowiec A J, Stuchly S S, Barr J B and Swarup A 1988 Dielectric properties of breast carcinoma and the surrounding tissues *IEEE Trans. Biomed. Eng.* **35** 257–263
- TCI (Technology Commercialization International Inc.) 2003 CENTILLION® Advanced digital imaging system for breast cancer detection (<http://www.tcimed.com/bcddintro.html>)
- Trigo F C, Gonzalez-Lima R, and Amato M B P 2004 Electrical impedance tomography using the extended Kalman filter *IEEE Trans. Biomed. Eng.* **51** 72–81
- Vauhkonen M 1997 Electrical impedance tomography and prior information *PhD Thesis* University of Kuopio, Finland
- Vauhkonen M, Karjalainen P A and Kaipio J P 1998 A Kalman filter approach to track fast impedance changes in electrical impedance tomography

*IEEE Trans. Biomed. Eng.* **45** 486–493

Vauhkonen M, Lionheart W R B, Heikkinen L M, Vauhkonen P J and Kaipio J P 2001 A MATLAB package for the EIDORS project to reconstruct two-dimensional EIT images *Physiol. Meas.* **22** 107–111

Vauhkonen P J, Vauhkonen M, Mäkinen T, Karjalainen P A and Kaipio J P 2000 Dynamic electrical impedance tomography - phantom studies *Inverse Problems Eng.* **8** 495–510

Vauhkonen P J 2004 Image Reconstruction in Three-Dimensional Electrical Impedance Tomography *PhD Thesis* University of Kuopio, Finland

Yorkey T J, Webster J G and Tompkins W J 1987 Comparing reconstruction algorithms for electrical impedance tomography *IEEE Trans. Biomed. Eng.* **34** 843–852

Webster J G 1990 *Electrical Impedance Tomography* (Bristol: IOP Publishing Ltd)

Zou Y and Guo Z 2003 A review of electrical impedance techniques for breast cancer detection *Med. Eng. Phys.* **25** 79–90

Z-Tech 2004 Z-Tech Breast Cancer Detection System, Z-Tech Inc. (<http://www.z-techinc.com/>)





## Acknowledgment

I would like to extend many thanks and my deepest appreciation to my advisor, Professor Kyung Youn Kim for his continuous support and guidance through my academic career. Professor Kim always expressed enthusiasm for my work and freely shared his wonderful ideas. I would like to thank professors of Department of Electronic Engineering, Professors Yang-Hoi Doh, Min-Je Kang, Kyung-Sik Kim, Kwang-Man Lee, Sung-Taek Ko, and Suk-Joon Ko for their encouragement during the course of this work. I offer special thanks to Professors Min Chan Kim and Sin Kim who have encouraged me to strive for a higher level of achievement in my graduate career. I would also like to thank Umer Zeeshan Ijaz and Jeong-Hoon Kim for their help. It has been a pleasure working with them.

I would like to express my sincere gratitude to Professors Jonathan Newell, David Isaacson, and Gary Saulnier at Rensselaer Polytechnic Institute. It has been a privilege to work with intelligent and prominent professors in the field of electrical impedance tomography. Special thanks to Professor Isaacson for teaching me a lot of mathematical principles and for freely sharing his great ideas. I would also like to thank Dr. Felix Kao, Roger Xia, and Ning Liu for their assistance. I have enjoyed doing my research with them and their friendship has enriched my time at Rensselaer Polytechnic Institute.

Finally I would like to acknowledge my family, especially my parents and my parents-in-law for their endless concern, support, and willingness which played a significant role in the successful completion of this thesis. I would like to dedicate this thesis to my wife, Hyo Jeong Yang who has always encouraged me in my academic career.